RAS Techniques and Instruments

RASTAI **2,** 148–206 (2023) https://doi.org/10.1093/rasti/rzad009
Advance Access publication 2023 March 22

The effect of stellar contamination on low-resolution transmission spectroscopy: needs identified by NASA's Exoplanet Exploration Program Study Analysis Group 21

Benjamin V. Rackham [1,2★†] Néstor Espinoza [3] Svetlana V. Berdyugina,[4,5] Heidi Korhonen [6] Ryan J. MacDonald [7] Benjamin T. Montet,[8] Brett M. Morris,[9] Mahmoudreza Oshagh,[10] Alexander I. Shapiro,[11] Yvonne C. Unruh [12] Elisa V. Quintana,[13] Robert T. Zellem,[14] Dániel Apai,[15,16] Thomas Barclay,[13,17] Joanna K. Barstow [18] Giovanni Bruno [19] Ludmila Carone,[20] Sarah L. Casewell,[21] Heather M. Cegla,[22] Serena Criscuoli,[23] Catherine Fischer,[4] Damien Fournier,[11] Mark S. Giampapa,[15] Helen Giles,[24] Aishwarya Iyer,[25] Greg Kopp,[26] Nadiia M. Kostogryz,[11] Natalie Krivova,[11] Matthias Mallonn,[27] Chima McGruder,[28] Karan Molaverdikhani [29,30,31] Elisabeth R. Newton,[32] Mayukh Panja,[11] Sarah Peacock,[13] Kevin Reardon,[33,34] Rachael M. Roettenbacher,[35,36] Gaetano Scandariato,[19] Sami Solanki,[11] Keivan G. Stassun [37] Oskar Steiner,[4] Kevin B. Stevenson,[38] Jeremy Tregloan-Reed [39] Adriana Valio,[40] Sven Wedemeyer,[41,42] Luis Welbanks,[25] Jie Yu,[11] Munazza K. Alam,[43] James R. A. Davenport,[44] Drake Deming,[45] Chuanfei Dong,[46,47] Elsa Ducrot,[48] Chloe Fisher,[9] Emily Gilbert,[49] Veselin Kostov,[13,50] Mercedes López-Morales,[28] Mike Line,[25] Teo Močnik,[51] Susan Mullally,[3] Rishi R. Paudel,[13,17] Ignasi Ribas[52,53] and Jeff A. Valenti[3]

Affiliations are listed at the end of the paper

Accepted 2023 March 13. Received 2023 March 3; in original form 2022 September 20

ABSTRACT

Study Analysis Group 21 (SAG21) of NASA's Exoplanet Exploration Program Analysis Group was organized to study the effect of stellar contamination on space-based transmission spectroscopy, a method for studying exoplanetary atmospheres by measuring the wavelength-dependent radius of a planet as it transits its star. Transmission spectroscopy relies on a precise understanding of the spectrum of the star being occulted. However, stars are not homogeneous, constant light sources but have temporally evolving photospheres and chromospheres with inhomogeneities like spots, faculae, plages, granules, and flares. This SAG brought together an interdisciplinary team of more than 100 scientists, with observers and theorists from the heliophysics, stellar astrophysics, planetary science, and exoplanetary atmosphere research communities, to study the current research needs that can be addressed in this context to make the most of transit studies from current NASA facilities like *Hubble Space Telescope* and *JWST*. The analysis produced 14 findings, which fall into three science themes encompassing (i) how the Sun is used as our best laboratory to calibrate our understanding of stellar heterogeneities ('The Sun as the Stellar Benchmark'), (ii) how stars other than the Sun extend our knowledge of heterogeneities ('Surface Heterogeneities of Other Stars'), and (iii) how to incorporate information gathered for the Sun and other stars into transit studies ('Mapping Stellar Knowledge to Transit Studies'). In this invited review, we largely reproduce the final report of SAG21 as a contribution to the peer-reviewed literature.

Key words: exoplanets – methods: observational – techniques: photometric – techniques: spectroscopic – stars: activity – Sun: activity.

1 INTRODUCTION

Study Analysis Group 21 (SAG21) of NASA's Exoplanet Exploration Program Analysis Group (ExoPAG) was organized to study the effect of stellar contamination on space-based transmission spectroscopy. This invited review summarizes the work of SAG21

* E-mail: brackham@mit.edu
† 51 Pegasi b Fellow

and largely reproduces the final report submitted to NASA (Rackham et al. 2022) as a contribution to the peer-reviewed literature. We begin with a brief description of the motivation for SAG21, the goals of the group, the methods by which we conducted our analysis, and the structure of this review.

1.1 Motivation

Transmission spectroscopy is a method for identifying the atmospheric composition of an exoplanet by measuring a wavelength-dependent radius of a planet as it transits its star (Seager & Sasselov 2000; Brown et al. 2001). This technique has been successfully applied to many exoplanets, primarily using the *Hubble Space Telescope* (*HST*) and *Spitzer Space Telescope* (*Spitzer*; e.g. Charbonneau et al. 2002; Tinetti et al. 2007; Agol et al. 2010; Désert et al. 2011b; Knutson et al. 2011; Deming et al. 2013; Fraine et al. 2014; Kreidberg et al. 2014; Sing et al. 2016), but also using ground-based telescopes (e.g. Redfield et al. 2008; Snellen et al. 2008, 2010; Bean, Miller-Ricci Kempton & Homeier 2010; Jordán et al. 2013; Danielski et al. 2014; Nikolov et al. 2016). Most transmission spectroscopy studies to date have targeted gas giant worlds due to their larger expected signatures, which scale with the planet's atmospheric scale height. During the next two decades, and thanks to the next generation of ground- and space-based observatories, the technique is expected to also be a major source of information on the atmospheres of rocky exoplanets.

Transmission spectroscopy relies on a precise understanding of the wavelength-dependent brightness of the star being occulted. However, stars are not homogeneous, constant light sources but have temporally evolving photospheres and chromospheres with inhomogeneities like spots, faculae, and plages (e.g. Berdyugina 2005). The surface features of the star change both intrinsically as active regions evolve and from the perspective of an observer as the star rotates. Spots and faculae have different temperatures from the disc-averaged photosphere, and for cooler stars, can have molecular features distinct from the star itself but similar to those in a planet's atmosphere, including H_2O (Wöhl 1971), TiO (Neff, O'Neal & Saar 1995), and other molecules (Berdyugina, Solanki & Frutiger 2003). Some studies have found that the signal from stellar inhomogeneities can exceed the signal from the planetary spectral features (e.g. Rackham, Apai & Giampapa 2018, 2019). In particular, small exoplanets – mini-Neptunes and rocky planets – around M-dwarf host stars are susceptible to this 'transit light source effect (TLSE)'. To make the most of transit studies from current NASA facilities like *HST* and *JWST*, it is essential we quantify the impact of stellar contamination on transmission spectroscopy and develop methods to mitigate for it.

1.1.1 Relevance to Astro2020

This topic is directly relevant to the first science theme identified in the Astro2020 Decadal Survey, *Worlds and Suns in Context*, and its priority area, *Pathways to Habitable Worlds*. Before the launch in the 2040s of the Habitable Worlds Observatory, a large space telescope capable of directly imaging Earth-like worlds, transit observations will provide our best pathway to identifying and studying rocky exoplanets, including potentially habitable ones. These will necessarily transit cool dwarfs, which tend to remain active long after their formation and possess heterogeneous photospheres. Even with the advanced direct-imaging capabilities enabled by the Habitable Worlds Observatory, transit observations will remain a critical tool in the study of exoplanetary atmospheres, as emphasized by the LUVOIR and HabEx Mission Concept Study Final Reports (The LUVOIR Team 2019; Gaudi et al. 2020). Thus, the topic of SAG21 is especially relevant to NASA's science priorities in the next two decades and beyond.

1.2 Goals of SAG21

This SAG brought together an interdisciplinary team of more than 100 scientists, with observers and theorists from the heliophysics, stellar astrophysics, planetary science, and exoplanetary atmosphere research communities to address both the impact of stellar contamination on transmission spectra and constraints on stellar photospheric heterogeneity enabled by transiting exoplanets.

SAG21 has six goals:

(i) Report on what effect stellar contamination could have on future space-based transmission spectroscopy measurements;
(ii) Identify regions of the parameter space in which care should be exercised with respect to stellar contamination in the context of transmission spectroscopy studies;
(iii) Identify measures that can be taken to understand the magnitude of stellar contamination;
(iv) Identify what modelling efforts can further our understanding of stellar contamination;
(v) Develop methods to identify measurements that might be contaminated; and
(vi) Pinpoint complementary observations that can be combined with transmission spectroscopy to mitigate or correct for stellar contamination.

1.3 Methods

1.3.1 Soliciting contributions

The SAG21 co-chairs solicited members for the group via open calls for members to the ExoPAG newsletter and other email listserves, social media sites, presentations at ExoPAG meetings, and direct communications to researchers with relevant expertise. In total, 122 people joined the dedicated email list for SAG21, and the group ultimately included more than 60 active participants that contributed to the discussion in some form.

1.3.2 Subgroups

Given the large interest from the community, we divided the analysis of SAG21 into five thematic areas and formed subgroups with relevant expertise to study each area. The subgroups studied the topics of:

(i) Stellar photospheric and chromospheric heterogeneity,
(ii) Unocculted active regions,
(iii) Occulted active regions,
(iv) Stellar and planetary retrievals, and
(v) Future complementary observations.

Each subgroup held roughly a dozen virtual meetings over the timespan of the SAG to refine the questions to be considered, assign member duties, discuss updates on the analysis, and decide on its final findings. Subgroup leads met with the SAG21 co-chairs monthly to share and discuss progress. Significant conversations also took place on public channels of SAG21's dedicated Slack Workspace.[1] The detailed scopes of these groups are defined in their corresponding sections of this review.

[1] https://slack.com/

1.3.3 SAG21 community symposium

SAG21 also hosted a 2-d virtual community symposium over Zoom on 2021 March 8–9 to share preliminary results from the analysis and solicit feedback from the wider community. The meeting included five overview presentations on the analysis from subgroup leads as well as 21 contributed community talks on subjects relevant to the SAG. In total, the symposium brought together roughly 110 attendees, including 46 active participants in question-and-answer sessions. The recordings of all talks are available on the SAG21 Community Symposium Website.[2]

1.3.4 Final report

Considering the analysis of the subgroups and inputs from the community symposium, each subgroup prepared a draft chapter of the report in mid-2021 outlining their top-level findings and the analysis that lead to them. Each chapter was then reviewed by at least three members from other subgroups, who provided detailed feedback that the original subgroup leads later addressed. The entire report was then thoroughly edited by the SAG21 co-chairs with an eye towards consistency, logical ordering of ideas between subgroups, and relevance to the scope of SAG21. The report was then shared again among all members for a final round of feedback and, after minor revisions, submitted to NASA and posted on the arXiv (Rackham et al. 2022).

The combined analysis produced 14 findings, which are contextualized statements of what we understand to be the current needs that can be addressed to further our understanding of the photospheres of exoplanetary host stars and make the best use of precise space-based transmission spectra of exoplanets. While SAG21 was focused on space-based observations specifically, the findings are generally applicable to low-to-medium-resolution transmission spectroscopy, both ground- and space-based. Following the format of the Exoplanet Exploration Program Science Gap List, each finding includes a summary statement along with a statement of the capability needed, capability today, and mitigation in progress to address each need.

1.4 The structure of this review

Like the SAG21 report submitted to NASA, the structure of this invited review follows that of SAG21 itself, with sections dedicated to the work of each subgroup. In each section, we introduce the scope of the analysis and the individual topics we studied. We then present the information on each topic we considered in reaching a finding. We summarize the 14 findings and conclude in Section 7. Table A1 lists the abbreviations and acronyms used throughout this review.

2 STELLAR PHOTOSPHERIC AND CHROMOSPHERIC HETEROGENEITY

Essential questions include the following:

(i) What do we know about solar and stellar photospheric and chromospheric heterogeneity (PCH)?

(ii) Which properties of PCHs are of relevance to exoplanet transit spectroscopy?

(iii) How can the knowledge of the Sun help to constrain such PCH properties?

(iv) Which of these PCH properties can be constrained by stellar observations? Which observations are the most useful (photometry, spectroscopy, X-ray, etc.)?

(v) Which of these PCH properties can be constrained using advanced magnetohydrodynamic (MHD) and hydrodynamic (HD) simulations?

(vi) How do stellar fundamental parameters influence PCH?

(vii) What is known about PCH of high-priority exoplanet host stars?

(viii) Which PCH properties of the known host stars are critical for the characterization of exoplanetary atmospheres?

2.1 Introduction

From high-spatial-resolution observations of the Sun we know that the solar atmosphere is anything but homogeneous. The main sources of the heterogeneities in the solar photosphere and chromosphere are due to the plasma flows and magnetic fields as well as the interplay between them (see e.g. the review by Solanki, Inhester & Schüssler 2006). Observations suggest that such heterogeneities are also present in the atmospheres of other stars (Berdyugina 2005; Reiners 2012). They manifest themselves via, e.g. photometric and spectral variability (see e.g. recent books by Engvold, Vial & Skumanich 2019; Basri 2021).

When a planet transits a star, such heterogeneities lead to a background spectral signal and temporal modulation on the transit light curve, contaminating the transmission spectrum (e.g. Pont et al. 2008). The magnitude of the contamination is defined by the brightness contrasts and the fractional areas of various magnetic features and their fine structure (e.g. Sing et al. 2011). From solar observations, we know that the contrast between different solar structures is strongly wavelength-dependent (e.g. Wöhl, Wittmann & Schröter 1970). Consequently, the underlying stellar transmission spectrum depends on the wavelength and can, thus, hide or mimic a genuine planetary atmospheric signal (e.g. Ballerini et al. 2012; Rackham et al. 2018, 2019).

To distinguish between planetary and stellar signals we must observe and model the contribution of stellar heterogeneities to transmission spectra. In particular, we need to understand the dependence of the stellar signal as a function of wavelength and time. Modelling requires accurate knowledge of properties of various stellar features on stars with different fundamental parameters and magnetic activity levels.

The main goal of this section is to summarize current knowledge, ongoing work, and limits in our understanding of stellar heterogeneities that is of relevance for transmission spectroscopy. In particular, the focus here is given to the optical and near-infrared (NIR), given the relevance of these wavelengths to the topic of this review: the 'stellar contamination' of transmission spectra (Rackham et al. 2018, 2019). We begin in Section 2.2 by introducing observations and modelling efforts to understand the star for which we can obtain arguably the most detailed information about these heterogeneities: the Sun, together with examples of Solar system planetary transits of the Sun-as-a-star. We then introduce simulations of surface structures on other stars in Section 2.3. We conclude this section by discussing observations of stars other than our Sun in Section 2.4.

2.2 The Sun: a prime window to understand stellar heterogeneities

Stellar heterogeneities in our Sun have been observed by the unaided eye at least since 800 BC, when dark spots – today known as

[2] https://sites.google.com/view/sag21symposium

'sunspots' – were seen to sporadically appear on the solar disc as reported by East Asian sunspot sightings (Stephenson 1990). The advent of telescopes in the 1600s allowed for a much more detailed and systematic analysis of these features, which Galileo Galilei interpreted as surface features *on the (spherical) Sun* (see e.g. Casanovas 1997). Later observations confirmed these early explanations and, in fact, extended the diversity of solar surface heterogeneities beyond these first noticed dark spots.

Solar (and, by extension, stellar) atmospheric heterogeneities are now understood, in general, to arise from both plasma-motion-driven processes and magnetic-field processes. The former features are generated by a constantly evolving cellular granulation pattern on the visible solar surface, accompanied by oscillations dominating within a rather narrow frequency interval. Surface magnetic structures, on the other hand, are driven by evolution of small-scale magnetic (also known as 'bright') features and spot-like magnetic (also known as 'dark') features. Both plasma-motion and magnetic-driven processes have distinct properties, e.g. the time-scales on which they are observed to act. While plasma-motion-driven features seem to impact various solar observables (e.g. the total solar irradiance; TSI) on time-scales of minutes to hours (Solanki & Unruh 2013), solar magnetic features give rise to longer time-scale variations, ranging from hours to years (Shapiro et al. 2017, see Fig. 1). Even though some properties of these two main processes, such as time-scales and flux variations at certain wavelengths, might not seem to depend on each other (see e.g. Bastien et al. 2013), they are physically related to one another as plasma-driven motions are inherently impacted by magnetic processes and vice versa (e.g. Stein 2012). Distinct spatial and wavelength-dependent signatures of these processes and their modelling are reviewed in this section.

In the following sections, we summarize observed and modelled properties of solar surface plasma-motion and magnetic field structures and processes relevant for transmission spectroscopy, together with examples of Mercury and Venus transits of the Sun-as-a-star.

2.2.1 *Solar granulation and oscillations*

Brightness variations due to granulation and oscillations in the Sun are important for understanding their influence on transit spectroscopy studies, since the time-scales on which they occur are similar to those of transit events (minutes to hours). Also, to date, the Sun is the only star on which we can spatially resolve these features in detail, so our host star is key to understanding the properties and main mechanisms driving them. Solar granulation and oscillations are believed to be reasonably well understood for the Sun.

The granulation brightness fluctuations are driven by intensity variations of hot, bright (up-welling) granules and cool, dark (down-flowing) intergranular lanes (see e.g. Nordlund et al. 2009; Stein 2012). The contrast between these features is typically measured through the mean-normalized RMS of the intensity fluctuations within an area/image of the Sun taken at a given wavelength or a bandpass.

The true RMS contrast of granulation, as seen in broad-band or continuum images of very quiet regions of the Sun, has been the subject of debates for decades, mainly because of the great disparity of results from early three-dimensional (3D) HD simulations and observations. Observations with the space-borne Hinode *Solar Optical Telescope* (*SOT*, Tsuneta et al. 2008) show 7 per cent intensity contrasts at 630 nm (Danilovic et al. 2008). Employing the highest spatial-resolution simulations and convolving with *SOT*'s point spread function, which is believed to be well known, Danilovic et al. (2008) showed that the simulated 14.4 per cent at 630 nm

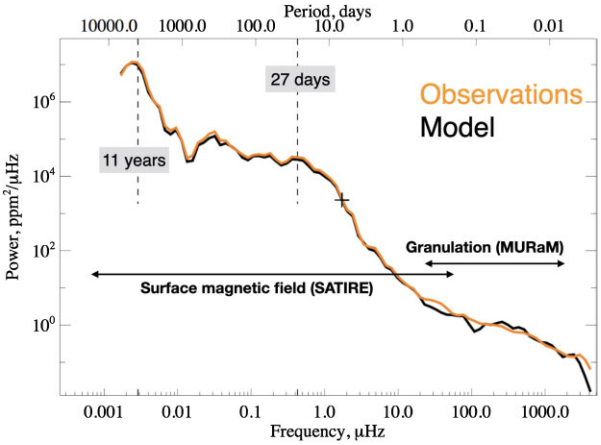

Figure 1 Global wavelet power spectrum of modelled (black) and measured (orange) TSI variations. Double arrows indicate frequency ranges where variability is dominated by surface magnetic field and granulation, modelled with the Spectral And Total Irradiance REconstruction (SATIRE; Yeo et al. 2014a) and Max-Planck-Institute for Astronomy/University of Chicago Radiation Magneto-hydrodynamics code (MURaM) (Vögler et al. 2005) codes, respectively. From Shapiro et al. (2017).

was degraded to close to the observed 7 per cent. Wedemeyer-Böhm & Rouppe van der Voort (2009) measured RMS contrast values of 12.8 ± 0.5 per cent, 8.3 ± 0.4 per cent, and 6.2 ± 0.2 per cent at disc centre for the blue, green, and red continuum, respectively using the Broad-band Filter Imager (BFI) of *SOT*. These values translate to 26.7 ± 1.3 per cent, 19.4 ± 1.4 per cent, and 16.6 ± 0.7 per cent for the blue, green, and red continuum, respectively, when deconvolving the images with the appropriate point spread function. The filters were centred at 450.45, 555.05, and 668.40 nm, respectively. Consequently, there is now good agreement between simulations and deconvolved resolved granulation observations, which both can be considered to yield the true intensity contrast of the granular structure on the surface of the Sun. Table 1 gives a summary of these values.

These measurements show a strong decrease of the granule contrast towards longer wavelengths, which translates into smaller amplitudes of the time-dependent RMS brightness variability at longer wavelengths. Such a contrast decrease was also observed to occur towards infrared (IR) wavelengths and was shown to strongly depend on the solar limb distance and location, with the smallest contrast near the limb (see e.g. Sánchez Cuberes et al. 2003, and references therein). This occurs because these intensity variations track temperature fluctuations: when assuming a blackbody spectrum for the granulation, its contrast and variation amplitudes are reduced at longer wavelengths. A similar argument can be made for oscillations, whose brightness fluctuation amplitudes are expected to strongly decrease with wavelength as well ($\sim 1/\lambda$; see e.g. Kjeldsen & Bedding 2011; Samadi et al. 2012).

In contrast to granulation, solar oscillations demonstrate much smaller brightness variability amplitudes on their time-scales (on the order of minutes). A full-disc RMS variability measurement over 8-h time-scales of about ∼15 parts-per-million (ppm) were measured by the Solar and Heliospheric Observatory (SOHO) using the Variability of solar IRradiance and Gravity Oscillations (Frohlich et al. 1997) instrument (Bastien et al. 2013). Also, the *Kepler Space Telescope* (*Kepler*; Borucki et al. 2010) was used to measure variability of the solar reflected light from Neptune of the order of several ppm (e.g. Gaulme et al. 2016, and references therein).

Table 1. Continuum contrasts of a solar-quiet region granulation at disc centre (c_{rms}) measured with two space-based telescopes of different aperture.

Satellite	Instrument	Aperture	Wavelength	c_{rms}	Deconvolved	Reference
SDO	HMI	14 cm	617.3 nm	4.0 per cent	12.2 per cent	Yeo et al. (2014a)
Hinode	SOT/SP	50 cm	630.0 nm	7.0 per cent	14.4 per cent	Danilovic et al. (2008)
Hinode	SOT/BFI	50 cm	450.5 nm	12.8 per cent	26.7 per cent	Wedemeyer-Böhm & Rouppe van der Voort (2009)
			555.0 nm	8.3 per cent	19.4 per cent	
			668.4 nm	6.2 per cent	16.6 per cent	

Given the level of brightness fluctuations and their dependence on the wavelength discussed above, it might follow that if other stars behaved like our Sun, granulation and oscillations may not be an important part of the budget for stellar contamination in the transmission spectrum of planets orbiting Sun-like stars in the IR. Rather, the impact of these processes could be a simple noise contribution (also known as 'jitter') to the transit light curves themselves. However, we still lack multiwavelength and precise centre-to-limb variation (CLV) measurements of this effect on the Sun in order to make a concrete assessment of how important this effect could be as a contamination source in transmission spectra from ultraviolet (UV; ∼0.3 μm) to NIR wavelengths (∼5 μm), which are relevant for transit studies with present and future space-based observatories. In particular, some studies (e.g. Chiavassa et al. 2017) do suggest that granulation could become an important effect for Earth–Sun transiting exoplanet analogues. We discuss this in the light of current knowledge on granulation and oscillations for other stars in Section 2.4.

2.2.2 *Small-scale magnetic heterogeneities: faculae, network, internetwork, and mixed-polarity magnetic fields (bright features)*

Faculae, from the Latin 'torch', are small-scale concentrations of bright patchy features with diameters of about 100–400 km, often found in the vicinity of sunspots in intergranular spaces. The term faculae refers to the brightening observed in the photosphere; at disc centre they appear as magnetic bright points. Their counterparts in the chromosphere (e.g. observed in Ca II H and K lines) are called plages. On the Sun, faculae and plages are typically found in magnetic active regions emerging within the latitudinal activity belts. A larger pattern of bright small-scale magnetic fields appears at borders of supergranular cells, as magnetic flux is swept towards the cell boundaries by convective horizontal flows. These concentrations form the magnetic network which is distributed almost uniformly across the solar disc, at any latitude and longitude. Thus, faculae, plage, and network heterogeneities are manifestations of photospheric and chromospheric small-scale magnetic fields which are not strong enough to form sunspots (Kiepenheuer 1953; Babcock & Babcock 1955; Solanki 1993). Here, we summarize the main characteristics of these magnetic bright features, focusing on the aspects most relevant to exoplanet transit spectroscopy.

Solar observations at high spatial resolution (sub-arcsec, corresponding to a few hundred kilometres on the solar surface) reveal that faculae are conglomerates of small features associated with kilogauss magnetic field concentrations (Fig. 2; Berger & Title 2001; de Wijn et al. 2009; Blanco Rodríguez & Kneer 2010; Keys et al. 2019). Both high-resolution observations (sub-arcsec) (e.g. Berger, Rouppe van der Voort & Löfdahl 2007; Kobel, Solanki & Borrero 2011; Romano et al. 2012; Kahil et al. 2017; Buehler et al. 2019) and medium-resolution observations (arcsec) (e.g. Ortiz et al. 2002; Yeo, Solanki & Krivova 2013; Criscuoli, Norton & Whitney 2017; Chatzistergos et al. 2019b) indicate that the radiative properties of faculae depend on their size, magnetic flux, degree of aggregation, wavelength, and position on the solar disc.

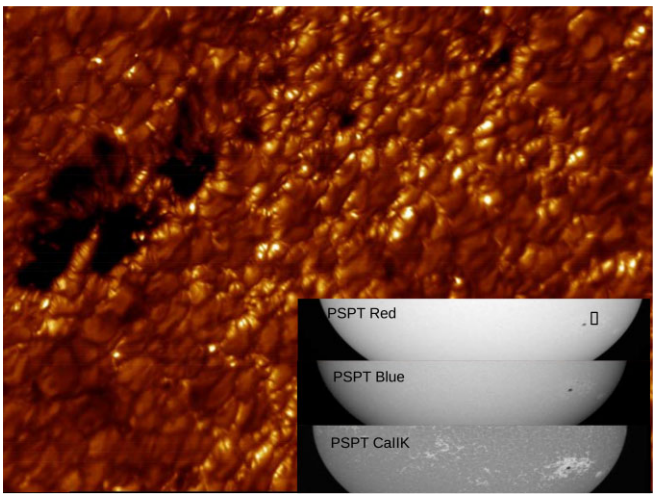

Figure 2 A portion of an active region observed at high spatial resolution in the *G* band (430.4 nm) with the *Swedish Solar Tower* (*SST*). Faculae appear as small (sub-arcsec), bright, elongated features. The same region, observed at medium resolution with the *Precision Solar Photometric Telescope* (*PSPT*) at Mauna Loa, appears as a bright patch, whose contrast is strongly dependent on the wavelength. The images were taken in the passbands 607.1±0.46 nm (*PSPT* red), 409.4±0.26 nm (*PSPT* blue), and 393.4± 0.27 (*PSPT* Ca II K). The black box in the *PSPT* red image shows roughly the field-of-view of the *SST G*-band image.

In the visible continuum, faculae are about 5–10 per cent brighter than the quiet Sun when observed close to the limb, while they are almost indistinguishable from the quiet photosphere, if not slightly darker, when observed close to the disc centre (Unruh, Solanki & Fligge 1999; Ahern & Chapman 2000; Ermolli et al. 2007; Yeo et al. 2013). In the IR, faculae appear darker than the surroundings (Sánchez Cuberes et al. 2002; Norris et al. 2017; Witzke et al. 2022).

Facular contrast reaches several tens of per cent in the cores of strong Fraunhofer lines, e.g. in the chromospheric Ca II H & K lines (e.g. Mehltretter 1974; Walton, Preminger & Chapman 2003; Rutten 2007; Chatzistergos et al. 2019b) and H-alpha wings (Dunn & Zirker 1973). A similar facular contrast is observed in certain molecular bands: the *CN* band at 388 nm (Chapman 1970; Sheeley 1971; Zakharov et al. 2005), the *G* band at 430 nm (Kitai & Muller 1984; Berger & Title 2001; Langhans, Schmidt & Rimmele 2004; Hirzberger & Wiehr 2005; Berger, Rouppe van der Voort & Löfdahl 2007), and the UV *OH* band at 313 nm (Berdyugina et al. 2003; Hirzberger et al. 2010). The dependence of the facular contrast on the line-of-sight magnetic field was found to be logarithmic (Kahil et al. 2017). The CLV of the quiescent photosphere brightness is less steep than that of faculae (Walton et al. 2003; Ermolli et al. 2010).

Magnetic network is also a manifestation of the photospheric magnetic field (e.g. Ortiz et al. 2002; Yeo et al. 2013; Criscuoli et al. 2017),

and, unlike faculae, which either are located in active regions or result from the decay of active regions, network is present at any latitude and longitude. Network also results from the aggregation of small-size magnetic elements, which are transported by surface convective motion to the edges of supergranules, thus forming a typical lattice structure particularly clear in chromospheric images (e.g. in near-UV images from the Solar Dynamics Observatory, SDO).

However, solar photometric measurements currently present two main difficulties. First, these measurements are affected by both finite spatial resolution and scattered light, which reduce the observed contrasts and affect the relation between physical and photometric properties. This problem affects both ground-based (Toner, Jefferies & Duvall 1997; Criscuoli & Ermolli 2008; Viticchié et al. 2010) and space-based observations (Mathew et al. 2007; Wedemeyer-Böhm & Rouppe van der Voort 2009; Yeo et al. 2013). Second, measurements are made relative to the quiet Sun background, whose definition is somewhat arbitrary, thus creating ambiguity and discrepancies between results presented in the literature (Peck & Rast 2015).

Moreover, the quiet Sun is not void of magnetic fields (see a review by Bellot Rubio & Orozco Suárez 2019). Weaker, predominantly horizontal fields occur as internetwork features flowing towards the network at supergranular borders (Livingston & Harvey 1971; Lites et al. 2008). Also, a large volume of mixed-polarity magnetic fields occur at scales which are unresolved with current instrumentation, but fortunately this rather hidden solar magnetism can be detected via the Hanle effect (Stenflo 1982; Faurobert-Scholl 1993; Stenflo, Keller & Gandorfer 1998; Berdyugina & Fluri 2004; Trujillo Bueno, Shchukina & Asensio Ramos 2004; Kleint et al. 2011; Shapiro et al. 2011). Whether these quiet-Sun magnetic features vary with the solar cycle (Kleint et al. 2010) or affect variations of the solar irradiance (Faurobert et al. 2020; Rempel 2020; Yeo et al. 2020a) is still not fully understood. High spatial resolution as well as high photometric and polarimetric sensitivity are therefore essential to improve our understanding of how solar magnetism affects irradiance variability.

Future observations with the upcoming *Daniel K. Inouye Solar Telescope* (*DKIST*, Rimmele et al. 2020) will have unprecedented spatial and temporal resolution, complemented by observations with space missions, e.g. the Interface Region Imaging Spectrograph (IRIS) and the Atacama Large Millimeter/submillimeter Array (ALMA). These data are expected to improve our understanding of the physics that underlies the radiative emission of quiet and magnetic regions, especially those occurring in the chromosphere and corona. Coordinated observations of *DKIST* with the recently launched Solar Orbiter are expected to improve our knowledge on polar faculae, whose properties, due to the ecliptic position of the Earth, are still poorly understood (Petrie, Criscuoli & Bertello 2021). These features have negligible effects on the solar irradiance received on the Earth, but they can play a major role for planets with orbits strongly inclined with respect to the rotation axis of the host star (Shapiro et al. 2016) or for stars with more abundant or stronger polar faculae. Observations with the upcoming *Solar Ultraviolet Imaging Telescope* (*SUIT*) onboard Aditya-L1 (Ghosh et al. 2016), planned for launch in 2023, will provide critical information on the contrasts and the CLV of the magnetic features in the UV between 200 and 400 nm.

2.2.3 Spot-like magnetic heterogeneities: umbra, penumbra, and pores (dark features)

Sunspots are the highest contrast features in the solar photosphere visible in the optical and NIR. The largest sunspot in recent history was observed in 1947 April with an area of more than 6000 millionths of the solar hemisphere area (MHS). Spots 10 times smaller are visible by the protected naked eye from the Earth. Spots larger than about 2000 MHS are regularly observed near solar activity maxima. These are several times larger than the Earth's area. There are several reviews of the literature related to physical properties of sunspots (e.g. Solanki 2003; Borrero & Ichimoto 2011). Here, we will only consider sunspot properties relevant to exoplanet transmission spectroscopy, and will refer to only a few important results.

Because of a strong magnetic field, up to 6 kG (e.g. Hale 1908; Harvey & Livingston 1969; Livingston et al. 2006; de la Cruz Rodríguez et al. 2013; van Noort et al. 2013; Siu-Tapia et al. 2017; Okamoto & Sakurai 2018), the bolometric intensity of sunspot umbra is 0.2–0.3 of that of the surrounding quiet (non-magnetic) photosphere, implying effective temperatures of 4000–4500 K. The intensity decreases with the umbral size (Mathew et al. 2007). An umbra larger than about 4000 km in diameter is usually (but not always) surrounded by a filamentary penumbra, which include both bright filaments and dark gaps and can be symmetric or partially asymmetric, depending on the spot complexity. The total spot area (including the penumbra) may exceed that of the umbra by up to a factor of five (e.g. Solanki 2003). The penumbra's bolometric contrast to the photosphere is about 0.8, i.e. its effective temperature is about 5500 K (average for bright filaments and dark gaps). A strongly inclined 0.5–1 kG magnetic field is responsible for the filamentary structure of the penumbra (Siu-Tapia et al. 2019). An umbra without a penumbra is known as a pore. Pores, which generally have relatively weak magnetic field strengths (Suetterlin 1998), are often observed to merge together and form larger spots with penumbra and structures called light-bridges, outlining the previous pores. The brightness of light-bridges is similar to that of the penumbra.

The sunspot size distribution is lognormal (Bogdan et al. 1988), with smaller spots occurring more frequently. This implies that the sunspot emergence is a fragmentation process, possibly of a large flux-tube anchored in the convection zone. The largest sunspot in a group occupies more than half the total area of all spots in a group, while the number of individual umbrae within a given group, N, increases with the group size as a power law $N \propto A_{\rm group}^{0.58}$ (Mandal et al. 2021). By extrapolating their results to significantly bigger spot groups, like those observed on very active stars, Mandal et al. (2021) conclude that such groups may be composed of multiple spots, with the biggest spot in a group occupying 55–75 per cent of the total group area. This, however, does not apply to spots formed by coalescence.

Sunspots exhibit various dynamic phenomena, such as magneto-convection, flows, oscillations, and short-term events. The umbral fine structure is best revealed in images taken in the passband centred at the TiO 706-nm molecular band (Berger & Berdyugina 2003). Remnants of convection within the umbra are observed as umbral dots, bright features of 100 km or less in diameter. In the photosphere, the intensity of umbral dots is significantly higher than that of the dark umbra, and their lifetimes span from minutes up to 2 h (Beckers & Schröter 1968; Adjabshirzadeh & Koutchmy 1983; Sobotka, Brandt & Simon 1997a; Riethmüller et al. 2008; Watanabe 2014; Kilcik et al. 2020). Longer-lasting umbral dots tend to be larger and brighter. As was found by Sobotka & Hanslmeier (2005), observed intensities of umbral dots correlate with local intensities of the umbral background. In terms of temperature, umbral dots were found on average hotter than the coolest area in the umbra by about 1000 K and cooler than the undisturbed photosphere by 500–1000 K, while individual umbral dots reached or even exceeded the average photospheric brightness and temperature. The density and brightness of umbral dots increase towards the umbral edge (Sobotka et al. 1997a; Yadav & Mathew 2018), and the brightness may vary quasi-periodically on time-scales of 3–30 min (Sobotka,

Brandt & Simon 1997b; Kilcik et al. 2020). Umbral dots extend up to the chromosphere where they are larger and more numerous (Kitai 1986). The horizontal outflow observed in penumbra (the Evershed effect) is reversed in the chromosphere, becoming an inflow in the penumbra and down-flow in the umbra. In addition, umbral flashes – sudden brightenings of the dark umbra – are observed in the upper atmosphere and reveal a further complexity of the dark umbra near the temperature minimum and lower chromosphere (Turova 1984; Henriques et al. 2020). Short-lived brightenings in the penumbra are associated with chromospheric micro-jets (Katsukawa et al. 2007).

Sunspots constitute active regions that emerge with an 11-yr solar cycle (22 yr if accounting for a magnetic reversal). A typical active region consists of larger leading and smaller trailing spots, pores, and faculae. The lifetime of sunspots linearly increases with their maximum size (the Gnevyshev–Waldmeier rule). The decay rate is about 11 MHS per day (Petrovay & van Driel-Gesztelyi 1997). This implies that most spots live less than a day, but larger ones can persist for months. It is not clear whether the sunspot lifetime and/or decay rate vary with the cycle. In the context of stellar and exoplanetary research, it is important to investigate cycle-dependent characteristics of sunspots and small-scale magnetic fields. This includes the contrast and relative areas of magnetic features and their spectral variations.

In view of this, a full-disc, synoptic capability is essential to achieve a comprehensive view of solar variability in all interlinked space and time domains. These domains include: global and temporal scales ranging from transient flare outbursts to cycle time-scales; spatial structures we refer to as active regions as delineated by spots, faculae, and plages; and field extrapolations into the corona and heliosphere that influence solar/stellar wind properties and, in turn, their potential impact on planetary atmospheres. The Synoptic Long-term Investigations of the Sun (SOLIS) facility of the National Solar Observatory is an example of an advanced instrument for global solar synoptic vector magnetic field investigations (Keller, Harvey & Giampapa 2003). A solar synoptic capability of this kind yields the partition of magnetic energy among the fundamental constituents of solar heterogeneity for the Sun-as-a-star on all time-scales and, in conjunction with *DKIST*, at all relevant spatial scales. Full-disc synoptic observations, uniquely characterized by long-term stability and continuity, provide a fundamental data base for the understanding of magnetic activity that is encountered in our Solar system, the planetary systems around Sun-like stars and the extrapolation of the solar example to other kinds of stellar hosts.

2.2.4 *Modelling solar observables*

Modelling solar observables requires, on one hand, a solid knowledge on physics of radiation, plasma, and magnetic processes and, on the other hand, accounting for instrumental degradation of the observed phenomena, especially for high-resolution imaging data.

From Table 1 and other observations, one can see that the uncorrected RMS contrast of granulation measured with space telescopes increases with increasing the telescope aperture, i.e. with increasing the spatial resolution. Thus, the distribution of the intensities is resolution-dependent. At low spatial resolution, the intensities show a distinct bi-modal intensity distribution, reflecting the different intensities of (bright) granular and (dark) intergranular space. With increasing spatial resolution of simulations, the bi-modality of the intensity distribution becomes less pronounced. For ground-based observations, achieving true contrasts is even more challenging because of the constantly varying terrestrial atmosphere causing image distortions on time-scales shorter than the data acquisition rates. In addition to adaptive optics corrections during observations, post-processing of imaging data is carried out with various image restoration techniques to achieve the diffraction limit of the instrument. After that, deconvolution similar to that applied to space data may allow achieving true contrasts of observed features. Alternatively, simulated and modelled observables can be convoluted with known instrumentation effects to be compared with the data. Both approaches have uncertainties and removing observing biases are to be improved. Modelling solar irradiance variability modulated by surface magnetism and comparing this with measurements are important for (i) reconstructing the solar irradiance variability (Chapman, Cookson & Preminger 2013; Chatzistergos et al. 2020a); (ii) validating atmosphere models employed in solar irradiance reconstruction (Fontenla, Avrett & Loeser 1993; Fontenla et al. 1999, 2006, 2009; Unruh et al. 1999; Penza, Caccin & Del Moro 2004; Ermolli et al. 2010); and (iii) understanding relations observed between various magnetic-activity indices (Choudhary et al. 2020; Ayres 2021; Clette 2021).

Understanding the physics of faculae in terms of their magnetic structure, radiative transfer, and dynamic substructure is important for predicting their effects at different wavelengths. Here, both realistic 3D simulations and a detailed modelling of opacities are of great importance. For example, Schüssler et al. (2003) showed why solar magnetic flux concentrations are bright in molecular bands using radiative magnetoconvection simulations and proper molecular opacities in the presence of magnetic fields by Berdyugina et al. (2003). This was followed by similar work by Keller et al. (2004), Steiner (2005), and De Pontieu et al. (2006).

Similarly, understanding physics of sunspots and obtaining their realistic models is helpful for modelling starspot effects on other stars at different wavelengths. Rempel, Schüssler & Knölker (2009b) discussed the magnetoconvective processes that occur in a sunspot and provided the first insights into penumbral filament formation. Subsequently, Rempel et al. (2009a) simulated circular sunspots with full-fledged penumbrae that reached such levels of realism that the simulated intensity images were almost indistinguishable from observed structures (see Fig. 3). However, physical drivers for forming sunspot penumbra are still not fully understood (Rempel 2012).

The fine structure and large range of temperatures in sunspots results in a dramatic difference of their spectra as compared with that of the quiet photosphere. In particular, spectra of the dark umbra are similar to those of M dwarf's quiet photospheres, with strong molecular bands from metal hydrides and oxides (e.g. MgH, CaH, FeH, CrH, SH, TiO, and VO). In addition, CNO-based molecules (e.g. CH, NH, OH, CO, CN, and C2) form in both the quiet photosphere and chromosphere as well as in sunspots (see an overview by Berdyugina 2011). Magnetic effects in these molecules are currently well understood and implemented in the HotMol numerical library. They are employed for measuring and modelling magnetic fields on the Sun and other stars. Other molecules have been detected in sunspots in the NIR, e.g. H_2O (Wöhl 1971; Polyansky et al. 1997). These molecular bands, along with strong atomic (resonance) lines, are spectral features that are being detected in exoplanetary atmospheres. Thus, modelling spectra of sunspot substructures is important for the decontamination of composite star–planet spectra.

2.2.5 *Observations of Venus and Mercury transits of the Sun as a star*

Photometric observations of exoplanets across their host stars contend with the many stellar-variability issues discussed here,

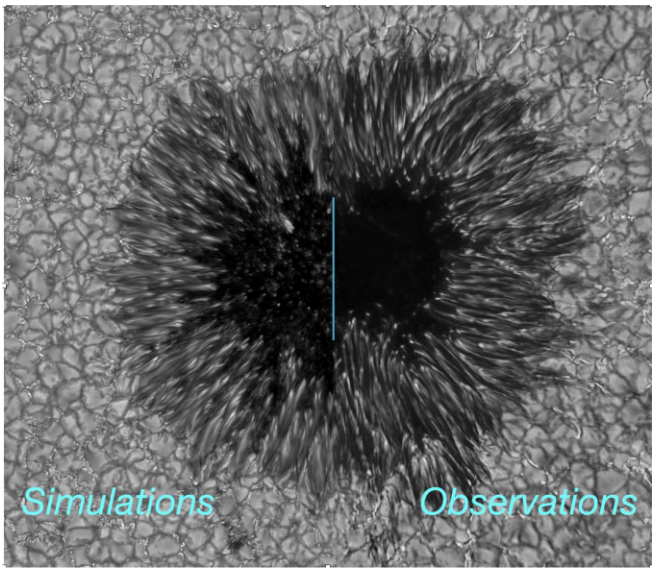

Figure 3 MURaM simulations of a sunspot by M. Rempel (left half of the plot) versus *Dunn Solar Telescope* observations by F. Wöger (right half of the plot). The vertical blue line separates the simulated image from the observed one. Credit: F. Wöger.

including global oscillations, convection, granulation, magnetically active regions, and CLVs. In the case of the Sun, the spatially averaged variations due to oscillations, granulation, and convection cause $\sim 10^{-4}$ variations in spatially and spectrally integrated light (Kopp 2016). For comparison, the transit of the Earth across the solar disc viewed from a distant system would have a maximum transit depth of $\sim 8 \times 10^{-5}$, and can thus be masked by the background solar variability.

Fortunately, the time-scales of solar variability and planetary transits differ sufficiently that transits of Earth-sized planets across Sun-like stars would, in fact, be detectable since they affect different portions of the stellar light-curve power spectrum. Solar variability due to oscillations, convection, and granulation primarily occurs on time-scales of several minutes, while active regions, such as sunspots and faculae, vary on multiday time-scales. In contrast, planetary transits occur on ∼1- to 10-h time-scales. This time-scale difference makes the exoplanet detection of Earth-like planets across solar-like stars feasible via photometric observations.

Observations of Mercury transits across the solar disc as viewed from the Earth demonstrate the difficulties in discovering small exoplanets orbiting G-type stars via photometric measurements of the stellar light curves during planetary transits. Four Mercury and two Venus transits have been observed by the total irradiance monitor (TIM) on NASA's Earth-orbiting Solar Radiation and Climate Experiment (SORCE) mission (Kopp 2021). This instrument measures the TSI, the spatially and spectrally integrated radiant solar energy flux incident at the top of the Earth's atmosphere. This essentially views the Sun as a star. Instrument sensitivities are $\sim 4 \times 10^{-6}$, making the TIM inherently capable of detecting both intrinsic solar variabilities and solar-disc transits by inner planets.

Viewed from the proximity of the Earth, Venus-transit light curves have large transit depths ($\sim 10^{-3}$), making such transits unambiguous from the smaller effects of background solar oscillations and convection. While detections of exoplanet signals typically involve several transits, these snapshots of stellar variability allow for their detailed study. The TIM radiometric measurements of the 2012 Venus

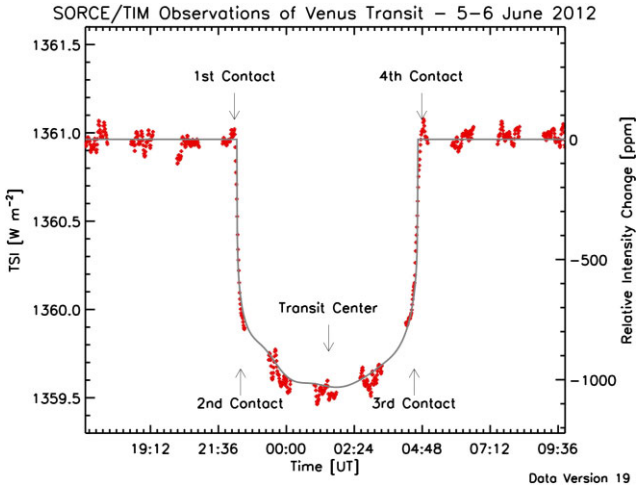

Figure 4 The SORCE/TIM measured a decrease in the TSI (red dots) as Venus transited the Sun on both 2012 June 5–6 (shown) and 2004 Jun 8. In agreement with predictions (grey curve) accounting for solar limb darkening and the SORCE position, the incident sunlight decreased by $\sim 10^{-3}$ during the transits, which is comparable to the effect of a medium-sized sunspot in TSI. The gaps in the plotted data are from times when the SORCE spacecraft was in the Earth's shadow and could not view the Sun. All four transit contact points, covering both ingress and egress, were observed in the shown Venus transit. The increases in brightness near ingress and egress during the transit are due to solar limb darkening, which makes the centre of the solar disc brighter than the edges and hence the transit-depth greater when Venus is nearer to disc centre. The small fluctuations in brightness on short time-scales are from normal solar convection and oscillations, and can be seen in the unocculted times both before and after the transits. From Kopp (2021).

transit are shown in Fig. 4. Even viewed from the Earth, Mercurial transits are much smaller. These have $\sim 4 \times 10^{-5}$ transit depths in integrated light, or approximately half the light-curve depth that an Earth-sized exoplanet would have when transiting a G-type star in a distant planetary system. These transits are largely masked by the ever-present background solar variability (see Fig. 5).

With such solar-variability masking, multiple transit observations are required for the unambiguous detection of an Earth-sized exoplanet across a solar-like star. Knowledge of the amplitudes and time-scales of the host star's intrinsic variability is also necessary for detecting small exoplanets via transits. Measurements of the Sun provide such knowledge for the most 'Sun-like' star known, and actual radiometric transit observations of the Sun's innermost planet, Mercury, exemplify the issues expected for exoplanet discoveries of transits of Earth-sized planets across host G-type stars.

2.2.6 Our finding: Finding 1.1

From this analysis, we draw the following findings:

Summary

The Sun provides the benchmark for stellar studies. Studying the spatial, spectral, and temporal variations of stellar surface structures is necessary for understanding the impact of analogous structures on transmission spectroscopy of exoplanets.

Capability needed

More work is needed to study spatially resolved properties of the Sun and their variations on time-scales from minutes to years at optical and IR (0.3–5 μm) wavelengths. Theoretical and observational perspectives are needed to further our understanding of both granules and active regions. For both granules and active regions, key

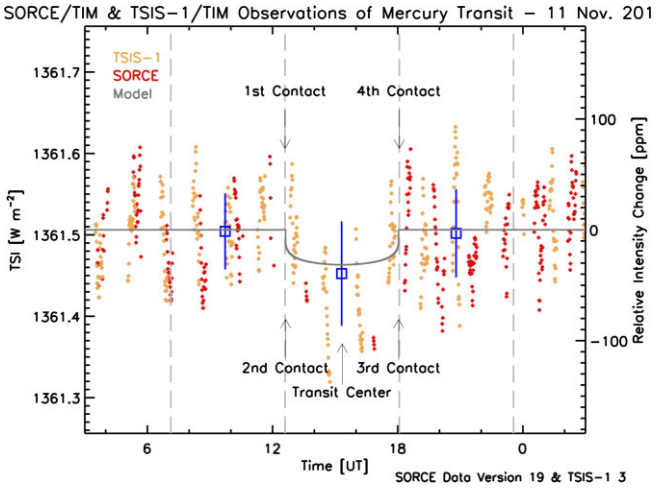

Figure 5 Both the SORCE/TIM and the Total and Spectral Solar Irradiance Sensor (TSIS)-1/TIM observed the 2019 November 11 Mercury transit. The high-cadence TSIS-1/TIM TSI values are plotted in orange and SORCE (scaled to the TSIS-1 values) in red. The scatter in these high-cadence TSI values is almost all due to actual solar variability. The blue boxes and whiskers are, respectively, the averages and standard deviations of equal-length time regions before, during, and after the transit from both instruments. The grey curve is the predicted signal for a limb-darkened solar disc viewed from the TSIS-1. As with three prior Mercury transits observed by the SORCE, the transit signal is likely there but would not be readily apparent without knowing where to look, since the $\sim 10^{-4}$ background solar variations mask the 3.7×10^{-5} expected transit-depth signal. From Kopp (2021).

parameters to understand better are sizes and contrasts at optical and NIR wavelengths. For active regions, key parameters to study also include locations, lifetimes, and vertical structure variations from the photosphere to the chromosphere.

Capability today

High-resolution observations of the Sun are available for fine-structure studies of photospheric and chromospheric inhomogeneities, but their wavelength range is limited. Advanced codes necessary solar and stellar magnetic studies are available, such as the HotMol numerical library for spectral synthesis using realistic molecular opacities in the presence of magnetic fields (Berdyugina et al. 2000, 2003, 2005; Berdyugina & Solanki 2002). The TSI of the Sun can be modelled accurately with codes such as SATIRE (Fligge, Solanki & Unruh 2000; Krivova et al. 2003; Yeo et al. 2014a) and MURaM (Vögler et al. 2005; Rempel et al. 2009b; Beeck et al. 2013a, b). 3D MHD codes, such as MURaM (Vögler et al. 2005), COnservative COde for the COmputation of COmpressible COnvection in a BOx of L Dimensions, L = 2,3; (CO5BOLD; Freytag, Steffen & Dorch 2002; Ludwig et al. 2009; Freytag et al. 2012; Bonifacio et al. 2018; Salhab et al. 2018), and Bifrost (Gudiksen et al. 2011), can be used to produce realistic simulations of the solar photosphere and chromosphere, including active regions and sunspots.

Mitigation in progress

When fully operational, *DKIST* will have unprecedented spatial and temporal resolution for observations of the solar photosphere and chromosphere at wavelengths of 0.4–5 μm (Rimmele et al. 2020). The augmentation of *DKIST* observations with full-disc, synoptic observations, such as those from SOLIS (Keller et al. 2003), will provide a global context that is continuous in space and time and, with *DKIST* observations, will extend across all relevant spatial scales. This complementary approach will yield a comprehensive view of solar activity and, by extension, the magnetic activity in Sun-like hosts of planetary systems.

2.3 3D stellar modelling: from the Sun to other stars

Since the first time-dependent 3D simulations of the Sun (e.g. Nordlund 1982, 1984, 1985) and other stars (e.g. Atroshchenko, Gadun & Kostyk 1989a, b; Dravins & Nordlund 1990a, b; Nordlund & Dravins 1990), stellar 3D models have been improved in terms of the spatial resolution of the numerical grid, the extent of the computational box, and the included physical processes. As all these improvements compete for limited computational resources, some models are geared towards either high resolution or covering large spatial scales (even up to global simulations of giant stars, Freytag et al. 2002). Others aim for a high degree of realism by including as many of the relevant physical processes as possible. The extension from pure HD to ideal MHD for 3D models of the lower solar atmosphere was a costly but necessary step in the early 2000s. Today, 3D MHD models are considered the standard for solar simulations and are increasingly applied to simulations of other stars.

The selected compromise between number of grid cells and included physics is typically determined by the intended scientific application. For instance, simulations of sunspots or even active regions require large computational boxes, but the minimum spatial resolution of the computational grid is constrained by the spatial scales that need to be resolved adequately, e.g. for realistically reproducing the photospheric flow field. The resulting number of grid cells then limits the detail and extent to which physical processes can be modelled. Another example is the extension of models in height into the chromosphere or even the corona. In these layers, many assumptions that can be made for photospheric conditions are no longer valid. For instance, the ionization of hydrogen is no longer in statistical equilibrium and instead requires detailed calculations that are computationally expensive (Carlsson & Stein 2002; Leenaarts & Wedemeyer-Böhm 2006; Leenaarts et al. 2007) despite using simplified model atoms. Nonetheless, these improvements are necessary for realistic simulations of the upper atmosphere and thus for the interpretation of spectral lines and phenomena originating in these layers. An example is the widely used 3D model of an enhanced network region by Carlsson et al. (2016) that has been produced with the Bifrost code. Depending on the exact application, even otherwise seemingly quiescent conditions in the solar photosphere can require models with a high degree of realism. This is because small-scale variations of the atmospheric structure in a line-forming layer and its dynamical (and magnetic) properties can have a notable impact on the resulting spectral line shapes. For instance, 3D simulations have resulted in the more precise determination of chemical abundances (see e.g. Steffen & Holweger 2002; Asplund, Grevesse & Sauval 2005; Asplund, Grevesse, Sauval & Scott 2009) and insights into the formation of the Hα line in the solar chromosphere (Leenaarts, Carlsson & Rouppe van der Voort 2012).

In the context of observing the atmospheres of exoplanets, numerical simulations of the atmospheres of host stars can support the interpretation of such observations and can also aid the design of adequate observing and data reduction strategies. The first step towards producing numerical simulations for this purpose is thus to define the wanted spectral diagnostics and the required precision of the anticipated measurements. These requirements then determine the needed set-up and degree of realism of the simulations. The second step is to see how to produce these models based on already existing models (discussion in the following sections). It should be emphasized that the production of advanced 3D nu-

merical simulations of stellar atmospheres is a computationally very expensive endeavour that requires much computational time on high-performance-computing infrastructure. Substantial high-performance-computing resources are thus needed as an integral part of the preparatory phase of the scientific strategy outlined here.

In the following sections, we detail the available state-of-the-art non-magnetic and MHD 3D model grids (Section 2.3.1) and modelling considerations as they relate to heterogeneities due to plasma motion (granulation and oscillations, Section 2.3.2), small-scale bright magnetic features (faculae and network, Section 2.3.3), and dark spot-like magnetic heterogeneities (umbra, penumbra, and pores, Section 2.3.4).

2.3.1 *Available non-magnetic model grids*

Systematic grids of local 3D model stellar atmospheres have been produced with several radiation MHD codes. The main codes used to produce grids of non-magnetic models for studying stellar near-surface convection are STAGGER (Stein & Nordlund 1998; Magic et al. 2013; Trampedach et al. 2013), CO5BOLD, and MURaM. Table 2 lists the range of spectral types, surface gravities, and metallicities covered by some of the prominent model grids. We refer the reader to Beeck et al. (2012) for a detailed comparison of the codes. Naturally, all three listed codes have been also used in numerous studies, sometimes simulating stellar atmospheres outside the listed grids. For example, CO5BOLD has been used to simulate M stars with effective temperatures down to 2500 K (Wende, Reiners & Ludwig 2009; Wedemeyer, Ludwig & Steiner 2013). These model grids are complemented by small grids of local, 3D stellar atmospheres including magnetic fields (Beeck et al. 2015a, b; Salhab et al. 2018) and 3D MHD models of M-dwarf atmospheres with a chromosphere (Wedemeyer et al. 2013).

In sum, there exists today a large range of 3D stellar non-magnetic models ready for future analysis. The grids cover main-sequence stars with $3600 < T_{\rm eff} < 7000$ (Table 2), spanning the parameters of more than 90 per cent of known exoplanet host stars.[3]

However, the models include varying degrees of realism in terms of set-up, metallicity, the inclusion of an upper atmosphere, and more. Unfortunately, these models do not yet include the effect of magnetic fields and simulations of stellar magnetic features are currently only available for several values of effective temperature (see Sections 2.3.3–2.3.4). The simulations of magnetic features on stars with a wide range of effective temperatures, metallicities, and surface gravities (in particular, covering the fundamental parameters of known cool stars hosting exoplanets, i.e. from early F- to late M-dwarfs and metallicity values from at least -1 to $+0.5$) are urgently needed for assessing the magnetic component of stellar contamination of transmission spectra. While the above mentioned simulations typically cover only a small part of a stellar atmosphere, they are ready to serve as the basis for the production of models in the context of exoplanet observations, given sufficient investments in the computational and human resources required for these efforts.

2.3.2 *Granulation and oscillations in stellar models*

Granulation

The intensity contrast of granules defines the amplitude of the granulation-driven contamination of the transmission spectrum and, thus, its accurate modelling for a broad class of stars is of special importance.

The first 3D simulations of granulation on the Sun were done by Nordlund (1982, 1984, 1985). Soon after that, Nordlund & Dravins (1990) extended the solar simulations to other Sun-like stars: Procyon F5 IV–V, α Cen A G2V, β Hyi G2IV, and β Cen B K1V ($T_{\rm eff}$ between 5200 and 6600 K), and further computed synthetic Fe line profiles and their bisectors to compare with observations. These early simulations established the strong dependence of granular velocity, lifetimes, and size on the spectral type.

Fig. 6 shows examples of granulation on stellar surfaces as bolometric intensity maps with the RMS intensity contrast given in each frame. The upper panel shows simulations of a red supergiant and an asymptotic giant branch (AGB) star. The granulation scale in such stars is comparable to the size of a star so that only several very prominent (note the very high values of the RMS intensity contrast) granules are present on their surfaces. Therefore giant stars can be simulated using a star-in-a-box approach, in which the entire stellar atmosphere is included in the simulation box. The remaining panels in Fig. 6 present simulations of dwarfs for which the surfaces contain many granules. For such stars, the star-in-a-box approach would demand a very fine spatial mesh to resolve the granulation, which is presently not feasible. Thus, they are presently simulated using a box-in-a-star approach, in which the simulation box covers only a small part of stellar atmosphere. The RMS contrast generally increases with increasing effective temperature; in other words, for hotter stars there is generally a larger contrast variation between the bright (up-welling) granules and dark (down-flowing) intergranular lanes. The exception from this rule is ultracool stars and substellar objects, e.g. brown dwarfs (see middle and right-hand panels in the bottom row) as well as hot A-stars (see left-hand and middle panels of the second row).

For a solar effective temperature and surface gravity, the RMS contrast increases with decreasing metallicity (Magic et al. 2013; Witzke et al. 2023). The RMS granular contrast over a wide range of effective temperatures, surface gravities, and metallicities is given by Tremblay et al. (2013). They find that the intensity contrast correlates well with the Mach number, the ratio of flow and sound speeds, at the stellar surface over the full range of the Hertzsprung-Russell (HR) diagram. This reflects the fact that both the Mach number and the intensity contrast are a measure of the vigour of convection.

The key points from these studies are as follows:

(i) The temperature contrast, and therefore intensity contrast, between granules and intergranular lanes depends strongly on the stellar surface temperature. Hotter stars have higher temperature contrast. The temperature contrast is weakly dependent on metallicity. For a solar effective temperature and gravity, the contrast decreases with metallicity.

(ii) Granule size increases with temperature and decreases with surface gravity. Thus, hotter stars with lower surface gravities have larger granules than cooler stars with higher surface gravities. In cooler stars with very low surface gravities (e.g. supergiants), granule sizes can be comparable to the stellar radius. Like the temperature contrast, granule size also shows a weak dependence on metallicity. At the same surface temperature, decreasing the metallicity results in smaller granules.

Oscillations

Predicting the amplitudes of oscillations on other stars remains challenging (see e.g. Aerts 2021, for a recent review). Instead, a number of scaling relations using fundamental stellar properties have been proposed (Kjeldsen & Bedding 2011; Samadi et al. 2012). For

[3]NASA Exoplanet Archive, accessed 20 Feb 2023 at: https://exoplanetarchive.ipac.caltech.edu/.

Table 2. Available non-magnetic 3D model grids.

Code	$T_{\rm eff}$ (K)	log g	[Fe/H]	Reference
STAGGER	4185–6901	2.2–4.74	0.0	Stein & Nordlund (1998) and Trampedach et al. (2013)
	4000–7000	1.5–5.00	-4.0–0.5	Magic et al. (2013)
CO5BOLD	3600–6750	1.0–5.0	-3,-2,-1,0	Ludwig et al. (2009) and Freytag et al. (2012)
MURaM	3690–6893	4.3–4.826	0.0	Vögler et al. (2005), Rempel et al. (2009b), Beeck, Schüssler & Reiners (2011), and Beeck et al. (2013a, b)

example, Kjeldsen & Bedding (2011) suggested

$$A_{\rm vel} \propto \frac{L\tau_{\rm osc}^{0.5}}{M^{1.5}T_{\rm eff}^{2.25}} \quad (1)$$

for velocity amplitudes, and

$$A_{\lambda} \propto \frac{L\tau_{\rm osc}^{0.5}}{\lambda M^{1.5}T_{\rm eff}^{2.25+r}} \quad (2)$$

for intensity amplitudes observed at a typical wavelength λ. Here L, M, $T_{\rm eff}$, and $\tau_{\rm osc}$ refer to luminosity, mass, effective temperature, and mode lifetime, respectively. The exponent r takes slightly different values in literature (see Kjeldsen & Bedding 2011, and references therein). The second scaling relation has been extensively tested and modified based on *Kepler* data (e.g. Huber et al. 2011; Stello et al. 2011; Mosser et al. 2012; Corsaro et al. 2013; Kallinger et al. 2014). The oscillation amplitudes were later found to be also metallicity-dependent by Yu et al. (2018) and Vrard et al. (2018). These studies showed that, all else being equal, metal-rich stars tend to have larger oscillation amplitudes, in agreement with theoretical predictions (Houdek et al. 1999; Samadi et al. 2010a, b).

These scaling relations have been used to estimate the significance of oscillation signals against granulation background and noise to prioritize the asteroseismic target selection for the *Kepler*, *K2*, and *Transiting Exoplanet Survey Satellite* (*TESS*; Ricker et al. 2015) space missions (Chaplin et al. 2011a, 2015; Schofield et al. 2019). These efforts have shown that the photometric oscillation amplitudes are very low compared with granulation and noise levels in the Fourier spectra of late K- and M-type main-sequence stars.

2.3.3 *Faculae and network in 3D stellar models*

Although HD simulations of near-surface granulation have been achieved by a number of groups, only two codes have been used to simulate magnetic fields on stars other than the Sun – MURaM (Beeck et al. 2011, 2015a, b) and CO5BOLD (Steiner et al. 2014; Salhab et al. 2018). The MURaM papers covered the spectral types F3V, G2V, K0V, K5V, M0V, and M2V, while the CO5BOLD ones covered the types F5V, G2V, K2V, and K8V. In both cases, the authors computed network or facular fields, starting with vertical homogeneous fields as an initial condition. Salhab et al. (2018) used an initial strength of 50 G for all of the runs, while Beeck et al. (2011), Beeck et al. (2015a), and Beeck et al. (2015b) used initial strengths of 20, 100, and 500 G, respectively.

Fig. 7 shows the bolometric intensity maps of models computed by Beeck et al. (2015a). The F-, G-, and K-type models show the typical bright magnetic elements familiar from solar network and plage regions. Only when the initial magnetic field strength is taken to be a copious 500 G, do a few dark features appear among the mostly bright magnetic structures. In contrast, in the M2V star (and in the M0V star – not shown in Fig. 7), dark magnetic structures frequently form in the 100-G runs. In the 500-G runs, however, large dark structures dominate, and there are essentially no bright magnetic structures left.

One remarkable behaviour of the magnetic flux concentrations that form in these simulations is that their magnetic field strength, measured at the surface with mean visible optical depth of unity ($\langle\tau_{500}\rangle = 1$), is only weakly dependent on stellar spectral type and initial magnetic field strength (for fixed solar surface gravity and metallicity). It increases towards later spectral types, from 1250 G for the F5V to 1440 G for K8V (Salhab et al. 2018), and increases with increasingly available magnetic flux (Beeck et al. 2015a) but remains in the range of kilogauss field strength.

Steiner et al. (2014) and Salhab et al. (2018) found that the presence of small-scale magnetism (e.g. magnetic bright points) increases the bolometric intensity and flux in all their investigated models compared with equivalent magnetic field-free models. The surplus in radiative flux of the magnetic over the magnetic field-free atmosphere increases with increasing effective temperature, $T_{\rm eff}$, from 0.47 per cent for spectral type K8V to 1.05 per cent for the solar model, but decreases again for effective temperatures greater than solar. This agrees with the results of Beeck et al. (2015a), as shown in Fig. 7. Thus, for mean magnetic flux densities of approximately 50 G, we expect the small-scale magnetism of stars with spectral types F5V – K8V to produce a positive contribution to their bolometric luminosity (see also Bhatia et al. 2021, for the first simulations of small-scale dynamo in stars of various spectral classes). While the overall effective temperature changes in the presence of small-scale magnetic features can be small, the flux increases are strongly wavelength dependent, with particularly strong enhancement in the UV. The enhancement also depends strongly on the disc position so that magnetic activity is expected to noticeably affect CLVs of emergent intensity.

All the simulations described above have been performed for the solar value of the metallicity. However, metallicity has a strong effect on the opacity so that one can expect that the visibility of facular features strongly depends on the metallicity (Witzke et al. 2018, 2020). Furthermore, most hot Jupiters are discovered around stars with a higher metallicity than the Sun (e.g. Osborn & Bayliss 2020). All in all, accounting for a metallicity effect on magnetic features is crucial for a proper characterization of magnetic contamination and, thus, 3D MHD simulations of magnetized stellar atmospheres for a broad range of metallicities are urgently needed.

The key points from these studies are as follows:

(i) The presence of small-scale magnetic fields on stellar surfaces leads to the formation of network and faculae, which can lead to strong contamination signals in transmission spectra.

(ii) Small-scale magnetic features typical of network and faculae (plage) may be both bright and dark, depending on the spectral type of the star. In M stars, very few bright features form and the change in radiative flux is largely dominated by the darker magnetic features.

(iii) Currently very little is known about the effect of metallicity on the facular contrast. While simplified 1D modelling indicates that

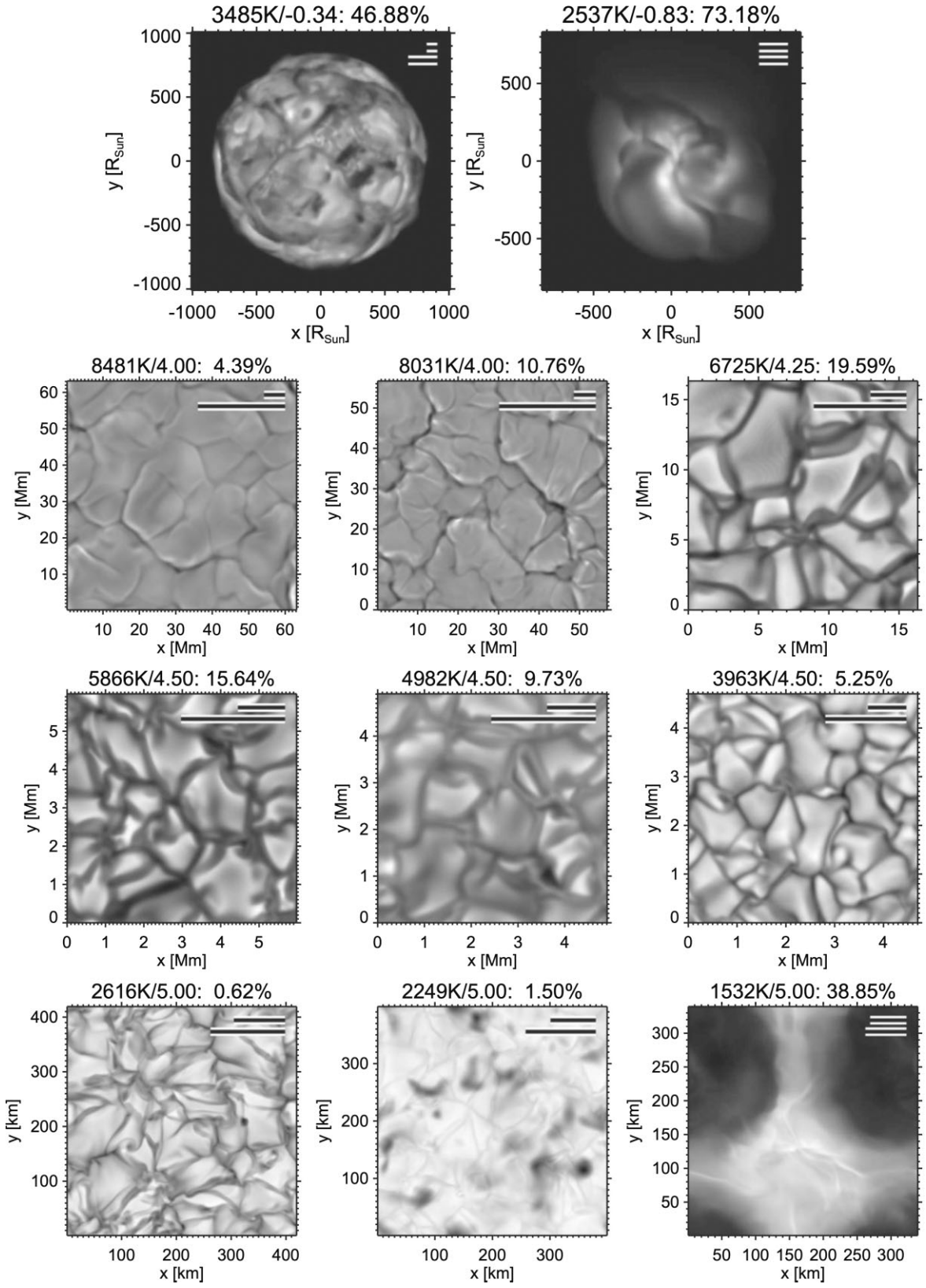

Figure 6 Instances of the normalized, time-averaged, and frequency-integrated (bolometric) intensity (grey scale) from various simulated solar-metallicity stellar surfaces with CO5BOLD. Top row: Global models of a red supergiant and an AGB star of low surface gravity. Following rows: Local models of main-sequence stars and brown dwarfs. The title lines show the effective temperature, the decadic logarithm of the surface gravity in cm s^{-2}, and the relative bolometric intensity contrast averaged over a representative time span. The length of the upper bar in the top right of each panel is 10 times the surface pressure scale height. The bar below is 10 times the pressure scale height but measured 3 pressure scale heights below the surface. From Freytag et al. (2012).

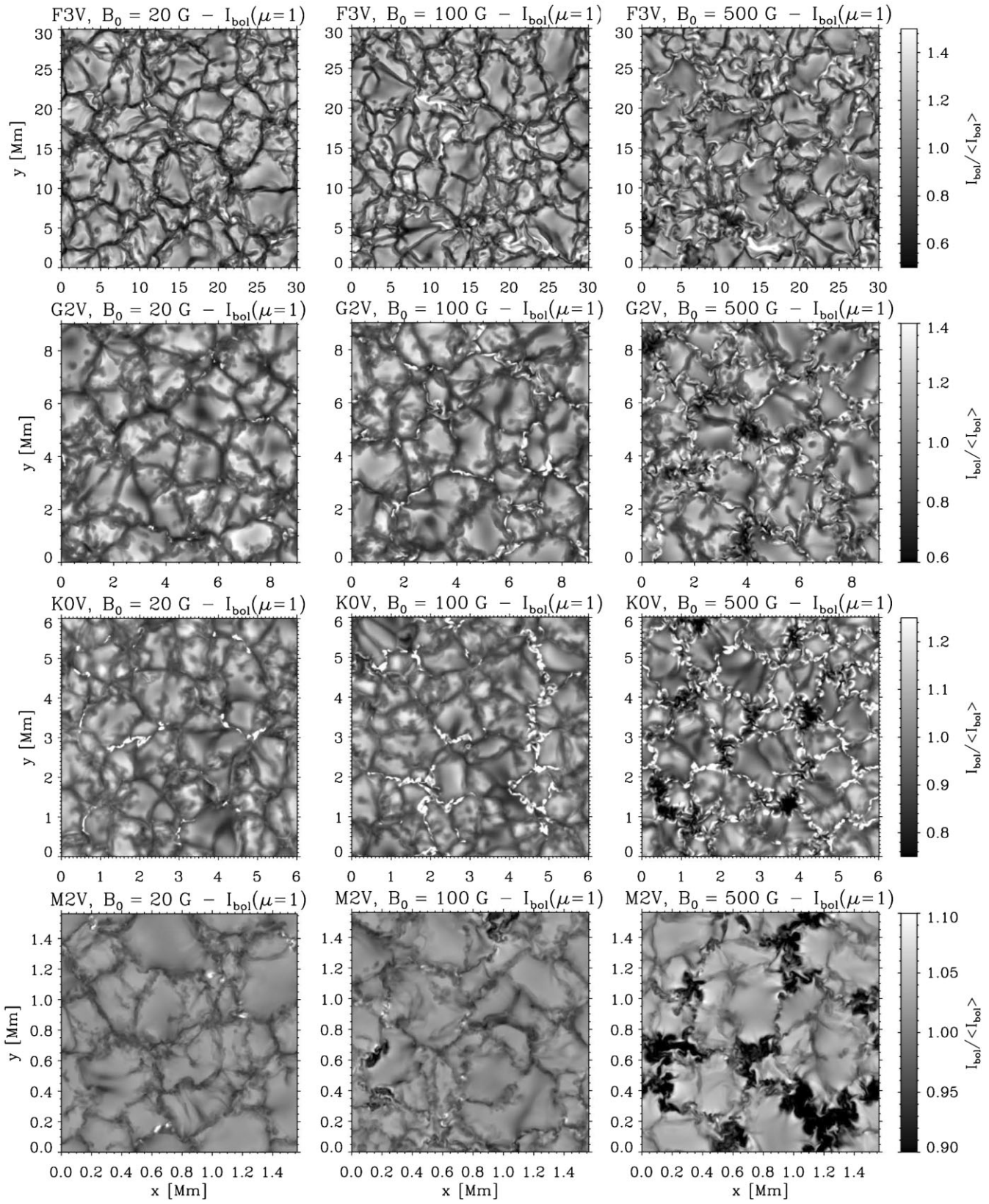

Figure 7 Maps of the vertically directed bolometric intensity for 12 of the 18 magnetic simulation runs. Note that the scale of the normalized intensity is adjusted for each spectral type for improved image contrast, and the grey-scales saturate at the limits indicated for each row. As the average magnetic field strength increases, more magnetic bright points are visible within the intergranular lanes; the quantity of magnetic bright points also increases with effective temperature, but decreases again at temperatures greater than solar. From Beeck et al. (2015a).

facular contrasts might strongly depend on the metallicity (Witzke et al. 2018, 2020), a more realistic 3D MHD modelling of faculae on stars with different metallicities is urgently needed.

2.3.4 Umbra, penumbra, and pores in stellar models

Models featuring spots have attained increasing levels of realism in the last decade (e.g. Rempel et al. 2009a, b; Rempel 2012). Building upon the first 3D sunspot simulation in a slab geometry using the MURaM code (Rempel et al. 2009b), the current state-of-the-art MHD simulations with the MURaM code produce sunspot intensity images, complete with expansive penumbral filaments that are often indistinguishable from observations (see e.g. Fig. 3).

Turning to stars other than the Sun, Panja, Cameron & Solanki (2020) recently conducted the first radiative MHD simulations of spots, focusing on their umbral properties. They modelled G2V, K0V, and M0V stars and found the temperature contrast between the umbra and the surrounding photosphere to be around 1400 K for the G2V star, 650 K for the K0V star, and 350 K for the M0V star. The umbral bolometric intensities relative to the quiet star intensities are 0.3, 0.5, and 0.7 for the G2V, K0V, and M0V stars, respectively. The umbral magnetic field strengths are all in the range of 3–4.5 kG. These simulations focused on the umbra; however, spots on the Sun are known to be dominated by the penumbra, with a typical umbra:penumbra areal ratio on the Sun of 1:4 (Solanki 2003). Due to the slab geometry chosen by Panja et al. (2020) to keep computing costs manageable, the penumbra is underrepresented in these simulations. Future studies will expand on this work to understand the properties of spots with expansive penumbral filaments (Fig. 8 shows such simulated spots for the spectral types G2V, K0V, and M0V), including intensity contrasts of spots at different wavelengths and different disc positions (Panja et. al, in preparation).

The key points from these studies are as follows:

(i) Modern 3D MHD simulations of sunspots excel at producing sunspot intensity images that essentially mirror solar observations.

(ii) Only recently have studies produced 3D MHD simulations of spots on other stars. Much work remains to be done in this arena, but the existing results reveal a trend of decreasing spot–photosphere temperature contrast for later spectral types, matching observations (e.g. Berdyugina 2005).

2.3.5 Our finding: Finding 1.2

From this analysis, we draw the following findings:

Summary

More modelling work is needed to understand how the fundamental parameters of stars other than the Sun govern their magnetic fields and the associated properties of their surface inhomogeneities. In accordance with observations, simulations show that many lower activity stars, such as exoplanet hosts that might be deemed as 'low risk' for transmission spectroscopy in terms of stellar activity, are facula-dominated (Shapiro et al. 2014; Nèmec et al. 2022). However, little is known on how facular contrasts and coverages depend on stellar activity levels and fundamental parameters, such as metallicity and surface gravity. Both observing and modelling the fine structure of spots on stellar surfaces remain a challenge.

Capability needed

MHD simulations of magnetic features and spectral synthesis for a larger range of stellar parameters, such as lower and higher metallicity, cooler temperatures, various stellar ages and/or activity levels are needed. In particular, we need to understand how facular and spot contrasts and coverages depend on stellar fundamental parameters and activity. We need to be able to infer the observational properties of photospheric and chromospheric features from easily accessible grids of simulations or, ideally, from simulations tailored to particular high-priority exoplanet host stars. Importantly, models of cool stars ($T_{\rm eq} < 3700$ K) are necessary to understand the hosts of many exoplanets that are high priority for follow-up.

Capability today

A limited amount of MHD radiative simulations exist now. Thus, atmospheric structures of various magnetic features are often represented by 1D radiative equilibrium models (e.g. PHOENIX; Husser et al. 2013), but they fail dramatically for bright features (e.g. faculae; Norris et al. 2017; Witzke et al. 2022). 3D radiative MHD codes like MURaM (Vögler et al. 2005) and CO5BOLD (Ludwig et al. 2009) have been used to simulate photospheric magnetic fields and surface features for a few (<10) FGK and early-M main-sequence spectral types (Beeck et al. 2012, 2013a; Freytag et al. 2012; Bhatia et al. 2022), but physical constraints on the fine structure of spots (umbra and penumbra) are still not understood.

Mitigation in progress

Groups have recently used the 3D radiative MHD code MURam to simulate starspots on G2V, K0V, and M0V stars (Panja et al. 2020). Others have also used MURaM to study facular contrasts of G2V stars with varying magnetic field strengths (Witzke et al. 2022, 2023).

2.4 Observations of stars other than the Sun

2.4.1 Granulation and oscillations in other stars

While plasma-driven processes like granulation and oscillations cannot yet be spatially resolved in stars other than the Sun, their impact in other stars can still be detected in unresolved observations. These include extremely precise radial velocity and spectral line profile measurements (not reviewed here) as well as photometric time-series measurements (i.e. light curves), particularly from space-based observatories such as the *Convection Rotation and planetary Transits* (*CoRoT*; Auvergne et al. 2009) space telescope, the *Kepler*/*K2* space telescope, and *TESS*. For example, *Kepler* observations of thousands of red giant stars have yielded detailed asteroseismic analyses of the oscillation frequencies of these stars, oscillations which are driven largely by surface convection. This enables accurate determination of bulk stellar properties, such as mass and radius, as well as detailed internal stellar structure and rotation profiles (see e.g. Chaplin et al. 2011b; Huber et al. 2011; Mathur et al. 2011; Stello et al. 2013, and references therein). In terms of granulation, Bastien et al. (2013, 2016) demonstrated a technique to measure the properties of the surface convective motions of solar-type main-sequence dwarfs, known as 'flicker' (F_8). F_8 is the amplitude of stochastic variations in the light curve on time-scales shorter than 8 h and can be directly tied to the stars' surface granulation properties (Fig. 9).

Comparisons with the predicted granulation properties (i.e. the F_8 amplitude) from 3D stellar models show good agreement in general. However, for stars hotter than ∼6200 K, the models predict amplitudes significantly larger (a factor of ∼2) than what is observed. The smaller observed granulation amplitudes may imply some suppression mechanism (e.g. surface magnetic fields) that reduces the granulation amplitudes relative to expectations (Cranmer et al. 2014). In addition, comparisons of observations and models in order to understand granulation in ensemble of stars have typically not used the full array of information that exists on the power spectrum of the time series where they are observed – a technique that studies of

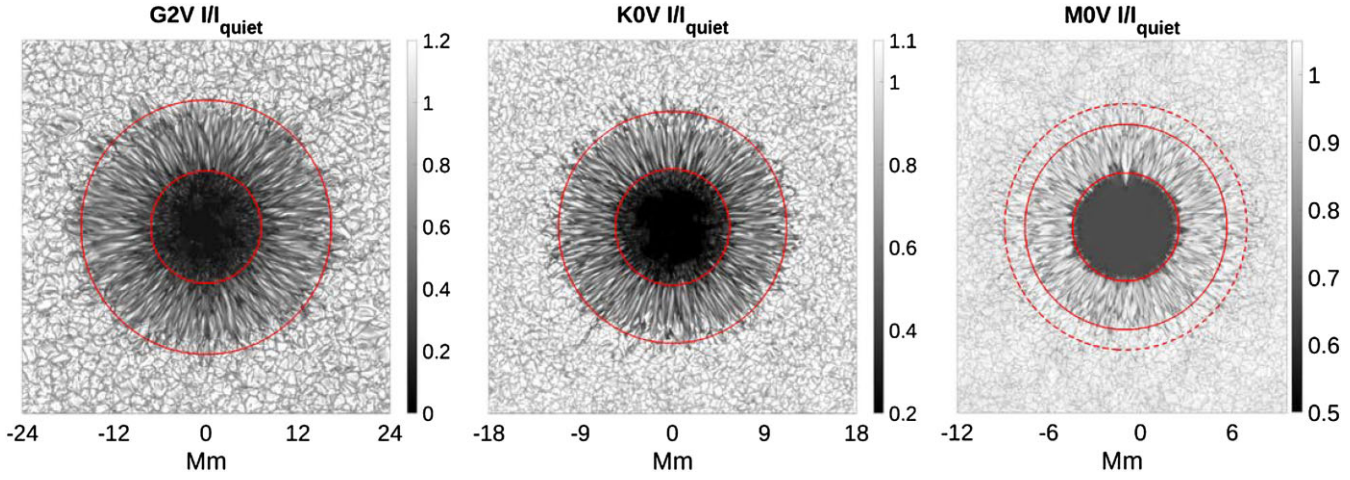

Figure 8 Simulated bolometric intensity maps of complete circular spots for the spectral types G2V, K0V, and M0V. From Panja et al. (in preparation).

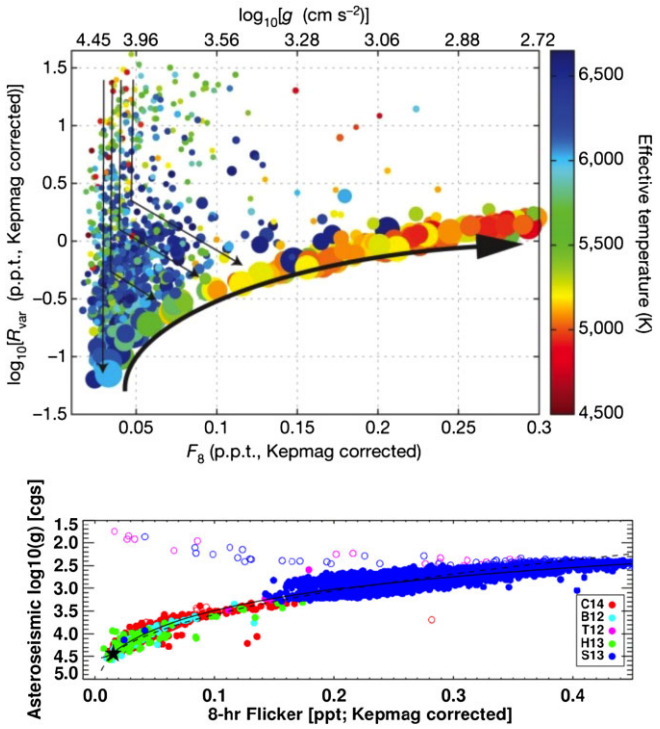

Figure 9 Top panel: Light-curve 'flicker' on time-scales of less than 8 h (F_8; horizontal axis) in units of parts-per-thousand (ppt) is shown for *Kepler* stars as a function of their evolutionary state ($\log g$ scale at top) and as a function of overall photometric variability amplitude (vertical axis). Arrows depict approximate evolution of stars for visualization, beginning as highly magnetically variable dwarf stars (upper left), evolving straight down as they become magnetically quieter at constant $\log g$, then evolving towards the right as they become subgiants and eventually red giants. The thick arrow from the lower left towards the right represents the 'flicker floor' set by granulation alone in the absence of magnetic activity. The photometric signal of surface granulation in solar-type stars ranges from ∼0.02 ppt as main-sequence dwarfs up to $\gtrsim$0.3 ppt as red giants. From Bastien et al. (2013). Bottom panel: Expanded sample from various *Kepler* asteroseismic studies, from Sun-like dwarfs (star symbol at lower left) to red giants at upper right, with their F_8 photometric amplitudes ranging from ∼0.02 to ∼0.45 ppt, respectively. From Bastien et al. (2016).

stellar oscillations do regularly use. Recent work, however, has begun to observationally characterize the full granulation power spectrum via data-driven inference in *TESS* light curves (e.g. Sayeed et al. 2021).

While an evident source of noise to be accounted for when analysing transit light curves, the impact of granulation and oscillations as a contamination source to the transit spectrum has been only explored using simulations. Chiavassa et al. (2017), simulating transits in front of stars using 3D stellar models, suggest that indeed biases on the transit depth can occur due to the fact that exoplanets could transit on chords in the stellar surface that have a significantly different brightness due to the granulation pattern. The effect could be of the order of a few per cent on the transit depth of a terrestrial exoplanet orbiting a Sun-like star in the red-end of the optical (∼0.7 μm), amounting to a few ppm in the case of an Earth–Sun analogue exoplanetary system – within the same order of magnitude as atmospheric features in a transiting Earth–Sun analogue exoplanetary system (Bétrémieux & Kaltenegger 2013). This percentage seems to rapidly decline at longer wavelengths, which suggests could make it a negligible effect in practice for most up-coming space-based observatories focusing on the IR. However, it could become a problem for transit observations in the optical range, such as the ones that missions proposed by, e.g. the Astro2020 Decadal Survey could perform. Validating these granulation simulations with wavelength-dependent data of both the Sun and stars other than the Sun seems to be fundamental to understand the true impact of this effect on future high-precision observations of transiting exoplanetary systems. Although likely having a smaller impact due to the smaller associated amplitudes, performing the same type of simulations and validations for oscillations would be highly beneficial to understand their impact as a contamination source.

2.4.2 *Observing starspots & faculae: techniques and their interplay*

Similar to granulation and oscillations, photometric monitoring of stars other than the Sun has enabled the study of the hours-to-multiyear variations produced by surface inhomogeneities for many decades (Kron 1947). With the advent of stellar high-resolution spectroscopy and spectropolarimetry, these were found to be caused by magnetic regions similar to those on the Sun – starspots (Berdyugina 2005).

Early attempts to interpret the observed photometric variability in other stars involved extrapolating properties from synthetic light curves of model stars with differing spot parameters: circular uniform spots (e.g. Budding 1977); spots with defined umbral and penumbral areas (e.g. Dorren 1987); and active latitudes and/or longitudes (e.g. Bopp & Evans 1973). A single-starspot model is rarely a solution for observed photometric variations. Also, it is unlikely that a light-curve analysis results in a unique solution. Instead, a set of various solutions usually satisfies the same data. Moreover, intrinsic degeneracies exist in the inversion of rotational light curves, and sets of surface features with zero impact are impossible to infer from single-band photometry (Cowan, Fuentes & Haggard 2013; Luger et al. 2021b). Nonetheless, as the volume of photometric data has dramatically increased, more advanced tools have been developed to analyse and interpret these observations (e.g. Lanza et al. 1998; Berdyugina, Pelt & Tuominen 2002; Ribárik, Oláh & Strassmeier 2003; Maxted 2016; Luger, Foreman-Mackey & Hedges 2021a; Luger et al. 2021b).

Understanding solar variability has been very helpful in solving problems posed by stellar observations – in particular, the brightness variations as detected by ground-based efforts and space-based missions such as *CoRoT*, *Kepler*, and *TESS* (e.g. Michel et al. 2008; Southworth 2011; Reinhold, Reiners & Basri 2013; Witzke et al. 2018; Shapiro et al. 2020). For instance, inspired by solar observations, Radick et al. (1998) and Reinhold et al. (2019) demonstrated that active stars are dominated by dark spots, whereas less-active stars are dominated by bright faculae and possibly networks. Reinhold et al. (2019) found the transition from spot- to facula-domination to happen at a Rossby number of about one (i.e. when the rotation period is roughly equal to the convective overturn time). This corresponds to the Vaughan-Preston gap (Vaughan & Preston 1980), where a dearth of F-, G-, and K-type stars with intermediate levels of magnetic activity has been observed (Noyes et al. 1984; Baliunas et al. 1995; Henry et al. 1996; Fossati, Ingrassia & Lanza 2015). They proposed an age of around 800 Myr for this transition, in accordance with the conclusions of Radick et al. (1998). This also explains the apparent lack of stellar rotation periods between 15 and 25 d in the *Kepler* field, which would result from the contributions of dark spots and bright faculae brightness cancelling at these periods (Montet, Tovar & Foreman-Mackey 2017). This result suggests that the observations do not necessarily imply an underrepresentation in the real period distribution but rather the lack of photometric modulation in the light curves. Reinhold et al. (2019) also concluded that stars at ages $\geq$2.55 Gyr should be facula-dominated (see Fig. 10), although further investigations with a larger sample size might be required to robustly extend these results to a wider range of stellar types and properties. While good empirical models based on the Sun exist for solar-like stars, similar models for other spectral types need more investigation and data to support them (Shapiro et al. 2014; Yeo et al. 2020b). For example, See et al. (2021) show a positive correlation between the variability amplitude and metallicity of stars and suggest rotation period detection might be biased towards the periods of metal-rich stars for stars of a given mass (see also Reinhold et al. 2021).

In addition to significant photometric effects, starspots and faculae demonstrate characteristic spectroscopic and spectropolarimetric signatures. Modelling of chromospheric features in the integrated spectra of stars can yield meaningful measurements of plage-like fractional area coverages (see e.g. Andretta et al. 2017); line-depth ratios are also a reliable source for starspot temperatures (e.g. Toner & Gray 1988; Gray & Johanson 1991; Catalano et al. 2002). Furthermore, starspots on stars with higher effective temperatures can result in molecular lines that would not otherwise be present in their spectra (Berdyugina et al. 2003). These molecular features can be

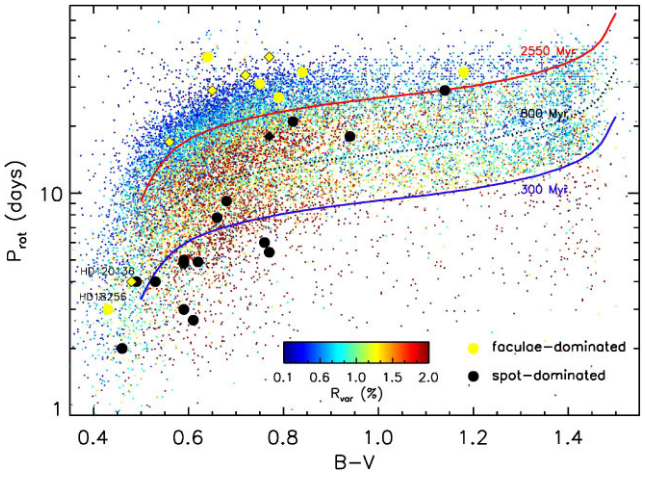

Figure 10 *Kepler* rotation periods $P_{\rm rot}$ against B − V colour. The data points are colour-coded with the variability range $R_{\rm var}$. Black and yellow symbols show spot- and facula-dominated stars, respectively. Dots show dwarf stars (luminosity class V) and diamond show (sub)giants (luminosity class III, IV, and IV–V). The solid blue, dotted black, and solid red lines show 300, 800, and 2550 Myr isochrones, respectively (Reinhold et al. 2019).

used to measure starspot properties (e.g. Vogt 1979; Huenemoerder, Ramsey & Buzasi 1989; Neff, O'Neal & Saar 1995; O'Neal, Saar & Neff 1998; Berdyugina 2002; Afram & Berdyugina 2015). In general, hotter stars have a larger difference between the unspotted surface temperature and the spot temperature than cooler stars do (e.g. Berdyugina 2005; Andersen & Korhonen 2015). This temperature difference can be as large as 2000 K for spectral type G0 and only 200 K for spectral type M4. While the trend with spectral type is similar, temperature differences derived from spectral observations can be both smaller and larger than those derived from observations (Panja et al. 2020). Spectropolarimetric analysis of many atomic and molecular lines reveals an internal, height-dependent temperature and magnetic structure of starspots with strong magnetic fields, which were found to be smaller and warmer in the lower atmospheres of earlier M-dwarfs than later M-dwarfs, where starspots with strong fields are bigger and cooler throughout their entire atmosphere (Berdyugina 2011; Afram & Berdyugina 2019).

The distribution of starspots on stellar surfaces can be recovered in some cases using the Doppler imaging (DI) technique, as surface features induce perturbations in Doppler-broadened spectral line profiles (e.g. Deutsch 1958; Vogt & Penrod 1983; Piskunov, Tuominen & Vilhu 1990; Berdyugina 1998). This method is reliant on stars being rapid rotators and starspots being relatively large. Such large active regions have been detected on young, rapidly rotating solar-type stars (e.g. Jeffers et al. 2007; Järvinen et al. 2008, 2018) as well as on evolved, rotationally synchronized binary components, such as RS CVn-type stars (e.g. Berdyugina et al. 1998; Berdyugina, Ilyin & Tuominen 1999; Vogt et al. 1999; Strassmeier 2009). Time series of DI maps and photometric light curves reveal stellar differential rotation and latitudinal activity belts (e.g. Donati & Collier Cameron 1997; Berdyugina & Henry 2007; Vida et al. 2007), longitudinal migration of active regions with respect to the stellar rotation and various activity cycles (e.g. Berdyugina & Tuominen 1998; Järvinen, Berdyugina & Strassmeier 2005a; Järvinen et al. 2005b; Oláh et al. 2009), and meridional motions and poleward migration of active regions (Kovári et al. 2007). Such long-term starspot phenomena are important for monitoring transits of Earth-like planets around solar-type stars with orbital periods more than a 100 d or so. High

spectral resolution is key for resolving spots and their substructure, e.g. a possible penumbra signature on a young solar analogue EK Dra (Järvinen et al. 2018).

DI also shows that, for active stars, starspots can occur at much higher latitudes than within the $\pm 30^{\circ}$ from the equator that is typically seen on the Sun. Large spots have been found to cover even the visible pole of the star (e.g. Strassmeier & Rice 1998; Donati 1999; Korhonen et al. 2021). Recently, large starspots on giant stars were directly imaged using long-baseline interferometric imaging (Roettenbacher et al. 2016, 2017). This method confirmed the existence of polar starspots on active stars (Roettenbacher et al. 2016). It also allows obtaining accurate information on spot locations with respect to the stellar equator that is not possible with DI (Roettenbacher et al. 2017). A polar spot that is perfectly symmetrical around the pole does not cause rotational modulation in the light curve. On the other hand, it would still cause effects on the observed spectrum of the star and also lead to the wrong estimation of the transit depth (e.g. Rackham et al. 2018; Zhang et al. 2018). However, typically stars showing polar spots would also show large spots on other latitudes, causing significant variation in their light curves. Therefore, as with other active stars, the presence of polar spots must be taken into account when assessing targets for transit spectroscopy and analysing observations from these systems. Here, molecular spectroscopy can also help detecting such spots, even if they do not modulate photometric and spectroscopic signals.

Similar to DI, a Zeeman–Doppler imaging (ZDI) technique based on spectropolametric measurements can help to recover the distribution of magnetic fields on stellar surfaces (Semel 1989; Donati et al. 1997; Donati & Landstreet 2009; Shulyak et al. 2019; Fuhrmeister et al. 2022). However, surface features detected photometrically and in DI maps seem not directly related to features in ZDI maps. Overcoming this discrepancy and improving underlying physical assumptions (e.g. Berdyugina 2009) may allow in the future relate ZDI magnetic features with transit spectrophotometry.

In terms of activity level and its relation with age, a clear relation has been found between the two for G, K, and M stars. Stars are born as rapid rotators, and their rotation slows down with age due to magnetic braking (Skumanich 1972). On the other hand, the dynamo action is enhanced with more rapid rotation until a saturation level (Pallavicini et al. 1981). Somewhat surprisingly, both fully convective and partially convective stars follow similar activity–rotation relations (Kiraga & Stepien 2007; Newton et al. 2017; Wright et al. 2018). There is evidence for the age–rotation relations breaking down at the halfway point of the main sequence lifetime of the star, i.e. close to the current age of the Sun, suggested to be due weakened magnetic braking (e.g. van Saders et al. 2016; Nichols-Fleming & Blackman 2020; Hall et al. 2021). Additionally, gyrochronological age estimates are significantly lower than isochronal age estimates for planet-hosting stars, which may be due to tidal or magnetic interactions between the star and planet (Brown 2014; Maxted, Serenelli & Southworth 2015).

The study of stars other than the Sun has also been fundamental to understand the time-scales on which active regions live on stellar surfaces. From the Sun, we know that the lifetime of small sunspots is proportional to their size (Gnevyshev 1938; Waldmeier 1955). Similar behaviour for starspots has been indicated from relatively sparse photometric observations (e.g. Hall & Henry 1994). Precise, high-cadence space photometry from *Kepler* and *TESS* has recently been used to further investigate starspot lifetimes as well (Giles, Collier Cameron & Haywood 2017; Namekata et al. 2020), which can be compared with theoretical and empirical models (Bradshaw & Hartigan 2014; Namekata et al. 2019). This is also an active area of research in the radial-velocity community, which is also interested in constraining these time-scales (see e.g. Haywood et al. 2014; Rajpaul et al. 2015; Faria et al. 2016). It seems that for other stars, starspot lifetimes fall slightly below the solar trend, but are within an order of magnitude of those expected from sunspots studies. Very large starspots on active stars can live a very long time, maybe even years (Hussain 2002). On the other hand, it is not clear if these huge spots are really single spots or an active-region-like collection of individual spots. On rapidly rotating M dwarfs, starspot modulation, observed in photometry and spectral features, can remain coherent for months to years, suggesting long-lived features (Newton et al. 2016; Robertson et al. 2020). The rapidly rotating ($P_{\rm rot} = 0.44$ d), fully convective, single M4 dwarf V374 Peg, e.g. exhibits a large-scale magnetic topology that is consistent for years (Morin et al. 2008) and even decades (Vida et al. 2016). Rather than originating from shearing in the tachocline region as is thought to be the case for stars with convective outer envelopes (Parker 1955), it has been proposed for fully convective stars that a distributed dynamo generates the surface magnetic field, which interacts with turbulent convection in the outer layers to produce the observed small-scale fields (Yadav et al. 2015).

2.4.3 *Atmospheric heterogeneity in ultracool dwarfs*

Stellar heterogeneity imposes special challenges for transiting planets orbiting ultracool dwarfs – stars and brown dwarfs with $T_{\rm eff} < 3000$ K. With the planet-to-star radius ratio being a key parameter underpinning the feasibility of observational studies of transiting exoplanets, ultracool dwarfs – including the smallest dwarf stars and most massive brown dwarfs – are set to play key roles in the future of exoplanet science. These stars, however, are not just smaller versions of the Sun but, instead, are a fundamentally different class of objects.

A spectral-type and thus temperature-dependent pattern of rotational variability has been observed for the mainly temperature-driven sequence from late M-dwarfs through early L-dwarfs to T-type brown dwarfs. Time-resolved, multicolour or spectrally resolved observations of such rotational variability provide powerful probes of the nature of the atmospheric heterogeneity in these objects. For the coolest stars and hottest brown dwarfs (at the M/L spectral-type transition), it is very likely that rotational variability is caused by multipole magnetic fields, resulting in large starspots. Such spots, possibly anchored by large-scale magnetic fields, have been found (at least for some early L-type dwarfs) to lead to periodic variability that is stable over multiple years (e.g. Gizis et al. 2015). Indeed, a strong surface magnetic field of 5 kG was successfully detected on one of such young brown dwarfs displaying transient rotationally modulated radio bursts (Berdyugina et al. 2017; Kuzmychov, Berdyugina & Harrington 2017). Also, the rotational modulation of the Balmer H I, blue Ca II, and Na I D line emission as well as radio bursts were found to be related to the detected magnetic region and magnetic loops anchored in it. Since rotation periods of such objects (and thus the emission modulation) are 2–3 h, this variability may affect transit spectra of exoplanets.

In contrast, later spectral type brown dwarfs (from mid-L to mid-T types) often display rotational variability (e.g. Buenzli et al. 2014; Radigan et al. 2014; Metchev et al. 2015) that are different in nature: Their light-curve shapes are constantly evolving (e.g. Artigau et al. 2009; Biller et al. 2013; Apai et al. 2017), likely caused by cloud thickness variations (e.g. Radigan et al. 2012; Apai et al. 2013) (although chemical disequilibrium may also play a role, Tremblin et al. 2020). Due to the low atmospheric temperatures and ionization

rates, the cloud thickness modulations are very likely independent of the magnetic field strengths (Miles-Páez et al. 2017). Instead, cloud thickness variations are driven by atmospheric circulation and lead to atmospheric jets and zonal circulation (Zhang & Showman 2014; Apai et al. 2017; Millar-Blanchaer et al. 2020; Apai, Nardiello & Bedin 2021; Tan & Showman 2021).

2.4.4 *Limb darkening and its interplay with stellar heterogeneities*

As has been discussed in this section, understanding CLVs on stars (limb-darkening or -brightening profiles) is fundamental to constraining stellar heterogeneities. They are not only critical for constraining the amplitude and contrast of granulation in stars and the observed contrast variations of faculae and spots as a function of their position on stellar surfaces, but they also impact transit light-curve modelling itself and hence the transit spectrum that is derived from this modelling. Through simulations, it has been shown that inaccurate modelling of limb darkening may lead to a 1- to 10-per cent discrepancy in the determination of exoplanetary radii obtained from transit photometry observed at UV or visible wavelengths (see e.g. Espinoza & Jordán 2015; Csizmadia et al. 2013). Studies trying to constrain how well theoretical limb-darkening profiles extracted from stellar model atmospheres compare against empirically determined limb-darkening profiles from precise photometry have typically found disagreement between the two (Claret 2009; Cabrera et al. 2010; Espinoza & Jordán 2015; Maxted 2018).

Limb darkening has an important interplay with stellar heterogeneities too. Csizmadia et al. (2013) showed that if stellar heterogeneities are present in the star, this can effectively modify the limb-darkening profile. Using theoretical limb-darkening laws to model this effect, which do not account for the presence of those features, will create a bias on the model that would translate to a bias in the retrieved transit depth. This could itself be an important source of contamination on the transit modelling.

Taking into account polarization due to scattering in stellar atmospheres was also found important for theoretical limb-darkening models. This is especially true closer to the limb and for cooler atmospheres, where scattering becomes significant as compared with absorption (Kostogryz & Berdyugina 2015; Kostogryz et al. 2016, 2017). Hence, near-limb transits of cooler stars will be most sensitive to (and, thus, biased if not accounted for) polarization effects.

2.4.5 *Our finding: Finding 1.3*

From this analysis, we draw the following findings:

Summary

Simultaneous multiwavelength (multi-instrument) stellar observations are needed to provide feedback to modelling efforts and improve our understanding of the photospheres and chromospheres of other stars, including high-priority exoplanet host stars. This is particularly critical for K, M, and L dwarfs, for which models are relatively poorly constrained.

Capability needed

Time-resolved multiband photometry, spectroscopy, and spectropolarimetry of high-priority exoplanet host stars are needed to provide feedback for simulations of these stars. In particular, we need to understand the variability of exoplanet hosts within the wavelength range of interest for current and upcoming missions (0.3–5 μm) at time-scales relevant to granulation (minutes), transits (minutes to hours), rotation periods (days to months), and magnetic cycles (years). More work is needed to understand the precisions at which variabilities should be constrained to be useful in this respect and the dependence of the required precision on the stellar parameters and the transit science case. Limb darkening as a function of wavelength and stellar activity should be constrained with future observations in order to better understand its impact as a contamination source on the transit spectrum.

Capability today

Precise broad-band photometric light curves from *CoRoT*, *Kepler*/*K2*, and *TESS* probe surface convective motions (or 'flicker'; Michel et al. 2008; Bastien et al. 2013, 2016) and spot distribution and evolution (Southworth 2011; Reinhold et al. 2013; Morris et al. 2017), providing feedback for 3D models of stellar surface features. Multidecade monitoring of stellar chromospheric emission (Reinhold et al. 2019) as well as recent population studies relying on photometric light curves (Montet et al. 2017) have been used to infer that more-active stars are dominated by dark spots while less-active stars are dominated by bright faculae. Ground-based spectroscopy and spectropolarimetry provide constraints on physical properties of stellar magnetic features (e.g. Toner & Gray 1988; Gray & Johanson 1991; Neff et al. 1995; Catalano et al. 2002; Berdyugina 2011; Andretta et al. 2017; Afram & Berdyugina 2019). ZDI can probe structures in photospheres of rapidly rotating stars (e.g. Semel 1989; Donati et al. 1997; Berdyugina & Tuominen 1998; Berdyugina & Henry 2007; Jeffers et al. 2007; Shulyak et al. 2019; Fuhrmeister et al. 2022), but it is unclear how well these findings may extend to the general population of exoplanet host stars, which tend to rotate more slowly (e.g. Gaidos et al. 2023).

Mitigation in progress

Recent work has explored the limits of light-curve inversion (Luger et al. 2021b) and presented an interpretable Gaussian process model that can be used to infer physical parameters from light curves (Luger et al. 2021a). Meanwhile, other work has shown that combining high-resolution spectroscopy and spectropolarimetry, precise space photometry, and interferometric imaging helps to construct stellar surface maps of cool stars (Roettenbacher et al. 2016, 2017), more recently also including a main-sequence exoplanet host (Roettenbacher et al. 2022).

3 OCCULTED ACTIVE REGIONS

Essential questions include the following:

(i) What is the state of the art for modelling and observing occulted active regions?
(ii) What are the outstanding theoretical challenges for this work?
(iii) What are the available modelling tools for active-region occultations? Are they sufficient for the precise transit data sets that are expected in the next decade?

3.1 Introduction

As described in Section 1, stellar surfaces are very inhomogeneous. In particular, active regions, including dark (spots and pores) and bright (faculae, plage, and network) magnetic features, are of concern to transmission spectroscopy due to their effects on transmission spectra. If the transit chord of a planet crosses a spot (facula), this will appear as a temporal brightening (darkening) in the resulting light curve. The prime effect of unocculted active regions, which are discussed in Section 4, is a change in apparent transit depth. Here, we focus on the effects of occulted active regions on the observed transit light curves. We consider three topics in this context: the state of the art for observations and models of occulted active

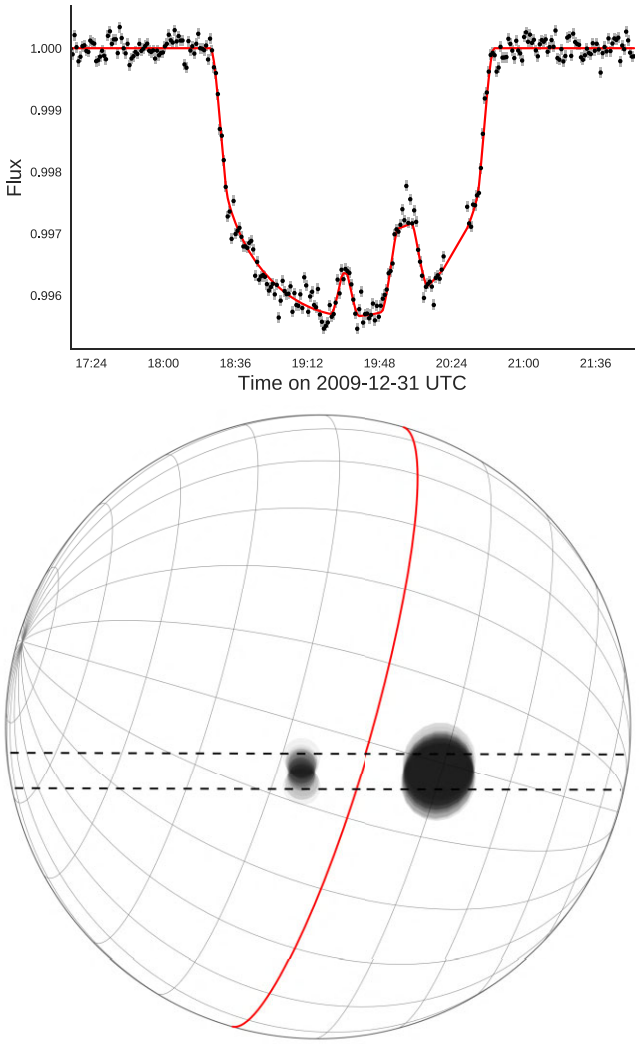

Figure 11 Top panel: Transit light curve of HAT-P-11 b observed by the *Kepler* mission (black) fit with the STSP forward model (red), which models occultations by two starspots (Morris et al. 2017). Bottom panel: Inferred starspot map produced by the Markov chain Monte Carlo (MCMC) fit of the STSP model to the *Kepler* observations, shown with the stellar rotational pole to the right and into the page. The stellar equator is marked in red and the transit chord is given by the dotted black horizontal lines. The two clusters of overlapping, low-opacity spots represent draws from the posterior distributions for the spot positions and radii.

regions (Section 3.2), outstanding theoretical challenges in this context (Section 3.3), and the availability of well-maintained tools for conducting these analyses (Section 3.4). In the following sections, we summarize the analysis that leads to our primary findings in these areas.

3.2 State of the art for observations and models

3.2.1 Observations of spot occultations

Due to spots' high contrast with respect to the quiet stellar surface and their more distinct structure as compared with faculae, spot occultations are significantly easier to identify, manifesting as temporal bumps in the transit light curves (see top panel of Fig. 11 for an example). Having lower contrast, faculae are much patchier in their surface structure and thus are more difficult to separate from noise and stellar variability. The following paragraphs summarize some notable studies of spot crossings from space- and ground-based observations.

Space-based

The first known transiting exoplanet, HD 209458b (Charbonneau et al. 2000; Henry et al. 2000), also provided the first observation of a exoplanet occulting a starspot, both from space with *HST* (Brown et al. 2001) and from the ground (Deeg, Garrido & Claret 2001). The occulted spots on HD 209458 were first modelled by Silva (2003), yielding their sizes and temperatures. The next detection was with the *CoRoT* telescope of CoRoT-2 (Silva-Valio et al. 2010). The number of observed starspot occultation events has increased since *Kepler* and the extended *K2* mission [e.g. Kepler-30 (Sanchis-Ojeda et al. 2012; Netto & Valio 2020), Kepler-63 (Sanchis-Ojeda et al. 2013), Kepler-539 (Mancini et al. 2016), Kepler-17 (Désert et al. 2011a; Valio et al. 2017), HAT-P-11 (Sanchis-Ojeda & Winn 2011; Oshagh et al. 2013a; Morris et al. 2017; Murgas et al. 2019), Kepler-71 (Zaleski et al. 2019), Kepler-45 (Zaleski et al. 2020), and Kepler-411 (Araújo & Valio 2021)]; although with low-cadence temporal sampling (30-min cadence), the *Kepler* mission is neither ideal nor well suited to such detections. The cadence has a strong impact on the detection limits of starspot anomalies for planetary systems with small planet-to-star radius ratios (Tregloan-Reed & Unda-Sanzana 2019). This effect is mostly evident in the detection limits of the smallest and/or hottest (low contrast, $\rho > 0.9$, where ρ is the intensity of the spot relative to the photosphere) dark starspots, when the time-scale of the occultation event is equivalent to or shorter than the observational cadence. Starspot occultations are more easily detected with the 1-min-cadence *K2* observations. Such detection examples include the aligned WASP-85 (Močnik et al. 2016) and Qatar-2 (Močnik, Southworth & Hellier 2017b) systems with recurring occultation events, and the misaligned WASP-107 system, where the occultations were not found to be recurring (Dai & Winn 2017; Močnik et al. 2017a).

Ground-based

There is a substantially greater number of observed starspot occultation events in transit light curves from ground-based telescopes compared with those from space-based telescopes. This is principally due to the many observations using high-cadence (<2 min) observations, which allows for smaller starspots to be detected. A sample of systems with starspot detections from ground-based photometry is given in Table 3.

3.2.2 Influences on the retrieved transmission spectra

When occulted during planetary transits, starspots and faculae decrease and increase the apparent transit depth, respectively, (e.g. Czesla et al. 2009), especially in the visible (Fig. 12). As their effect is wavelength-dependent, uncorrected active-region crossings produce effects opposing those of unocculted active regions. In broad-band data, occultations of stellar active regions (spots/faculae) during planetary transits can mimic broad-band characteristics of planetary atmospheres in transmission spectra, as has been shown with both observations and simulations (Sing 2010; Pont, Aigrain & Zucker 2011; Oshagh et al. 2014; Herrero et al. 2016). In the context of narrow-band features, several studies have explored the possibility that realistic stellar active regions (both occulted and unocculted) on various types of stellar hosts could also have a significant impact on the strength of atomic and molecular features (Rackham et al. 2017, 2018, 2019; Apai et al. 2018; Tinetti et al. 2018; Chachan et al. 2019).

Table 3. Selected planetary systems found to show a starspot-occultation event in their light curves from ground-based photometry.

Planetary system	Telescope/instrument	Reference
HD 209458	Observatorio de Sierra Nevada 90 cm/Strömgren photometer	Deeg et al. (2001)
WASP-4	1.54-m *Danish Telescope*/DFOSC	Southworth et al. (2009)
	Magellan Baade 6.5 m/MagIC	Sanchis-Ojeda et al. (2011)
HAT-P-11	Astrophysical Research Consortium 3.5 m/ARCTIC	Morris, Hawley & Hebb (2018e)
WASP-19	1.54-m *Danish Telescope*/DFOSC	Mancini et al. (2013)
	MPG/ESO 2.2 m/GROND	Mancini et al. (2013)
	3.6-m *New Technology Telescope*/EFOSC2	Tregloan-Reed et al. (2013)
	8.2-m *VLT*/FORS2	Sedaghati et al. (2015)
	Magellan Baade 6.5 m/IMACS	Espinoza et al. (2019)
HATS-2	*MPG*/ESO 2.2 m/GROND	Mohler-Fischer et al. (2013)
WASP-21	*Cassini* 1.52 m/BFOSC	Ciceri et al. (2013)
	Calar Alto 1.23 m/DLR-MKIII	Ciceri et al. (2013)
Qatar-2	*MPG*/ESO 2.2 m/GROND	Mancini et al. (2014b)
	CAHA 2.2 m/BUSCA	Mancini et al. (2014b)
	Cassini 1.52 m/BFOSC	Mancini et al. (2014b)
	Calar Alto 1.23 m/DLR-MKIII	Mancini et al. (2014b)
WASP-89	*TRAPPIST* 0.6 m/TRAPPIST photometer	Hellier et al. (2015)
	Euler 1.2 m/EulerCAM	Hellier et al. (2015)
WASP-6	1.54-m *Danish Telescope*/DFOSC	Tregloan-Reed et al. (2015)
HAT-P-36	*Cassini* 1.52 m/BFOSC	Mancini et al. (2015)
	Calar Alto 1.23-m/DLR-MKIII	Mancini et al. (2015)
WASP-41	1.54-m *Danish Telescope*/DFOSC	Southworth et al. (2016)
	TRAPPIST 0.6 m/TRAPPIST photometer	Neveu-VanMalle et al. (2016)
	1.54-m *Danish Telescope*/DFOSC	Neveu-VanMalle et al. (2016)
WASP-52	*William Herschel Telescope* 4.2 m/ULTRACAM	Kirk et al. (2016)
	MPG/ESO 2.2 m/GROND	Mancini et al. (2017)
	1.54-m *Danish Telescope*/DFOSC	Mancini et al. (2017)
	Cassini 1.52 m/BFOSC	Mancini et al. (2017)
	Calar Alto 1.23 m/DLR-MKIII	Mancini et al. (2017)
	Euler 1.2 m/EulerCAM	Mancini et al. (2017)
HAT-P-20	*YO* 1 m/Andor 2K × 2K CCD camera	Sun et al. (2017)
GJ 3470	10.4-m *Gran Telescopio Canarias*/OSIRIS	Chen et al. (2017)
GJ 1214	8.4-m *Large Binocular Telescope*/Large binocular camera	Nascimbeni et al. (2015)

If the occultation is isolated and its signal large compared with the noise level, it is usually removed from the transit. However, Barros et al. (2013) showed that the occulted feature can impact multiple transit parameters other than the transit depth, such as mid-transit time, scaled orbital semimajor axis, and orbital inclination. In particular, impact parameter variations due to the effect of active regions on limb-darkening parameters can introduce positive or negative slopes from the visible to the IR transmission spectrum (Alexoudi et al. 2020). Such effects can reach up to one or more scale heights.

Hence, simply removing active-region occultations from the transit profile likely does not completely negate their effect on the determination of transit parameters, particularly with high-precision spectrophotometry. The problem becomes trickier still when multiple occultations are observed in the same transit, as has been found in many cases in the visible (e.g. Czesla et al. 2009; Désert et al. 2011a; Morris et al. 2017). In these cases, removing the occultations might simply not leave enough data points for the fit of the transit profile, such that using a transit-starspot model becomes a necessity. In addition, modelling active-region occultations, instead of removing them, allows us to leverage their wavelength-dependent impact on planetary transits to derive active-region parameters (Sing et al. 2011; Bruno et al. 2022) – valuable information for correcting transmission spectra for the effects of stellar activity (see Section 5). Finally, even in cases without obvious active-region occultations, occultation models can be used to place upper limits on the impact of low signal-to-noise occulted active regions, which introduce an uncertainty in the level of stellar-activity contamination similar to that of unocculted active regions but with an opposite sign (Ballerini et al. 2012).

3.2.3 Our finding: Finding 2.1

From this analysis, we draw the following findings:

Summary

Precise transit observations increasingly reveal occultations of stellar active regions. Rather than flagging and removing active-region occultations, which results in decreased observing efficiency and possibly biased transit depth measurements, future observations should move towards joint inference of the active-region and planetary properties.

Capability needed

Detections of occulted active regions are more common in precise data sets. From a practical perspective, discarding data impacted by active-region occultations in many interesting systems will result in continuously lower observing efficiencies as precisions improve. Additionally, more study is needed to understand the extent to which transit depths may be biased by active regions that are occulted but undetected.

Capability today

Many recent studies have included joint inferences of transit and active-region properties using a variety of spot modelling codes (see e.g. Table 3). However, the active regions we can detect in precise

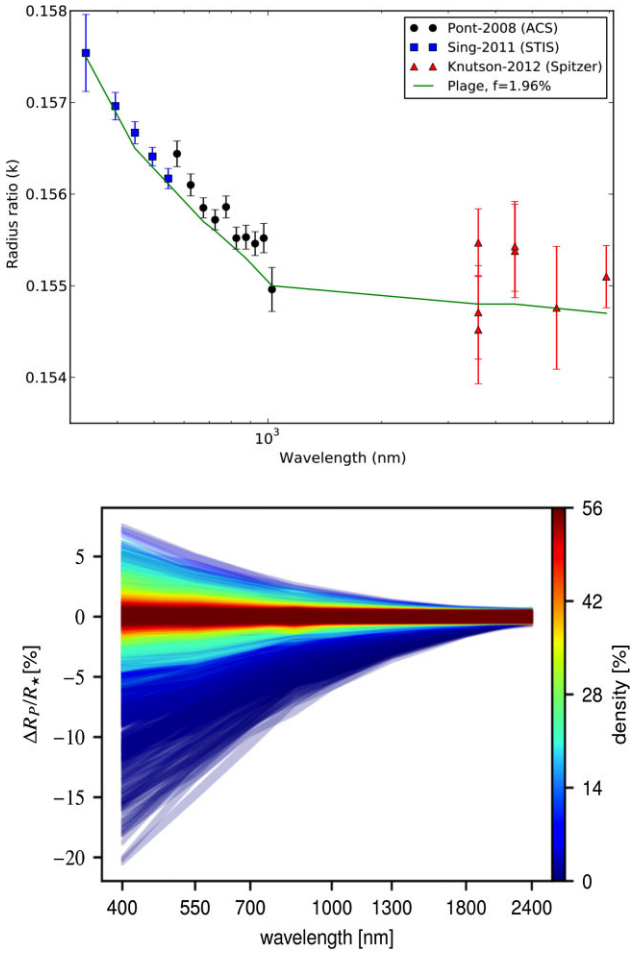

Figure 12 Top panel: Impact of stellar facula occultation on the retrieved transmission spectra of HD 189733b, which is similar to what one would expect from a hazy atmosphere in a planet that causes a Rayleigh scattering slope (Oshagh et al. 2014). Bottom panel: Simulated transit depth changes for WASP-19b in chromatic Rossiter–McLaughlin observations due to occultations of randomly distributed active regions (Boldt et al. 2020). Results from 10 000 simulations are shown, highlighting a wide range of broad-band features produced. The colour scale indicates the percentage of other simulated results that fall within $\Delta R_p/R_s \leq 0.0005$ of the current result across the studied wavelength range, highlighting that most random distributions of active regions do not produce strong changes that mimic broad-band features.

transit light curves, both ground- and space-based, are much larger than those that have been observed on the Sun (Mandal et al. 2021). At the same time, data impacted by active-region occultations are commonly discarded in other studies.

Mitigation in progress

Joint analyses of active-region and planetary properties from impacted light curves have been presented recently (e.g. Mancini et al. 2017; Espinoza et al. 2019). Additionally, some groups are beginning to look into the impact of heavily spotted transit chords on inferences (e.g. Cauley et al. 2018; Morris et al. 2018b).

3.3 Theoretical challenges for active-region occultations

3.3.1 Solar spots and comparison to models of stellar spots

In the context of studying transiting planets occulting starspots, the most relevant property is the relative brightness of the starspot with respect to its surroundings. For spots on the Sun, there is a clear connection between the size of the spot and its umbral intensity: Larger spots tend to have darker umbrae than smaller spots (Mathew et al. 2007; Schad 2014; Valio et al. 2020). In the study by Mathew et al. (2007), spots that have an umbral radius between 5 and 15 arcsec (1 arcsec $\approx$ 720 km), the mean umbral relative intensity drops from 0.5 to 0.3 relative to the quiet-Sun intensity at the continuum near the Ni I line at 676.8 nm. They also found a very weak dependence of penumbral intensity on spot size, between 0.84 and 0.81 at the same wavelength.

Another property determining the effective brightness of a spot on a star is the ratio of penumbral to umbral area. For the Sun, this factor is roughly 4 and generally independent of spot area above a minimal spot area (although there is some scatter in the literature; e.g. Solanki 2003).

For starspots, there is a strong connection between the surface temperature of the star and the spot contrast (Berdyugina 2005). The spot temperature contrast is larger for hotter stars, and this seems to be valid for stars of different surface gravities. Updated summaries of starspot contrasts as a function of stellar surface temperature can be found in Mancini et al. (2014a) and Herbst et al. (2021). Interestingly, starspot temperatures inferred from planetary transits seem to be warmer than temperatures retrieved by other methods. This may be because the transit method returns the average temperature of the entire spot while methods like modelling of molecular bands are mainly sensitive to the umbral temperatures (due to the non-linear response of molecular lines to temperature).

A particularly useful example for drawing comparisons to solar activity is that of the active G-dwarf Kepler-71. Both spots and plages have been detected in its photosphere via occultations by its transiting hot Jupiter (Zaleski et al. 2019). Despite the higher contrast of Kepler-71 faculae than the solar counterparts, these plages showed similar properties, such as increasing contrast towards the limb and larger sizes than sunspots. Assuming a solar-type differential-rotation profile, the results obtained from independent modelling of starspots and faculae indicated similar rotational periods at the transit latitude and the same rotational shear.

3.3.2 The importance of MHD simulations for modelling occulted active regions

Johnson et al. (2021) have used quiet-Sun limb darkening and limb-dependent facular contrasts derived from MURaM 3D MHD simulations by Beeck et al. (2015a), together with spot contrasts computed from 1D model atmospheres with effective temperatures in agreement with 3D MHD results by Panja et al. (2020), to model rotational light curves of active G2, K0, M0, and M2 stars in the *Kepler* band. They found that the spot temperature together with spot coverage determines the amplitude of the variability, while faculae have a strong influence on mean brightness levels and the shape of light curves. The latter might have significant implications for occultation modelling.

Using 3D radiative MHD simulations, Panja et al. (2020) have recently confirmed the dependence of spot contrast on stellar surface temperature for dwarfs within the spectral range G2V–M0V. These authors simulated the spectral types G2V, K0V, and M0V and obtained umbral bolometric intensities of 0.3, 0.5, and 0.7 relative to the stellar photospheric intensities. Ongoing work includes simulations of spots with expansive penumbral filaments, similar to those observed in sunspots for the simulated G2V starspot, and

simulations that allow the calculation of spot contrasts as a function of wavelength and disc position (Panja et al., in preparation).

3.3.3 Common degeneracies in the retrieved spot and facula properties

The main difficulty in accounting for surface inhomogeneities is that these are essentially never single, isolated features. Thus, dark and bright features are likely present simultaneously, both occulted and unocculted. Simultaneous ground-based spectroscopic and space-based photometric observations of G and K stars show that starspots and plage are often, although not always, spatially associated, as is true on the Sun (Morris et al. 2018d). Moreover, it is not always clear whether a bright or dark feature is being occulted, as models with either type of feature at different times may offer comparable fits to transit light curves (Bruno et al. 2016; Kirk et al. 2016). The resulting effect from all features depends on their coverage (size), location, and the wavelength of observations, and is generally impossible to separate.

When observing stellar rotation in a single photometric bandpass, both faculae and starspots can produce rotational modulation signatures. Observing in more than one bandpass nearly simultaneously can break this degeneracy and suggest whether spots or faculae dominate. This technique has been applied to photometry of the planet-hosting M8 dwarf TRAPPIST-1, which shows (i) no clear spot occultations in transit photometry, though a few candidate events have been identified (Burdanov et al. 2019; Ducrot et al. 2020), (ii) strong rotational modulation in the *Kepler* bandpass (Luger et al. 2017; Vida et al. 2017), and (iii) very little modulation in *Spitzer* photometry (Roettenbacher & Kane 2017; Morris et al. 2018a, c).

3.3.4 Our finding: Finding 2.2

From this analysis, we draw the following findings:

Summary

Theoretical advances are needed to understand the limits of what we can infer about active-region properties from transit light curves and how best to incorporate prior knowledge from MHD models into transit studies.

Capability needed

More study is needed to understand the limits of inferences from occultations and how to break degeneracies in retrieved parameters of occulted active regions, such as size and contrast, with additional observations, such as spectroscopic transit depths or multiwavelength monitoring. Additionally, more study is needed to understand best approaches for propagating information from stellar magnetic activity models into priors on spot properties, such as typical size and contrast, as a function of stellar spectral type and activity level.

Capability today

Studies generally use uninformative priors on active-region properties when studying occultations of active regions (e.g. Morris et al. 2017). Retrieved sizes are generally large and contrasts are generally small relative to those inferred from other methods (e.g. Mancini et al. 2013; Espinoza et al. 2019), which may point to biases with the technique or the combined impact of umbral, penumbral, and facular areas.

Mitigation in progress

Multiple groups are developing MHD models for active regions on stars with differing spectral types and activity levels (Panja et al. 2020; Johnson et al. 2021; Witzke et al. 2022), which can be used to provide informative priors in future studies.

3.4 The availability of well-maintained, open-source tools

Over the years, there have been multiple starspot occultation models developed both by the eclipsing binary star community [e.g. WILSON-DEVINNEYcode (Wilson & Devinney 1971; Wilson 1979, 1990, 2012) and PHysics Of Eclipsing BinariEs (PHEOBE; Prša & Zwitter 2005; Prša et al. 2016) and the exoplanet community [e.g. ECLIPSE (Silva 2003), SOAP-T (Oshagh et al. 2013a), PRISM (Tregloan-Reed et al. 2013, 2015, 2018), SPOTROD (Béky, Kipping & Holman 2014), KSint (Montalto et al. 2014), ellc (Maxted 2016), StarSim (Herrero et al. 2016), PyTranSpot (Juvan et al. 2018), STSP (Morris et al. 2017), and TOSC (Scandariato et al. 2017)]. Such models require integration over a 2D grid on the stellar surface or in the projection plane, which is computationally expensive, with computational time growing as the square of the grid resolution. The only exceptions to our knowledge are the semi-analytical SPOTROD and STSP models. At the same time, full 2D integration (pixelation) has the advantage that it allows individual intensities (accounting for surface inhomogeneities) to be assigned to every individual element at specific coordinates.

We summarize some of the most prominent models below.

3.4.1 ECLIPSE

ECLIPSE (Silva 2003), a code first written in IDL and then translated into PYTHON, models active-region occultations using a 2D image of a synthetic star with spots (dark features) or plages (bright features) on the surface of the limb-darkened stellar disc. The planet, modelled as a circular dark disc, is positioned in its elliptical orbit every 2 min (or the desired time interval) and the intensity of all pixels in the image is summed to yield the light-curve intensity at a given time. The spots (or plages) are simulated as dark (or bright) circles positioned along the transit chord. Spot intensities vary from 0 to 1, whereas the plage intensities vary from 1 to 1.5, where 1 is the brightness of the activity-free stellar disc centre. The temperature of the spots can be estimated assuming blackbody emission for both the spots/plages and the stellar photosphere (Valio et al. 2017). Foreshortening of the spots is taken into account when they are close to the stellar limb. This model was first applied to HD 209458 (Silva 2003) and has since been applied to many targets with high-cadence *Kepler* data (e.g. Silva-Valio et al. 2010; Valio et al. 2017; Netto & Valio 2020; Zaleski et al. 2020; Araújo & Valio 2021). An example of such modelling is shown in Fig. 13 for Kepler-17 with three spots. ECLIPSE can be found at GitHub[4] and was last updated in 2021.

3.4.2 SOAP-T

Spot Oscillation and Planet Transit (SOAP-T; Oshagh et al. 2013a) is a SOAP (Boisse, Bonfils & Santos 2012) adaptation that can generate light curves and radial-velocity variations for systems containing a rotating spotted star and a transiting planet. The stellar disc, active regions on it, and a transiting exoplanet are simulated numerically using a pixelation approach. This tool has been used to investigate spot-crossing anomalies within transit light curves (Oshagh et al. 2013b), as well as to assess their impacts on the estimation of the transit duration, depth, and timing. SOAP-T was used to study, for the first time, the impact of the occultation of a stellar spot and plage on the transmission spectra of transiting exoplanets (Oshagh et al. 2014). SOAP-T was also used to study the impact of stellar

[4]https://github.com/biaduque/astronomy

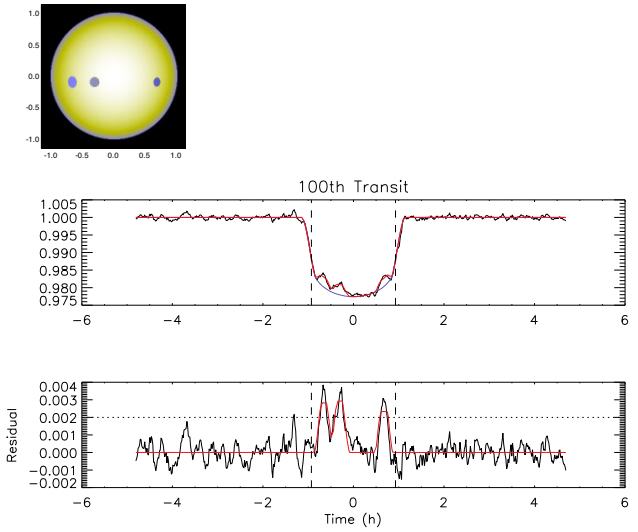

Figure 13 Top panel: Simulated star with three spots. Middle panel: The 100th transit light curve with a spotless model (blue) and the three spot model (red). Bottom panel: Residuals after subtraction of the spotless model from the transit light curve with the modelled three spots (red curve). Adapted from Valio et al. (2017).

active-region occultation on the Rossiter–McLaughlin effect signal (Oshagh et al. 2016; Boldt et al. 2020), as well as on the estimation of orbital configuration and properties of planetary systems (Oshagh et al. 2018) and active regions on their host stars (Oshagh et al. 2015; Serrano et al. 2020). SOAP-T is available via an online interface.[5]

3.4.3 PRISM

The Planetary Retrospective Integrated Starspot Model (PRISM; Tregloan-Reed et al. 2013) is written in IDL and uses a pixelation approach to model the stellar disc in a 2D array by subdividing the star into many individual elements. These elements can then be described by a 2D vector in Cartesian coordinates. Each element is then assigned an intensity value based on whether a stellar feature is present at that location and then the quadratic limb-darkening law is applied over the entire stellar disc. The planet is then set to transit the star. For each data point in the transit light curve, the total received intensity is calculated based on which elements of the star are visible. The PRISM model has been used primarily to model starspots found in ground-based transit exoplanetary light curves (e.g. Tregloan-Reed et al. 2013, 2015; Chen et al. 2017; Mancini et al. 2017). More recently, PRISM has also been used to simulate spotted transits observed with 2-min-cadence *TESS* data (e.g. Tregloan-Reed & Unda-Sanzana 2019, 2021). An example of the use of PRISM is provided by Fig. 14. PRISM is available on GitHub[6] and was last updated in 2019.

3.4.4 SPOTROD

SPOTROD (Béky et al. 2014) is a semi-analytic tool for modelling planetary transits of stars having an arbitrary limb-darkening law (being identical for spots and the stellar photosphere) along with a number of homogeneous, circular spots on the stellar surface. It can

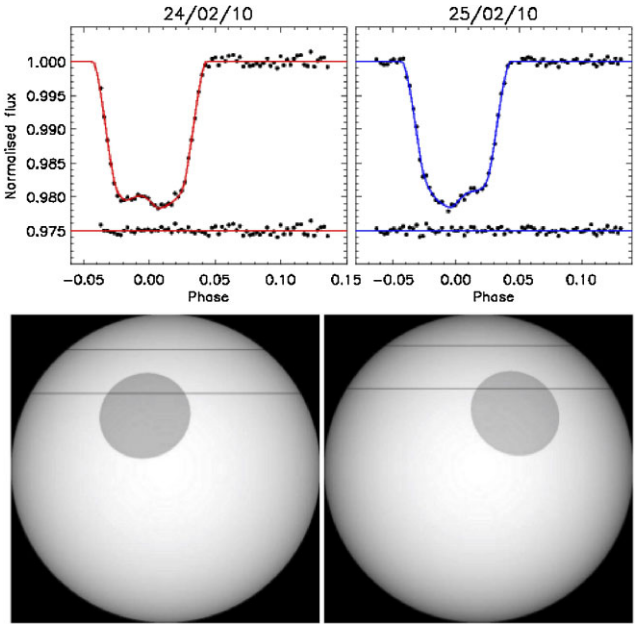

Figure 14 Top panel: Two consecutive transits of G8 V WASP-19 by the 0.8-d, hot-Jupiter WASP-19b from European Southern Observatory (ESO) NTT, along with the best-fitting PRISM model. The spot anomalies are clearly visible as upward blips around the midpoints of the two transits. Bottom panel: Representation of the stellar disc, starspot, and transit chord for the two data sets, showing the movement of the starspot between the consecutive nights. The stellar rotation axis lies in the plane of the page and points upwards. From Tregloan-Reed et al. (2013).

account for both eclipsed and uneclipsed starspots. The program is written in C and available in PYTHON. The homogeneous spots are represented by their flux ratio, f, which is the ratio of the flux from a spot (as viewed by the observer) to the flux from an unocculted stellar surface at the same disc location. Umbra-penumbra structures of spots can be accounted for by superimposing two concentric spots of differing intensities, and bright features can be introduced by using $f > 1$. SPOTROD works in polar coordinates, with the advantage being that the integral over the polar angle can be computed analytically and only the integral over the radial coordinate requires numerical integration. The significant reduction of the required computation time is the main advantage of this model compared with other, typically 2D, models. Thus, SPOTROD can be used for fitting large numbers of transits with occulted active regions and also for efficient statistical investigations using MCMC approaches. SPOTROD is available on GitHub[7] and was last updated in 2015. It has been wrapped into a nested-sampling retrieval framework, SpotNest (Espinoza et al. 2019), which is also available on GitHub[8] and was last updated in 2018.

3.4.5 StarSim2

StarSim2 (Rosich et al. 2020), an update of the StarSim tool (Herrero et al. 2016), uses a fine grid of surface elements to model integrated spectral contributions of a spotted rotating photosphere. It is written in PYTHON and FORTRAN 90. The flux intensities and wavelengths of spectral features produced by active regions are

[5] http://www.astro.up.pt/resources/soap-t/
[6] https://github.com/JTregloanReed/PRISM_GEMC
[7] https://github.com/bencebeky/spotrod
[8] https://github.com/nespinoza/spotnest

included in the model. The original StarSim tool has been used to derive stellar surface parameters from light-curve inversion as well as to mitigate their impacts on the transiting planet's transmission spectrum (Mallonn et al. 2018). StarSim2 is available on GitHub[9] and was last updated in 2020.

3.4.6 STSP

STSP is a fast forward model for starspot occultations by transiting exoplanets and unocculted spot modulation, written in C by L. Hebb and G. Rohn (Davenport 2015; Morris et al. 2017; Schutte et al. 2022). It computes the overlap between the planet, circular starspots with geometric foreshortening, and concentric nested discs of varying intensity to approximate stellar limb darkening. The code is highly efficient and coupled to a MCMC sampler also written in C, making it ideal for studies on high-performance computing facilities. STSP is available on GitHub[10] and was last updated in 2021.

3.4.7 ellc

ellc (Maxted 2016) is a semi-analytical and seminumerical model to analyse the light curves of detached eclipsing binary stars and transiting exoplanet systems. It can include the effects of both occulted and unocculted starspots simultaneously. It is implemented as Fortran subroutines called directly from a user interface written in PYTHON, and is fast enough to enable the use of modern Monte Carlo methods for data analysis and model testing. The source code is available at the Strasbourg Astronomical Data Center via anonymous file transfer protocol.[11]

3.4.8 Our finding: Finding 2.3

From this analysis, we draw the following findings:

Summary

Several publicly available tools have been developed for forward-modelling active-region occultations. Their maintenance and further development is necessary to ensure their utility for analyses of precise transit observations.

Capability needed

Publicly accessible, well-maintained, and up-to-date tools for modelling active-region occultations are necessary for analyses of precise transit observations from current and future facilities. A comparative understanding of the performance of these tools is also needed.

Capability today

Several publicly available tools exist for modelling for active-region occultations in broad photometric bandpasses today, including ECLIPSE (Silva 2003), SOAP-T (Oshagh et al. 2013a), PRISM (Tregloan-Reed et al. 2013), SPOTROD (Béky et al. 2014), StarSim2 (Rosich et al. 2020), STSP (Davenport 2015; Morris et al. 2017; Schutte et al. 2022), and ellc (Maxted 2016). However, many are not actively developed or maintained.

Mitigation in progress

Multiple groups have developed tools for modelling active-region occultations and made their source code publicly available. Continued development of some tools has been spurred on by recent analyses (e.g. Schutte et al. 2022).

[9] https://github.com/rosich/Starsim-2
[10] https://github.com/lesliehebb/stsp
[11] http://cdsarc.u-strasbg.fr/viz-bin/qcat?J/A+A/591/A111

4 UNOCCULTED ACTIVE REGIONS

Essential questions include the following:

(i) Can we learn about unocculted active regions through the study of transit depth variations in large photometric planet search surveys?
(ii) How well can other signatures of stellar activity in these data sets such as flares provide information about unocculted active regions?
(iii) What are the limitations of what we can learn about unocculted active regions from transit photometry?
(iv) Can additional photometric or spectroscopic data taken simultaneously with transit data help to better understand the information encoded in light curves?
(v) What data can best inform our knowledge of active-region filling factors?
(vi) How can we best distinguish between starspots and faculae?
(vii) Can we quantify the noise floor due to granulation as a function of stellar parameters?

4.1 Introduction

4.1.1 Motivation

Unocculted active regions on the heterogeneous surface of a star can impact measured transmission spectra of planets (e.g. Pont et al. 2008; Czesla et al. 2009; Rackham et al. 2017, 2018, 2019; Zellem et al. 2017). In transit photometry, the particular configuration of active regions produces a degenerate signal with an infinite number of different configurations, making unique identification of unocculted regions challenging. Moreover, while the most obvious signature of rotational modulation in broad-band stellar time-series photometry is often the signal from starspots, facular regions are expected to induce a more significant impact on transmission spectra due to their complicated spectral signatures (e.g. Cauley et al. 2018). In this section, we examine our understanding of unocculted regions and our ability to infer their presence before and during transmission spectroscopy of active stars.

4.1.2 Scope

We focus on three areas of interest here, primarily centred around the measurement and understanding of unocculted active regions rather than their impacts on atmospheric retrievals, which is instead discussed in Section 5. First, in Section 4.2, we investigate what information can be obtained about unocculted active regions from high-cadence transit photometry. In Section 4.3, we explore the usefulness of other data sets, current or planned, in understanding these regions. Finally, in Section 4.4, we discuss the effects of stellar granulation on transmission spectra.

4.2 Information from high-cadence transit photometry

High-cadence and high-precision transit photometry, such as that enabled by the *Kepler* and *TESS* missions (Borucki et al. 2010; Ricker et al. 2015), also encodes information about the underlying stellar surfaces. Here, we investigate opportunities from these data sets to directly infer properties of unocculted active regions.

4.2.1 Transit depth variations

Transit shapes can be affected by dynamical interactions between multiple planets or between a planet and its host star, which affects

the relative geometry of the system along our line of sight. Transit shapes can also be affected by variability on the stellar surface with no change in the geometry (Agol et al. 2005; Ragozzine & Wolf 2009; Barros et al. 2013). In this section, we explore how to disambiguate between the two.

Changes in the observed parameters of transiting planets have provided significant opportunities to understand planet–planet and star–planet dynamical interactions. The most dramatic result of a perturbation to a planet's orbital parameters is in the measured transit timing, which has been used to determine orbital configurations and planet masses, as well as to identify tidal inspiral of hot Jupiter systems (Maciejewski et al. 2016; Patra et al. 2020). In other systems, transit duration variations have provided information about orbital precession.

Transit depth variations, in which the magnitude of the depth of the transit changes over time, are at their most fundamental a change in the relative brightness of the occulted stellar chord compared with the unocculted starlight in the atmosphere. This change can be the result of a few different physical variations. The transit chord geometry itself could be changing as a result of dynamical interactions (Carter & Winn 2010; Hamann et al. 2019). The unocculted stellar surface could also change in brightness due to a change in the rotational phase of active regions or their emergence or decay. The occulted stellar surface could change in brightness for the same reason, producing an equivalent effect in the opposite direction.

The last of these possibilities is discussed more fully in Section 3. Here we note active regions on the occulted surface produce additional structure in observed transit photometry (Sanchis-Ojeda & Winn 2011), while unocculted active regions do not: Sufficiently high-precision photometry can disambiguate between these cases.

Separating depth variations from dynamical interactions compared with those from unocculted active regions is also possible. One straightforward consideration is that a change in the transit chord should also produce a change in the impact parameter, and thus the transit duration, while brightness variations should not significantly affect the transit duration as observed in broad-band photometry. Transit duration variations from long-term photometry can be detected at high confidence, with variations of $\approx$1 min yr^{-1} expected to be common (Boley, Van Laerhoven & Granados Contreras 2020). In most cases, duration variations should be more significant than depth variations (Holczer et al. 2016). Careful observations over a long temporal baseline, whether from the same telescope or others, can provide the evidence needed to separate these cases.

If a system is observed to have transit depth variations and not timing or duration variations, and there is no evidence for these variations to be predominantly caused by the growth of active regions along the transit chord, then it is plausible that this is the result of changes in the unocculted stellar surface. However, for *Kepler* and *TESS* photometry, the primary hindrance in inferring these changes is in identifying which stellar surface – that of the target star or another nearby – is changing. The *Kepler* telescope point spread function is approximately 6 arcsec in size; for *TESS*, it is typically 30–50 arcsec.[12] A typical photometric aperture used in the *Kepler* mission has a diameter of 10–20 pixels; for *TESS* the typical diameter is >1 arcmin. As a result, each aperture is contaminated by the light of multiple nearby stars, and it is not uncommon for the Exoplanet Follow-up Observing Program data base[13] to report 50 or more stars within 1 arcmin of a *TESS* object of interest (TOI). In addition, at least 25 per cent of TOIs have unresolved stellar binary companions (Ziegler et al. 2020), which can equally plausibly be the root of stellar brightness variations even when all known nearby stars can be ruled out. It is therefore challenging from transit photometry alone to determine whether a depth variation is due to a change in brightness of the target star, or a change in brightness of a background star, which would have an equivalent effect on the light curve.

This issue can be mitigated at some level by obtaining high-resolution imaging of these systems to limit the parameter space in which relatively bright nearby stars can evade seeing-limited detection (e.g. Law et al. 2014; Baranec et al. 2016; Ziegler et al. 2017). In order to remove neighbouring stars from the observed aperture, occasional monitoring of potential candidate transits with ground- or space-based telescopes with considerably higher pixel scales provides a benefit over large photometric surveys themselves. This sort of analysis (from the ground) is a common component of *TESS* candidate validation efforts (e.g. Wells et al. 2021; Delrez et al. 2022; Gan et al. 2022a, b; Schanche et al. 2022). An even more promising route would be to use the existence of transit depth variations in concert with other proxies of stellar activity indicators. For example, measurements of chromospheric activity indicators (e.g. Baliunas et al. 1995) could shed light on whether potential transit duration variations are due to the target star or some chance brightening of another star in the aperture.

4.2.2 *Active-region distributions*

In the context of transmission spectroscopy observations, not all active regions may be equally important to consider. Cauley et al. (2018) demonstrate that spectral line contrast absorption decreases dramatically as the separation between a planet and an active latitude increases, with the most significant events occurring when the two are within five degrees of each other. Although not all planets have a low obliquity between their orbital axis and the stellar spin axis (Winn et al. 2010), for the systems where the obliquity can be measured, this consideration can impact our interpretation significantly if we can determine the distribution of active regions on the surface of the star.

Inferring the 2D distribution of active regions on a stellar surface from 1D transit photometry is an ill-posed and degenerate problem, with different stellar surface models able to produce identical light curves (Vogt, Penrod & Hatzes 1987; Basri & Shah 2020; Luger et al. 2021b). This is the case even if one is trying to recover information on dark (or bright) features alone. However, the problem is compounded as active regions typically contain bright (facular or plage-like) features and dark spots. The contributions from these can add or partially cancel, depending on the location of the features, the wavelength at which the star is observed, and the feature size (or magnetic field strength) and the stellar spectral type. The contribution of faculae is particularly poorly characterized (see Sections 2.3.3 and 5.3).

In general, longitudinal information is more easily recovered than information about the latitudes of unocculted active regions (Luger et al. 2021b), although this is complicated further by the potential of active regions that manifest at all longitudes, such as a banded region or a polar spot. While there is some asymmetry even in banded features, their photometric signal is only representative of the asymmetry rather than the total filling factor, requiring other techniques to infer their structure.

As discussed in Section 3, significantly more information can be learned about the size and structure of active regions when they are

[12] For both telescopes, the point spread function is a strong function of location on the focal plane and, more weakly, a function of magnitude and colour.
[13] https://exofop.ipac.caltech.edu/tess/

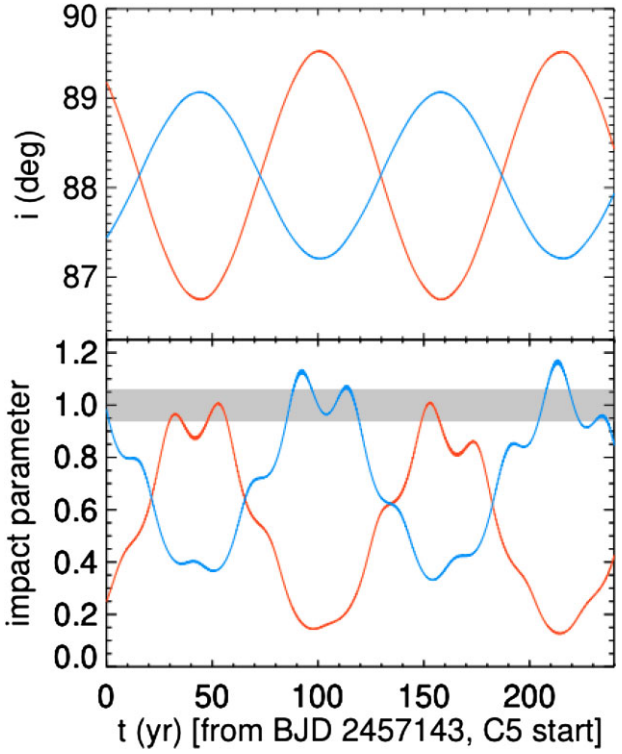

Figure 15 Long-term evolution of the (top panel) inclination and (bottom panel) observed impact parameter of the two planets in the K2-146 system. Over time-scales of a decade, the impact parameters from both planets can vary by as much as 10 per cent, causing previously occulted active regions to become unocculted and vice versa. From Hamann et al. (2019).

occulted by a planet. In the context of transmission spectroscopy, the most promising avenue to use transit photometry to understand active regions outside of a narrow transit chord is to consider multiplanet systems with strong dynamical interactions. Over years to decades, multibody perturbations can affect neighbouring planets' inclinations by a few degrees; in some cases, planets can move from transiting the stellar equator to not transiting.

The K2-146 system, described by Hamann et al. (2019) and Lam et al. (2020), provides an example of these perturbations in action (Fig. 15). Over 10 yr, the impact parameter for both planets can change by 10 per cent, leading to a ∼10-degree change in the projected latitude of the transit chord on the surface of the star. Regular monitoring of occulted active regions over many years can then give a broader understanding of unocculted surfaces at the time of transmission spectroscopy observations, especially those surfaces within a few degrees of the transiting planet that are most critical for interpreting the transmission spectrum.

It is also helpful to know the inclination and rotation period of the star, and to observe a large number of rotations (Basri & Shah 2020). This could, in particular, help to distinguish between the effects of the active regions on the light curves due to the stellar rotation (change in the projected area and contrasts) and the evolution of active regions (e.g. redistribution of the magnetic flux between the dark and bright components leading to a change in their relative contributions as well as flux decay). Furthermore, a promising tool to distinguish between the signatures of planets, starspots, and faculae in the light curves is offered by multiband photometry, due to the different centre-to-limb contrasts of the different occulters (see Section 4.3.1 for further details).

4.2.3 Stellar flares

The presence of unocculted active regions can also be traced in principle by measuring the occurrence rate and energy of stellar flares. *Kepler* and *TESS* have been effective flare-finding missions (e.g. Davenport 2016; Günther et al. 2020). Flares appear in these light curves as stochastic spikes, which can be separated from slower and usually weaker variations or sources of noise (Feinstein et al. 2020). Since flares are distinct events, it can be easier to unambiguously measure their specific occurrence rate for stars, compared with the degeneracies in estimating the true filling factor of, e.g. starspots, as discussed above.

Detailed statistical analyses of flares on Sun-like stars (e.g. Maehara et al. 2015; Notsu et al. 2019; Okamoto et al. 2021) are limited in their ability to compare directly to the Sun itself: The smallest flares on Sun-like stars observed by *Kepler* are still more energetic than the largest flares observed on the Sun or even than the upper limit on the possible solar flare energy (Schrijver et al. 2012; Aulanier et al. 2013). Yet these so-called superflares seem to follow the same relationship between occurrence and emitted energy as smaller flares, suggesting a common physical origin. There is clear and convincing evidence that the energies of solar flares are correlated with the magnetic energy in active regions on the Sun (Mayfield & Lawrence 1985). For example, flare rates on the Sun are ∼10 times higher during activity cycle maximum, when the largest number of sunspots and active regions are present (Aschwanden & Freeland 2012). Three potential extreme solar particle events, identified by Brehm et al. (2021) in the newest radiocarbon data with annual resolution, all occurred close to solar activity maxima (Usoskin et al. 2021). Notsu et al. (2013) similarly demonstrate that the energies of superflares observed on solar-type stars trace the total starspot coverage on these stars. Yet the occurrence of strongest flares or flare candidates on the Sun does not seem to be closely correlated with the strength of the cycle, and strong events can happen even during relatively weak cycles (Bazilevskaya et al. 2014; Omodei et al. 2018; Usoskin et al. 2021). From an analysis of main-sequence stars, Roettenbacher & Vida (2018) found that only low-amplitude flares were correlated with observed starspot phase.

For stars that are different from the Sun, there are more uncertainties about the relationship between active-region coverage and flare frequency, making flare frequency a more difficult proxy to interpret for transmission spectroscopy analyses. On the other hand, tracing flare energies on stars provides us with key information about the overall active-region coverage on these stars. Studies of the spectral behaviour of flares on M dwarfs are useful for constraining radiative HD flare models and thus areal coverages of active regions associated with flares (Kowalski et al. 2013). However, locating these active regions on the stellar surface is not possible from observing the flares alone, somewhat limiting our ability to infer the impact of these active regions on exoplanet transmission spectra.

Doyle et al. (2018) find no correlation with rotational phase for any flares on M dwarfs, an interpretation matched by Feinstein et al. (2020) in an analysis of stars in young moving groups. These observations may suggest very large (≈80 per cent) active-region filling factors are typical for M dwarfs and young stars, consistent with values inferred via spectroscopic methods of the young star LkCa4 (Gully-Santiago et al. 2017), or may suggest variations in the underlying relations between active-region size and flares on non-Sun-like stars. For M dwarfs, flares may primarily occur from smaller active regions spread across the entire photosphere, while the starspot modulations observed by *Kepler* and *TESS* may be tracing larger and more stable active regions or 'spot caps' (Hawley et al.

2014). There is an opportunity for continued theoretical modelling of active regions on these stars to be combined with the additional photometry for young and low-mass stars that will be collected over the coming years with *TESS* to more fully understand the relations between flares and active regions on stars different from the Sun.

4.2.4 *The potential for improved data analysis methods*

While some features of active regions, such as the overall latitude distribution, can demonstrably not be uniquely inferred from transit photometry, here we consider what limitations may be due to current data processing practices.

The *Kepler* and *TESS* data analysis pipelines are motivated by the search for exoplanets. While they do try to preserve stellar signals when possible, attempting to maintain those signals is sometimes at odds with the goal of planet detection.

Planet transits are relatively small signals (hundreds of ppm) with sharp features, few-hour time-scales, and characteristic shapes, and are mostly achromatic. Therefore, relative precision is only needed on time-scales of hours to a few days, while slow variability can be effectively removed by data processing pipelines. Since the signals are nearly achromatic, single-bandpass broad-band photometry is acceptable for finding transits.

Significant effort has been made towards increasing the photometric precision achievable by analysing these data for transits, though there is clear evidence that additional information can be recovered to better understand the observed stars themselves. For example, Montet et al. (2017) used the *Kepler* full-frame images, a set of calibration data obtained approximately monthly over the *Kepler* mission, to calibrate photometry from that telescope and measure absolute brightness variations over multiyear time-scales. That data product provides the opportunity to probe the relative contributions of facular and spot regions on the surface of the star as they grow and decay due to changing activity levels.

Similarly, Hedges et al. (2021) characterized the colour dependence of the *Kepler* point spread function, enabling identification of changing average stellar temperatures (and thus colours) over the course of the mission. This technique has the potential to further our knowledge of large active regions, possibly breaking some degeneracies between starspot size and temperature by providing effective multiwavelength photometry over a 4-yr baseline. It also could enable improved inference of temperatures of stellar flares observed by *Kepler*.

Further development of new data analysis methods for *Kepler* and *TESS* data can help understand unocculted active regions in spaces where information may be quashed by the instrument pipeline or otherwise overwhelmed by systematic effects. Possible opportunities where significant progress may be both achievable and particularly beneficial include the improved recoverability of low-amplitude or long-period rotational modulation, the characterization of the smallest flares, and the development of machine learning methods to separate astrophysical and instrumental signals.

4.2.5 *Our finding: Finding 3.1*

From this analysis, we draw the following findings:

Summary

High-cadence light curves provide the potential to understand unocculted active regions, but the information is not comprehensive enough to make unambiguous measurements at present. Theoretical advances are needed to make full use of these light curves.

Capability needed

Significant theoretical work is needed to understand the relations between observational signatures of stellar activity in light curves. Continued advances in data analysis methods developed to re-analyse archival data sets can provide major improvements in our ability to leverage information from precise light curves.

Capability today

The large data sets provided by missions such as *Kepler* (Borucki et al. 2010) and *TESS* (Ricker et al. 2015) have enabled the development of data-driven methodologies for studying unocculted active regions through photometry (e.g. Montet et al. 2017; Hedges et al. 2021; Luger et al. 2021a). These same data sets are producing opportunities for improved data analysis tools (e.g. Lightkurve Collaboration et al. 2018; Feinstein et al. 2019). Efforts like these can be supported by programs such as the NASA Astrophysics Data Analysis Program.

Mitigation in progress

The NASA–NSF Extreme Precision Radial Velocity (EPRV) initiative,[14] a strategic effort to develop methods and facilities for measuring the masses of temperate terrestrial planets orbiting Sun-like stars, has enabled opportunities for the development of theoretical work to improve our understanding of the effects of stellar activity on time-series spectroscopy (e.g. Newman et al. 2023), which is a parallel need to the theoretical work outlined here.

4.3 Information from other data sets

In characterizing the effects of unocculted active regions on transmission spectra, the high-cadence photometry obtained to discover these systems does not exist in a vacuum. Here, we consider other observations, whether or not they are obtained simultaneously with the transmission spectrum, and their ability to understand active regions. Solar observations show that the absolute as well as the relative surface coverage of spots and faculae (or plage) varies as a function of time. As the transmission spectrum 'contamination' depends on the feature contrasts in the given spectral band, a single active-region tracer is generally insufficient and ideally two active-region tracers should be combined, ideally with very distinct sensitivity levels to bright and dark active-region components.

4.3.1 *Multiband photometry*

Both *Kepler* and *TESS* observe with a single broad-band filter. With simultaneous observations at multiple wavelengths, the changing colour of an active stellar surface over time can be inferred. This strategy has been used to determine temperatures of stellar flares (Howard et al. 2020), and there is a long tradition of using multiband photometric light-curve modelling to infer spot temperatures and covering fractions on active stars (see Section 2.4.2 and Berdyugina 2005 for a review on starspot properties and observations). While multiband photometry can lift some of the degeneracies between filling factors and active-region temperatures (e.g. Rosich et al. 2020), spot contrasts only vary slowly as a function of wavelength, meaning that spot temperature determinations remain very uncertain. Recovering active-region filling factors becomes even more of a problem when trying to map spots and faculae simultaneously using broad-band photometry. However, as facular regions have a much stronger spectral signature than starspot regions (Shapiro et al. 2014), narrow-band photometry focused on particular spectral regions (e.g.

[14] https://exoplanets.nasa.gov/exep/NNExplore/EPRV/

Ca II H & K and molecular bands such as CN bands, the CH G-band, or the TiO band in the red optical; Zellem et al. 2010) could provide an outsized benefit in understanding the distributions of faculae, motivating future theoretical modelling. These spectral regions are also discussed more fully in Section 4.3.4.

Work by Milbourne et al. (2021) suggests that for solar twins, where spot and facular contrasts are relatively well constrained by theory and solar observations, it should be possible to recover spot and facular filling factors using a combination of high-fidelity broad-band photometry and a magnetic-activity tracer such as the Ca S-index (which can either be obtained using high-resolution spectroscopy or narrow-band photometry). The first results are promising (Fig. 16), though they rely on accurate knowledge of the spot and facular contrasts. There is also both theoretical and observational evidence that spot and facular contrasts are affected by stellar metallicity, but the effects have not been fully explored in detail for a large population (Karoff et al. 2018; Witzke et al. 2018). Thus, more information on active-region contrasts for different spectral types and metallicities is needed before this can be extended to stars with non-solar spectral types. Further work will also be needed to explore how the location and relative importance of spots and faculae affects such reconstructions.

To map and understand the distribution of faculae, their spectral signatures should be further explored. Faculae have strong UV contrasts, though this has as yet been not fully explored, mainly due to a lack of time-resolved UV photometry. Broadly, optical photometry has been traditionally considered to retrieve stellar heterogeneities from long-term photometry, with the Strömgren b and y filters commonly considered (e.g. Gray 2005). Far UV photometry may provide a promising addition to this set, though current capabilities may enable only a limited benefit compared with monitoring of stellar calcium emission features (Findeisen, Hillenbrand & Soderblom 2011). In the NIR, there is some evidence that signatures of stellar activity may be even smaller than anticipated for some young stars (Miyakawa et al. 2021), making them a suboptimal choice to measure long-term photometric variability. However, Stefansson et al. (2018) highlight a promising custom filter, 300-Å wide and centred at 8570 Å. This filter spans the Ca II IR triplet (8498 Å, 8542 Å, 8662 Å) and minimizes the effects of telluric absorption. These authors suggest this filter offers an inexpensive opportunity to study stellar activity in the NIR; further work should be undertaken to determine the usefulness of this or other potential bandpasses, spanning features such as the Na D doublet (5890 Å, 5896 Å) or the metastable He 10 830-Å line (e.g. Vaughan & Zirin 1968), in the context of identifying and quantifying the extent of stellar surface heterogeneities.

4.3.2 *Long-term photometry*

For many bright stars, additional photometry exists from ground-based surveys with long temporal baselines, i.e. extending 10 yr or more before the present day. These data are often leveraged by the exoplanet community to great effect in the confirmation and characterization of planetary systems, demonstrating their utility in combination with high-cadence transit photometry. In particular, the Wide Angle Search for Planets (WASP; Pollacco et al. 2006), Kilodegree Extremely Little Telescope (KELT; Pepper et al. 2007), and All Sky Automated Survey for SuperNovae (Kochanek et al. 2017) surveys often have the precision to separate planet candidates from background eclipsing binaries and infer stellar rotation periods through starspot modulation. On much longer time-scales, the Digital Access to a Sky Century @ Harvard survey (Grindlay et al. 2009, 2012) provides photometry with 0.1 magnitude precision over 100 yr through the digitization of a photographic survey that began in 1885. These data have been used to study long-term variability in the *Kepler* field (Tang et al. 2013).

These data sets offer a tradeoff between time baseline and photometric precision, with a century of data available at ≈10 per cent precision or a decade at ≈1 per cent precision. They can be used to measure photometric variability at these precisions as well as changes in variability over time (e.g. Lanza et al. 1998; Gully-Santiago et al. 2017), owing to activity cycle evolution or the growth and decay of large polar spots.

While these data have information about unocculted active regions that can be used to understand the overall activity level of the star, they are collected years or decades before the transmission spectra are obtained. Long-term observations do provide data on the relative overall activity of the star at the current time, through spectroscopic tracers such as a single measurement of chromospheric activity from the Ca II H and K lines can provide a similar level of information contemporaneously with the transmission spectrum. There is currently a paucity of theoretical motivation suggesting that these observations can provide useful information in interpreting a transmission spectrum. The converse has even been suggested: Iyer & Line (2020) suggest that prior knowledge of stellar heterogeneities does not improve precision in planetary parameters achievable from an atmospheric retrieval if the heterogeneities are appropriately marginalized. Expanded theoretical work highlighting benefits of this long-term photometry specifically in the context of transmission spectroscopy would help to motivate the future utility of these data in this context.

4.3.3 *Interferometry*

The nearby active star ζ And is among the so far few stars for which a global surface temperature map has been successfully constructed via aperture synthesis imaging (Roettenbacher et al. 2016). The data, which were obtained with the interferometric Center for High Angular Resolution Astronomy (CHARA) Array at a wavelength of 1600 nm and an angular resolution of 0.5 mas, reveal variations in the surface temperature that are related to starspots.

Interferometric observations are possible with present technology only for bright stars with large angular sizes; these are typically red giants. Recent work has enabled constraints on the spot locations for the K2V exoplanet host ϵ Eridani through a combination of RV spectroscopy, *TESS* photometry, and interferometry with the Michigan InfraRed Combiner-eXeter (MIRC-X) six-telescope interferometric imager at the CHARA array (Roettenbacher et al. 2022), though the spot detections are marginal with this data set, underscoring the challenge of imaging exoplanet hosts. Thus, the primary utility of optical interferometry at present is in enabling a better understanding of possible configurations of active regions on stellar surfaces, which can be compared with theoretical models to provide constraints on the stellar dynamo. In the context of transmission spectroscopy, an important step is theoretical modelling of the differences between the dynamo and resultant magnetic fields between typical planet-hosting stars and the giants that are observable with optical interferometry.

4.3.4 *Low- and medium-resolution spectroscopy*

Photometric observations of active stars can be used to identify active regions, especially starspots. However, they typically produce

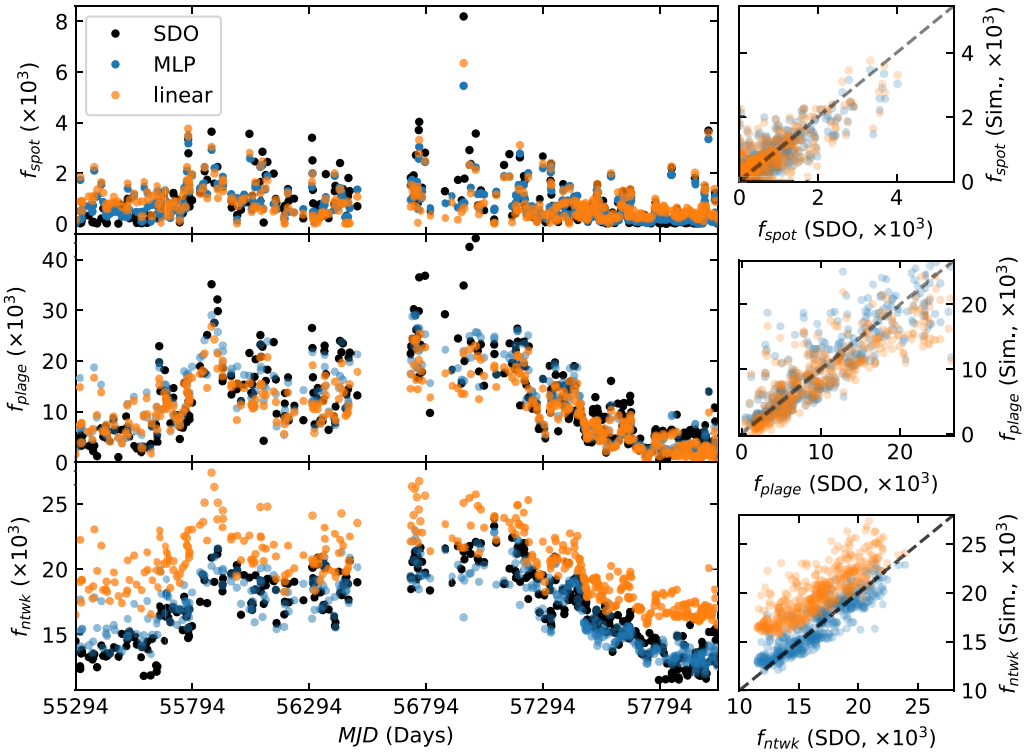

Figure 16 Spot (top panel), facular (middle panel), and network (bottom panel) filling factors as obtained from SDO (black dots; obtained using segmentation) and reconstructed using TSI and Ca S-index time series. Blue symbols are for a machine learning algorithm, orange symbols are from linear fitting. From Milbourne et al. (2021).

a degeneracy between filling factors and active-region temperature: A given amount of photometric modulation could be produced by a relatively small but very dark starspot or a larger spot with a relatively small differential between its temperature and the unocculted stellar surface. Low- and medium-resolution spectroscopy can offer a more detailed view than photometry, provided the instrumental stability is sufficient to monitor relatively subtle spectral changes. An example of (facular-dominated) solar cycle variability observed at mid-resolution ($R \sim 1000$) with the Ozone Monitoring Instrument (OMI) onboard the NASA Aura Mission is shown in Fig. 17 (Marchenko et al. 2019). The blue and UV wavelength regions are of particular use here as facular contrasts are much larger at shorter wavelengths. A number of relatively broad spectral features stand out, such as the Ca II H & K lines, the CH *G* band, and the CN violet system (see Section 4.3.1).

Despite recent advances (Panja et al. 2020), generally little is known about contrasts of active regions on stars of spectral types other than the Sun, and more theoretical work is needed to understand and model bright features (see Section 5.3). Magnetoconvection simulations show that faculae will become less bright for later spectral types, in particular for M stars (Beeck et al. 2015a). Preliminary calculations suggest variability in the CN and CH bands will decrease, while TiO bands become more important; at the same time, facular UV contrasts remain comparable to those observed for Sun-like stars (Norris 2018).

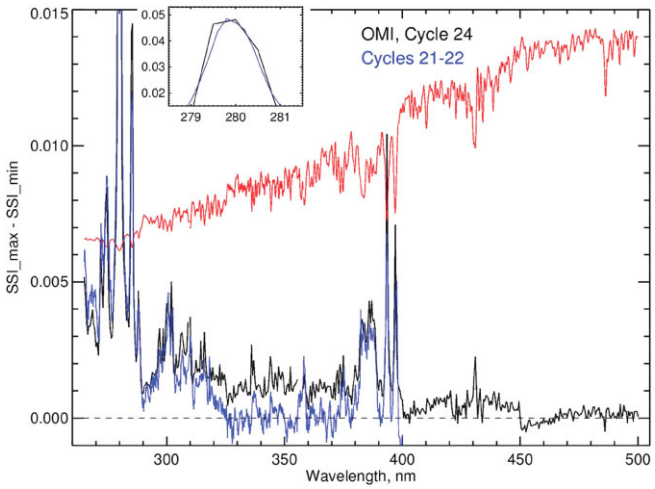

Figure 17 Spectral solar-cycle variability for cycle 24 as observed by Aura/OMI (black line; the blue line shows the cycle 21 and 22 variability below 400 nm scaled to match the cycle 24 variability for Mg II). Enhanced variability is clearly seen in the Ca II H & K lines as well as the CN violet band (between ∼380 and 390 nm), and the CH *G* band (at 430 nm). From Marchenko et al. (2019).

4.3.5 High-resolution spectroscopy

Much as in the low-/medium-resolution spectroscopy discussed in the previous section, high-resolution spectroscopy can be used to better understand active-region filling factors. With sufficiently high resolution, molecular bands can be detected at high significance. Spectroscopic signatures of molecular features are strong functions of temperature and pressure, so these features provide an ideal laboratory to understand the stellar surface as the sum of multiple components at different temperatures (e.g. Berdyugina et al. 2003). For example, O'Neal, Saar & Neff (1998) demonstrated that the active K star II Peg had a coverage fraction of ∼50 per cent from

observations of TiO molecular bands. Gully-Santiago et al. (2017) showed an even higher filling factor for the young star Lk Ca 4 using the same molecular features. In fact, the most studied active K stars II Peg and IM Peg were never observed in their unspotted states, as evidenced by the continued presence of variable TiO bands in their spectra (Neff et al. 1995; Berdyugina et al. 1998, 1999). Thus, the disappearance of the TiO bands forming only in cool spots can provide the reference for the unspotted stellar atmosphere and brightness (Berdyugina et al. 1998). Similar observations of other stars at different levels of activity remain critical to understanding overall active-region filling factors and thus the underlying sizes, atmospheric parameters, and distributions of active regions.

Additionally, molecular features trace the stellar magnetic field through their polarization (Berdyugina 2011). High-resolution spectropolarimetry of these lines provide estimates of magnetic fields on active stars, also directly within spatially unresolved spots (Berdyugina 2002; Berdyugina et al. 2006). In particular, Afram & Berdyugina (2015) highlight that high-resolution spectropolarimetry of TiO on M dwarfs, CaH on K dwarfs, and MgH and FeH on G dwarfs provide particularly promising avenues to understand stellar magnetic fields. This has been demonstrated for M dwarfs by studying atomic and molecular spectropolarimetric signatures, revealing variations of the magnetic field complexity on stellar surfaces, with the height in the atmosphere and depending on the stellar effective temperature (Berdyugina 2011; Afram & Berdyugina 2019).

EPRV observations to measure planet masses and orbits also require care to mitigate the effects of active regions on stellar spectra (e.g. Robertson et al. 2014; Robertson, Roy & Mahadevan 2015). Considerable effort has been expended to attempt to separate the effects of stellar active regions from planetary signals. These efforts have been successful in developing methods that can effectively predict the radial velocity (RV) signal from active regions from observed photometric variability (e.g. Aigrain, Pont & Zucker 2012) and to model the surfaces of very active stars to measure the masses of their planets (e.g. Barragán et al. 2019). Observations of the Sun with the High Accuracy Radial velocity Planet Searcher for the Northern hemisphere spectrograph also demonstrate that RVs can effectively be modelled in the face of known active-region distributions (Milbourne et al. 2021).

A common finding in EPRV studies of active regions is the importance of simultaneous photometry and spectroscopy to condition data-driven models. Having both data sets is critical in many cases to measure planet masses (Oshagh et al. 2017); it is likely that in many cases simultaneous observations will also provide a benefit to uniquely characterize unocculted active regions in transmission spectroscopy data.

4.3.6 Conclusion

Each of the methods described in this section holds the potential to improve our understanding of unocculted active regions for transmission spectroscopy. While there is evidence from EPRV observations that simultaneous photometry is highly important for active stars, it is not as obvious for stars with lower activity levels. An important step forward is not just understanding what data additional sets are important, but to what level the answer is a function of spectral type, age, and/or activity level. Theoretical work that can effectively predict the effects of stellar activity on transmission spectra would be beneficial in answering this question.

4.3.7 Our finding: Finding 3.2

From this analysis, we draw the following findings:

Summary

Simultaneous multiband photometry and contemporaneous spectroscopy provide critical information towards understanding the potential effects of active regions on transmission spectroscopy observations. While other data sets can provide information on filling factors, theoretical work is needed to maximize the utility of these data for transmission spectroscopy.

Capability needed

A better understanding of the emergent flux from stellar active regions, including both photometric (i.e. spectral energy distribution, SED) and spectral signatures (e.g. Na D doublet, Ca II IR triplet, He 10830 Å, etc.), especially for spectral types and metallicities other than the Sun, is essential to robustly interpret transmission spectra.

Capability today

There is a relatively good understanding of active-region contrasts for solar twins from solar observations and modelling. Models including calculated spot and facula contrasts as a function of wavelength and limb angle can accurately reconstruct solar irradiance variations on time-scale of the solar rotation (Fligge et al. 2000) and solar magnetic cycle (Krivova et al. 2003). Extended to other stars, these models can reproduce the observed photometric variability of Sun-like stars using different coverages of magnetic features (Shapiro et al. 2014). Using a combination of spectroscopy and photometry, the coverage of both spots and faculae on Sun-like stars can similarly be constrained (Milbourne et al. 2021).

Mitigation in progress

Ab initio modelling of emergent fluxes from spots and faculae for different spectral types is being developed by multiple research groups (e.g. Norris et al. 2017; Panja et al. 2020; Witzke et al. 2022).

4.4 Stellar granulation

One of the ultimate sources of an astrophysical 'noise floor' in stellar light curves is stellar surface granulation. Because it is a fundamental feature of stars with convective envelopes (i.e. $T_{\rm eff} \lesssim 6700$ K), it represents a true lower limit to the photometric variability that any star can attain. This is summarized in Fig. 9, where the lower 'granulation flicker floor' shows the lowest possible photometric variability amplitude for otherwise inactive stars, as a function principally of the stellar surface gravity, $\log g$. On the time-scale of typical planet transits (i.e. $\lesssim$8 h), in the *Kepler* bandpass (i.e. visible light), the 'granulation flicker' noise ranges from $\sim$0.02 ppt for the least active dwarfs to $\gtrsim$0.4 ppt for the least active giants.

The amplitude of the 'granulation flicker' noise scales with the granule/intergranule brightness contrast, which is minimized at longer wavelengths. For example, the granular brightness contrast for a solar-type star is $\sim$100 times lower at 10 μm than in visible light. Thus, for inactive dwarfs, the 'granulation flicker' noise at 10 μm should be as low as $\sim$0.2 ppm on planet-transit time-scales.

While these are relatively small contributions to the overall stellar photometric noise, from the standpoint of a planet transit spectrum, the impact can become the dominant source of uncertainty, particularly for transits around larger stars and at shorter wavelengths. That is because a larger star of a given mass will have a lower surface gravity, hence a stronger granulation signal, and as noted above, that signal is strongest in the visible. Morris et al. (2020) examined the impact of granulation on observations from the ESO PLAnetary Transit and Oscillations (PLATO) mission (Rauer et al. 2014), and Sulis et al. (2020) performed a similar analysis for both

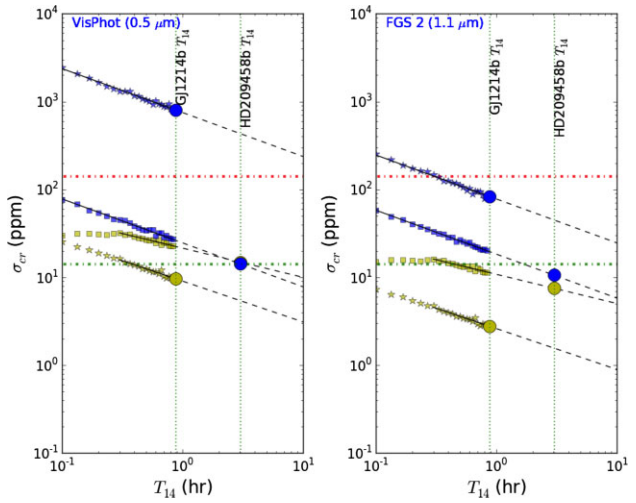

Figure 18 Simulations of the relative noise contributions to planet-transit depth fractional uncertainty (σ_{cr}) due to stellar pulsation and granulation (yellow) and photon noise (blue) as a function of transit duration. The cases of a hot Jupiter orbiting a G0V-type star (HD 209458b; squares) and a super-Earth orbiting an M4.5V-type star (GJ 1214b; stars) are shown for two filters of the Ariel Space Mission, VisPhot (visible; left-hand panel) and FGS 2 (NIR; right-hand panel). The black dashed lines give power-law fits to the noise levels, and the upper red and lower green dash–dotted lines show the Ariel noise floor requirement and goal, respectively. For each planet, compare the large yellow dot to the large blue dot; this is the relative contribution of stellar granulation noise to photon noise for atmospheric retrieval. Note that in the left-hand panel (visible light), the yellow and blue dots overlap for HD 209458b, meaning that the stellar granulation noise begins to dominate the error budget. From Sarkar et al. (2018).

PLATO and CHaracterising ExOPlanet Satellite (CHEOPS; Benz et al. 2021) observations. These simulations show that for planets transiting Sun-like stars observed in the visible, the absolute error on the retrieved planet radius due to granulation noise can be as large as ∼2 per cent and ∼10 per cent for super-Earth and Earth-sized planets, respectively. Indeed, CHEOPS commissioning observations of the bright, G8/K0 subgiant KELT-11 show granulation-induced variability with an amplitude of 200 ppm (Benz et al. 2021), in line with these predictions.

In practice, stellar granulation can impact the transit spectrum thus in two ways. The first and most obvious one is the one related to the extra noise this granulation adds to light curves, effectively setting a lower limit to the possible precision attainable on the retrieved transit depths as a function of wavelength. This source of noise, however, should be minor in most cases. While studying this, Sarkar et al. (2018) considered the relative and absolute contributions to the error budget for atmosphere retrieval of the planets HD 209458b (a hot Jupiter orbiting a G0V-type star) and GJ 1214b (a super-Earth orbiting an M4.5V-type star). The results are summarized in Fig. 18 and Table 4, where we see that in the worst case (HD 209458b in the visible), where the stellar noise from granulation dominates over the photon noise, the impact on the transit-depth measurement for atmospheric retrieval is at most ∼0.05 per cent.

The second way in which granulation could impact on the transit spectrum, however, is through the TLSE, similar to the impact caused by unnocculted spots and faculae described by Rackham et al. (2018, 2019), but produced by the effectively different granulation pattern in different parts of the stellar surface. This is an effect that Chiavassa et al. (2017) studied through 3D simulations using the STAGGER grid and synthetic images computed with the radiative transfer code

Table 4. Tabular summary of Fig. 18. Relative uncertainty in planet transit depth for the two representative cases (in ppm), and the resulting absolute uncertainty on the planet radius for atmospheric retrieval (in per cent) for different wavelength regimes of observation. From Sarkar et al. (2018). Details of the listed spectral channels can be found in Tinetti et al. (2018).

Channel (μ m)	GJ 1214b		HD 209458b	
	$\sigma_{cr,\,sn}$ ppm	$\frac{\sigma_{R_p,sn}}{R_p}$ per cent	$\sigma_{cr,\,sn}$ ppm	$\frac{\sigma_{R_p,sn}}{R_p}$ per cent
AIRS Ch1 (3.9–7.8)	1.5	0.01	3.6	0.01
AIRS Ch0 (1.95–3.9)	2.3	0.01	3.5	0.01
NIRSpec (1.25–1.9)	3.1	0.01	4.5	0.02
FGS 2 (1.1)	2.8	0.01	7.5	0.03
FGS 1 (0.9)	4.4	0.02	9.0	0.03
VisPhot (0.5)	9.6	0.04	14.9	0.05

OPTIM3D (Chiavassa et al. 2009). The study concluded that the impact of this contamination could be as large as a few per cent in the transit depth of small, terrestrial exoplanets orbiting Sun-like stars at 0.7 μm. While Chiavassa et al. (2017) did this experiment with simulations for both a Sun-like star and a K-dwarf star, it is unclear how big this impact is in reality, and how realistic those simulations are both as a function of wavelength and granulation amplitudes. This latter effect is one that should be studied in detail, especially given missions such as the ones proposed in the Astro2020 Decadal Survey, which could perform precise optical spectrophotometry.

4.4.1 Our finding: Finding 3.3

From this analysis, we draw the following findings:

Summary

Stellar 'granulation flicker' constitutes a fundamental 'noise floor' on stellar light curves that increases with decreasing stellar surface gravity and at shorter wavelengths. The impact of this stellar granulation can enter as a source of noise and/or contamination for transmission spectroscopy in two ways. The first is through extra light-curve scatter, the impact of which is minimal in most cases (at most ∼0.05-per cent error on the transit depth in the visible and even less at longer wavelengths). The second is through a contamination source similar to that of spots and faculae, albeit at a much lower amplitude (∼ 1 per cent of the transit depth at about 0.7 μm). This second source is significant at short wavelengths for smaller exoplanets around Sun-like stars, but decreases strongly as a function of wavelength.

Capability needed

3D granulation simulations need to be validated against observed light curves as a function of spectral type and wavelengths relevant for future space-based observatories (∼0.3–5 μm). Simulations of exoplanets crossing those simulated stellar surfaces should be used further to study the full impact of these features as a contamination source in the transmission spectrum of high-profile exoplanet systems.

Capability today

Granulation is well understood in large optical bandpasses from space-based missions such as *Kepler*, *TESS*, and CHEOPS. Methodology is in place in order to understand and analyse its amplitude given an observed precise light curve. 3D stellar models can be used to model granulation as a function of wavelength for different spectral types. CHEOPS observations of the G8/K0 subgiant KELT-11 show granulation-induced variability of 200 ppm (Benz et al. 2021) that is in line with predictions (Sulis et al. 2020). For future

Ariel observations, simulations show that the impact of granulation can be comparable to photon noise uncertainties for a 3-h transit of the G0V HD 209458 (Sarkar et al. 2018). Similarly, simulated transits of the Sun show that solar oscillations and granulation produce signals with an amplitude of 100 ppm, producing a planetary radius uncertainty that accounts for a significant fraction of the error budget of the PLATO mission (Morris et al. 2020).

Mitigation in progress

All-sky missions such as *TESS* can retrieve the properties of the granulation signal for high-profile exoplanet host stars (Campante et al. 2016; Stassun, Collins & Gaudi 2017). Studies of the impact of oscillations and granulation on Ariel (Sarkar et al. 2018), CHEOPS (Sulis et al. 2020), and PLATO (Morris et al. 2020) have recently been carried out.

5 STELLAR AND PLANETARY RETRIEVALS

Essential questions include the following:

(i) What is the state of the art for stellar and planetary retrievals of transmission spectra?
(ii) What wavelengths and resolutions are necessary for useful constraints on active-region contrasts and coverages? Do these requirements vary with spectral type?
(iii) What are the best practices for propagating stellar spectral information into atmospheric retrievals of transit observations?
(iv) What additional information is necessary to uniquely disentangle stellar and planetary signals via retrievals?
(v) What are the limitations of using retrievals to disentangle stellar and planetary features?
(vi) What future work should be pursued in this context?

5.1 Introduction

As noted in Section 1, a primary concern with transmission spectroscopy is the potential of unocculted active regions (including, e.g. spots or faculae) to alter transit depths through the TLSE (see Fig. 19) and, thus, bias inferences of the properties of the exoplanetary atmosphere. Here, we examine the state of the art for Bayesian frameworks that jointly fit for the properties of a planetary atmosphere and a heterogeneous stellar photosphere, i.e. one with magnetic active regions. We begin by defining more precisely these retrieval frameworks and outlining the scope of our analysis.

5.1.1 Retrievals

Atmospheric retrieval refers to a broad class of techniques used to extract constraints on properties of a planetary atmosphere (e.g. composition, temperature, and clouds) from an observed spectrum. Retrieval codes start with a set of spectral observations, such as *HST* transmission spectra, and compute the range of models consistent with the data, as illustrated in Fig. 20. A retrieval model describes an atmosphere by a set of free parameters (e.g. molecular abundances and planetary radius) and uses a Bayesian sampling algorithm (typically MCMC or nested sampling) to explore the posterior distribution of the model. A retrieval typically computes $\gtrsim 10^5$ spectra to map the parameter space defining a model, with nested models then compared with identify the statistical significance of each model component (e.g. whether a given molecule is supported by the data).

5.1.2 The scope of this analysis

Extracting the most information from transmission spectra requires inference frameworks that allow us to constrain the properties of stars and planets simultaneously. In this context, the analysis presented here considers how we can best use the information we receive on both stars and planets in transit observations from space-based facilities. We focus on three areas of interest: the utility of joint stellar and planetary retrievals generally (Section 5.2); the known limitations of the approach, with a focus on the availability of suitable model spectra for stellar active regions (Section 5.3); and the complementarity of short-wavelength observations to *HST* and *JWST* NIR observations for inferring stellar photospheric properties (Section 5.4). In the following sections, we summarize the analysis that leads to our top-level findings in these three areas.

5.2 The utility of joint stellar and planetary retrievals

We first consider the general utility of employing joint stellar and planetary retrievals over other, simpler approaches. In reaching our finding, we reviewed how unocculted stellar heterogeneities modify transmission spectra, approaches for directly correcting for stellar spottedness without using retrievals, and the current state of the art for modelling stellar photospheric heterogeneity in retrievals. We also reviewed recent studies that suggest direct approaches for corrections may underestimate the actual level of stellar heterogeneity, underscoring the utility of retrievals. The following sections present each of these topics in turn.

5.2.1 Unocculted stellar heterogeneities modify transmission spectra

When a stellar surface contains heterogeneities residing outside the transit chord (i.e. unocculted spots and faculae), the transmission spectrum of a transiting planet can accrue a wavelength dependence not caused by the planetary atmosphere. The origin of this effect is a mismatch between the stellar intensity incident on the planetary atmosphere and the average intensity of the full stellar surface (see Fig. 19). The TLSE can be expressed by the following functional form:

$$D_{\lambda,\,\mathrm{obs}} = D_{\lambda,\,\mathrm{atm}}\,\epsilon_{\lambda,\,\mathrm{het}} \tag{3}$$

where $D_{\lambda,\,\mathrm{obs}}$ is the observed transmission spectrum, $D_{\lambda,\,\mathrm{atm}} = (R_{\mathrm{p},\lambda}/R_{\mathrm{s}})^2$ is the intrinsic transmission spectrum of the planetary atmosphere (i.e. the square of the wavelength-dependent planet-to-star radius ratio), and $\epsilon_{\lambda,\,\mathrm{het}}$ is the wavelength-dependent 'contamination factor' introduced by the TLSE. For a stellar surface with a single type of unocculted heterogeneity (i.e. a population of similar spots or, alternatively, faculae), the contamination factor can be written as (e.g. Rackham et al. 2018)

$$\epsilon_{\lambda,\,\mathrm{het}} = \frac{1}{1 - f_{\mathrm{het}}\left(1 - \frac{S_{\lambda,\,\mathrm{het}}(T_{*,\,\mathrm{het}})}{S_{\lambda,\,\mathrm{phot}}(T_{*,\,\mathrm{phot}})}\right)} \tag{4}$$

where f_{het} is the fractional coverage area of the heterogeneous regions, $S_{\lambda,\,\mathrm{het}}$ and $S_{\lambda,\,\mathrm{phot}}$ are the specific intensities of the heterogeneity and background photosphere, respectively, with $T_{*,\,\mathrm{het}}$ and $T_{*,\,\mathrm{phot}}$ being their corresponding temperatures. Fig. 21 shows example model spectra of $S_{\lambda,\,\mathrm{het}}$ (left-hand panel) and the contamination spectra $\epsilon_{\lambda,\,\mathrm{het}}$ (right-hand panel). We see that the contamination factor deviates from unity significantly at short wavelengths ($\lesssim 1\,\mu$m), with transit depths enhanced by unocculted spots and lowered by unocculted faculae.

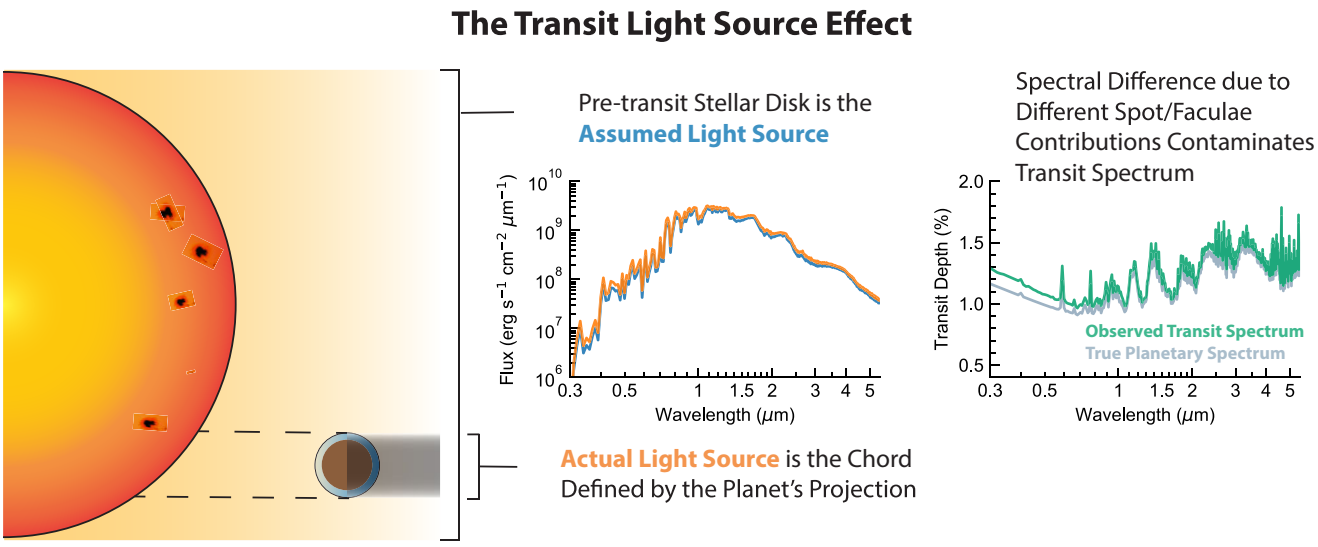

Figure 19 Illustration of the TLSE. Unocculted heterogeneities (i.e. magnetic active regions) can mask or mimic spectral features in transmission spectra by introducing a difference between the spectrum of the light source illuminating an exoplanet's atmosphere – the emergent spectrum of the transit chord – and the light source necessarily used as a reference for the transit depth measurement – the disc-averaged spectrum of the star. From Rackham et al. (2018).

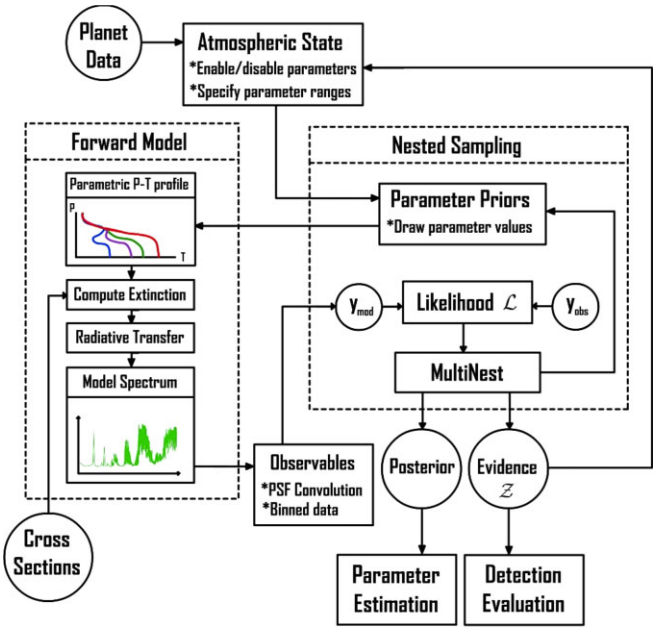

Figure 20 Schematic illustration of a retrieval framework. Retrievals start with an observed (or simulated) spectrum. A forward model is called repeatedly to compare model spectra for a wide range of atmospheric properties to the observations. A Bayesian sampling algorithm (here, nested sampling) guides the parameter space exploration, producing the posterior distribution for each parameter and detection significances for each model component (e.g. molecular species and presence of stellar heterogeneities). From MacDonald & Madhusudhan (2017).

5.2.2 Non-retrieval approaches for correcting for stellar spottedness

Without even turning to retrievals, a rich body of work exists on mitigating the impact of stellar heterogeneities on transmission spectra (see review by Bruno & Deleuil 2021). In the transmission spectroscopy literature, the primary non-retrieval approach used to account for a heterogeneous stellar photosphere is to apply a direct correction for stellar heterogeneity based on the photometric variability of the star. Modelling the stellar flux as a linear combination of the flux from the quiescent photosphere $F_{\mathrm{phot},\lambda}$ and spots $F_{\mathrm{spot},\lambda}$, which cause a total dimming of $\Delta f(\lambda_0, t)$ at a nominal wavelength λ_0, Sing et al. (2011) derive an expression for the correction required for the transit depth D_λ, given by

$$\frac{\Delta D_\lambda}{D_\lambda} = \Delta f(\lambda_0, t)\left(1 - \frac{F_{\mathrm{spot},\lambda}}{F_{\mathrm{phot},\lambda}}\right) / \left(1 - \frac{F_{\mathrm{spot},\lambda_0}}{F_{\mathrm{phot},\lambda_0}}\right). \quad (5)$$

This implies a concomitant correction to the planet-to-star radius ratio of

$$\Delta(R_{\mathrm{p},\lambda}/R_{\mathrm{s}}) \simeq \frac{1}{2}\frac{\Delta D_\lambda}{D_\lambda}(R_{\mathrm{p},\lambda}/R_{\mathrm{s}}). \quad (6)$$

Zellem et al. (2017) present a similar approach, relying on the variability of the out-of-transit stellar spectra, which are used to establish the baseline for transmission spectroscopy studies, to infer a per-visit stellar activity correction.

However, as noted by Berta et al. (2011), who derived a correction similar to that of Sing et al. (2011), this approach (whether photometric or spectroscopic) relies on the assumption that the maximum brightness in a light curve corresponds to an unspotted photosphere. This is an increasingly poorer assumption for active stars, which can have many active regions that contribute to a persistent level of spottedness as the star rotates.

These highly spotted stars are those for which corrections for stellar heterogeneity are most important to consider. McCullough et al. (2014), e.g. note that the strongly sloped transmission spectrum of HD 189733 b could be explained by spots alone (without any contribution from haze in the planetary atmosphere) if the total covering fraction of unocculted spots were 5.6 per cent, not the 1- to 1.7-per cent coverage that had been inferred through variability monitoring and previously taken into account (Pont et al. 2008, 2013; Sing et al. 2009, 2011). From this example and others, we conclude that rotational variability provides a lower limit on the heterogeneity of a stellar photosphere. Thus, applying a direct correction based on the stellar variability may underestimate the actual correction required.

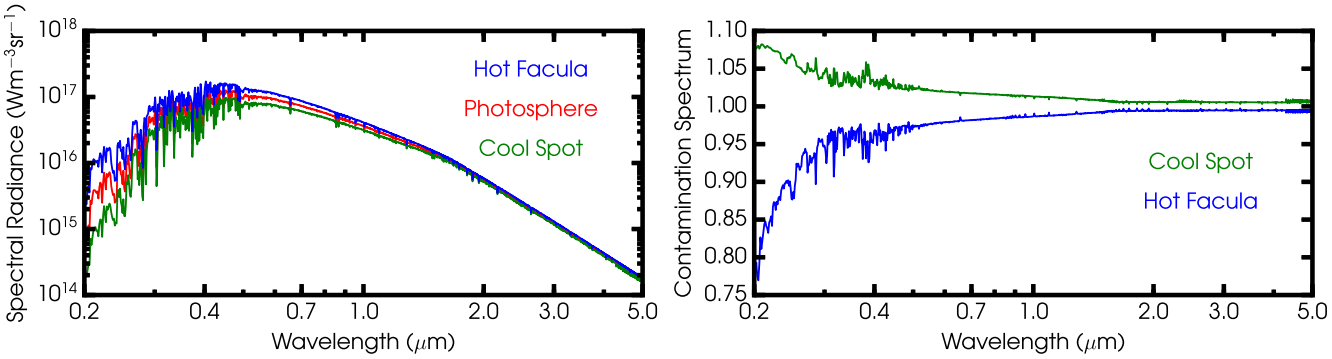

Figure 21 Stellar spectral components and their impacts on transmission spectra. The left-hand panel shows example model spectra of three primary stellar photospheric components for the case of HAT-P-1, assuming $T_{\rm phot} = 5980$ K and adding (subtracting) 300 K for the hot facula (cool spot) spectrum.. The right-hand panel illustrates the multiplicative change in transit depth introduced by unocculted spots and faculae, assuming a 10-per cent coverage fraction. From Pinhas et al. (2018).

5.2.3 Including stellar heterogeneities in retrievals

By constraining the impact of stellar contamination directly from transmission spectra, retrievals can identify photospheric heterogeneity that is not evident in variability monitoring. These analyses can fit simultaneously for the properties of the planetary atmosphere and any heterogeneities and appropriately marginalize over the contamination signal while estimating planetary parameters. Retrieval codes typically accomplish this by adding three additional free parameters encoding the heterogeneous regions (e.g. Pinhas et al. 2018; Rathcke et al. 2021): $f_{\rm het}$, $T_{*,\,\rm het}$, and $T_{*,\,\rm phot}$. During parameter space exploration, each pair of $T_{*,\,\rm het}$ and $T_{*,\,\rm phot}$ are used to compute spectra of the heterogeneity and the photosphere by interpolating grids of stellar models, e.g. the PHOENIX (Husser et al. 2013) or Castelli-Kurucz grids (Castelli & Kurucz 2003). Given the interpolated stellar spectra and $f_{\rm het}$, the contamination factor is computed using equation (4) and combined with the atmospheric spectrum as in equation (3). The combined transmission spectrum is then compared with the observations at each point in the parameter space.

We provide an example retrieval analysis in Fig. 22. We generated a simulated transmission spectrum of a hot Jupiter (with planet properties based on HD 209458b) transiting a star with unocculted spots. For this example, we assumed 5-per cent spot coverage with a spot temperature 900-K colder than the photosphere. The unocculted spots produce a steep slope at visible wavelengths and secondary features imprinted by stellar absorption. The simulated data cover 0.34–1.80 μm, roughly corresponding to the range of *HST*/STIS+WFC3, at a precision of 30 ppm. We subjected this data set to two retrievals with the POSEIDON code (MacDonald & Madhusudhan 2017) under different assumptions: (i) unocculted spots are included within the retrieval; and (ii) no spots are considered, only the planetary atmosphere shapes the spectrum. We find that the atmosphere-only retrieval attempts to account for the lack of spots by adding a haze (producing a similar optical slope) and a cloud deck. While both models result in an acceptable fit, the atmospheric properties are significantly biased when unocculted spots are not considered: The Na and K abundances are biased by $\sim 5\sigma$, the H_2O abundance is biased by $\sim 3\sigma$, and one would incorrectly conclude that the atmosphere has potent aerosols. Conversely, the retrieval including unocculted spots correctly recovers all input parameters within the 1–2 σ expected from Gaussian scatter. The Bayesian evidence also prefers the model including spots ($\Delta \ln Z = 11.6$), showing that a retrieval code can differentiate between these scenarios. This exercise demonstrates that biases in atmospheric properties can be mitigated by including stellar heterogeneities in retrievals.

The confidence with which unocculted stellar spots or faculae can be identified is a function of spectral precision, coverage fraction, and wavelength range. Using simulated *JWST*/NIRISS data and Bayesian model comparisons, Iyer & Line (2020) show how the level of preference for stellar contamination varies with these factors for typical sub-Neptunes orbiting M-dwarfs. For large covering fractions of unocculted spots (above 1 per cent, see Fig. 23), the Bayes factor increasingly favours a model including the proper TLSE correction across spectrophotometric precisions from 15 to 120 ppm. For small spot covering fractions (below 1 per cent), the TLSE signal is evident in high-fidelity *JWST*/NIRISS data (∼15 ppm precision). However, it may be harder to identify stellar contamination for small spot coverage at more typical precisions ($\gtrsim$30 ppm). Iyer & Line (2020) draw consistent conclusions for including the TLSE in retrievals – in their case, for *JWST*/NIRISS data of sub-Neptunes transiting M-dwarfs – compared with those we draw from the analysis of simulated *HST*/STIS+WFC3 data of a hot Jupiter transiting a G dwarf in Fig. 22. Notwithstanding these analyses, there is considerable scope for future work to further quantify when the inclusion of stellar contamination within a retrieval framework is necessary, e.g. considering the sensitivity of such inferences to other instruments with different precisions, wavelength coverage, and spectral resolutions.

The inclusion of unocculted stellar heterogeneities within retrievals is a relatively new addition to the literature. Consequently, approaches can vary between different studies and a 'best practice' consensus has yet to emerge. Four of the main differences are as follows:

(i) **Free parameters**: A single heterogeneity can be described by three free parameters ($f_{\rm het}$, $T_{*,\,\rm het}$, and $T_{*,\,\rm phot}$; see Pinhas et al. 2018), or a subset can be fixed (e.g. Bruno & Deleuil 2021). Additional parameters could be added for multiple heterogeneities when such models (e.g. including both spots and faculae; Zhang et al. 2018) are necessary is unclear and worthy of future study.

(ii) **Out-of-transit stellar spectra**: Recent studies have leveraged baseline, out-of-transit stellar spectra in real and simulated data sets to fit for stellar heterogeneity parameters, either while simultaneously modelling their impact on transmission spectra or simply gathering prior information for analyses of transmission spectra (Zhang et al. 2018; Wakeford et al. 2019; Iyer & Line 2020; Cracchiolo, Micela

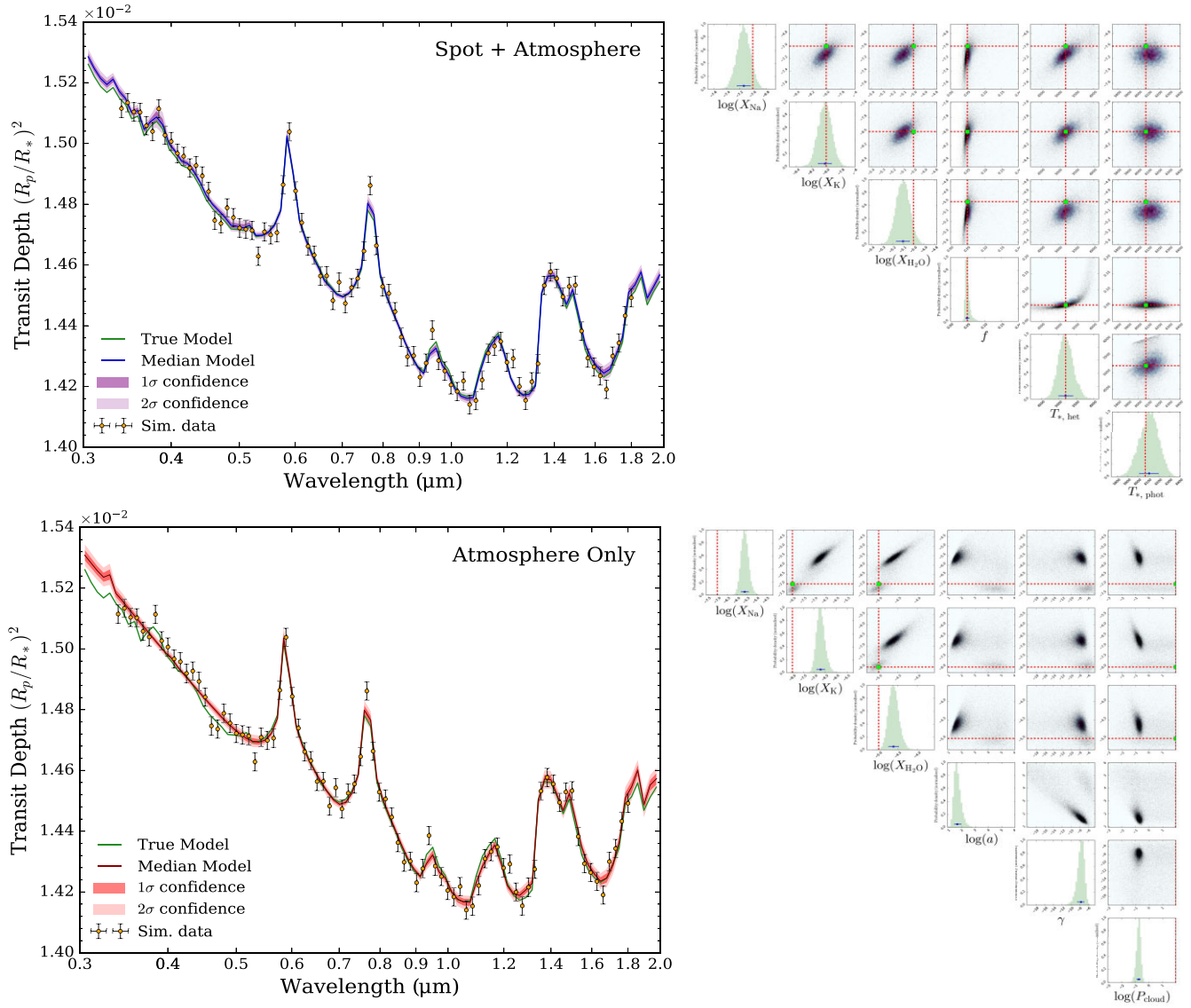

Figure 22 The impact of unocculted spots in a retrieval analysis. A simulated hot Jupiter transmission spectrum contaminated by unocculted spots (orange data) is subjected to two retrievals: (i) simultaneous modelling of the planetary atmosphere and unocculted spots (top panels); and (ii) the planetary atmosphere only (bottom panels). The posterior distributions (right-hand panels) compare the true planetary atmosphere and stellar properties (red dashed lines) to the 1 σ confidence regions for each parameter (blue error bars). The model without spots attempts to compensate by adding a haze slope and a cloud deck, resulting in a similar fit but significantly biased ($\gtrsim 3\sigma$) composition inferences. The model including unocculted spots within the retrieval achieves a better fit to the data and successfully recovers the input planetary atmosphere and stellar properties.

& Peres 2021). It is unclear whether this approach provides an additional advantage over analyses of transmission spectra alone.

(iii) **Priors**: Some studies ascribe Gaussian priors to $T_{*,\,\mathrm{phot}}$ (e.g. Pinhas et al. 2018; Rathcke et al. 2021), encoding a priori knowledge on the stellar T_{eff}, while others use uniform priors (e.g. Iyer & Line 2020).

(iv) **Stellar grids**: Many model stellar grids are available, with different grids implemented in different retrieval codes. We consider the impact of this further in Section 5.3.

Alongside these differences, other common assumptions include: fixing the metallicity and surface gravity of any heterogeneities to those of the photosphere (both set to a priori values) and, as noted previously, the consideration of only one heterogeneity. The variety of approaches in the literature to date serves to illustrate that more work on retrievals including stellar heterogeneities will be beneficial.

5.2.4 *Existing spectra are impacted*

Recent studies employing retrievals have found mounting evidence for unocculted heterogeneities impacting transmission spectra, in many cases at a level beyond what was previously inferred via variability measurements. Pinhas et al. (2018) reanalysed nine hot Jupiter transmission spectra from *HST* and *Spitzer* (Sing et al. 2016), finding moderate evidence (3.1σ) for stellar heterogeneity in the spectrum of WASP-6b, beyond that previously estimated to be present from variability measurements (Jordán et al. 2013; Nikolov et al. 2015). Another three hot Jupiters show moderate to weak suggestions of stellar heterogeneity: WASP-39b (2.5σ), HD 209458b

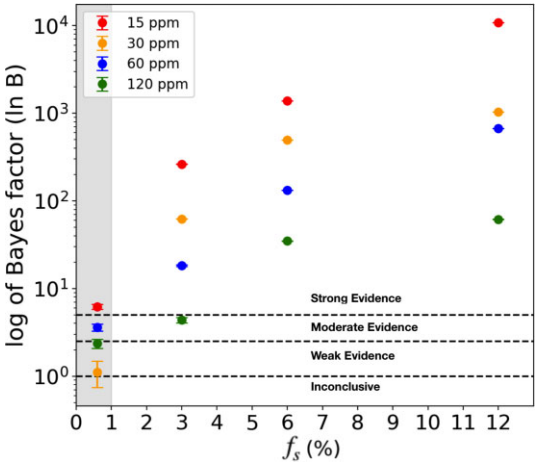

Figure 23 The statistical preference for including the TLSE in retrievals of synthetic *JWST*/NIRISS data as a function of spot covering fraction. In this exercise, Iyer & Line (2020) performed retrievals on the transmission spectrum of a sub-Neptune orbiting an M-dwarf with unocculted spots, varying the data precision from 15 to 120 ppm (point colours) and the spot covering fractions from 0.6 per cent to 12 per cent. The black dashed lines indicate the degree of statistical preference for the TLSE-correction-included retrieval model (Trotta 2008). The overall trend is that the model including the TLSE is increasingly preferred for better precision and for spot covering fractions above 1 per cent. Below 1- per cent spot coverage, the biases from ignoring the correction are not as noteworthy (except for 15-ppm precision, where the TLSE model is still strongly preferred). Such small spot coverage (a low evidence regime) also incurs inaccuracies in computing Bayes factors, causing the crossing over of the 30-ppm point (e.g. Lupu et al. 2014). From Iyer & Line (2020).

(1.6σ), and HAT-P-12b (1.4σ). Rathcke et al. (2021) studied the optical and NIR transmission spectrum of the hot Jupiter WASP-79b and inferred the presence of unocculted faculae (4.7σ) covering ∼15 per cent of the disc of the F5V host star with a temperature contrast of ∼500 K. Similarly, Kirk et al. (2021) studied the optical and NIR transmission spectrum of the ultrahot Jupiter WASP-103b, notably using 11 optical transits that paint a consistent picture between epochs and across four instruments. From this spectrum, which shows a marked decrease in transit depth at blue-optical wavelengths, they inferred the presence of unocculted faculae (4.1σ) covering ∼20 per cent of the stellar disc with a temperature contrast of ∼400 K. In these examples, the impact of stellar heterogeneity on the transmission spectra was either underestimated in previous studies applying direct corrections or may have been missed if not for the use of retrievals, which points to the utility of this approach for identifying and disentangling signals from stellar heterogeneity and planetary atmospheres in transmission spectra.

5.2.5 Our finding: Finding 4.1

From this analysis, we draw the following findings:

Summary

Retrievals of transmission spectra that include the effects of unocculted active regions can guard against biases. More work is needed to understand when these retrievals are necessary and what are the limitations and best practices of this approach.

Capability needed

A detailed understanding is needed of when to marginalize over stellar heterogeneity in retrievals of planetary atmospheric parameters and the best practices for doing so. A benchmarking of the available retrieval tools is also needed.

Capability today

Multiple groups have developed retrievals that use simple parametrizations of unocculted heterogeneities and rely on 1D stellar models for spectra of both the quiescent photosphere and active regions (e.g. Rackham et al. 2017; Pinhas et al. 2018; Zhang et al. 2018, 2019; MacDonald 2023).

Mitigation in progress

Retrieval frameworks that marginalize over stellar heterogeneity are commonly used in modern analyses of transmission spectra (e.g. Espinoza et al. 2019; Kirk et al. 2021; Rathcke et al. 2021). Applications to simulated *JWST* data show that marginalizing over potential stellar impacts is useful for avoiding biases in retrieved planetary properties introduced by photospheric heterogeneity (Iyer & Line 2020). Ongoing work is focused on applying these frameworks to *JWST* transmission spectra to understand the best practices when working with these precise observations (Rackham et al. 2023).

5.3 Limitations of the approach

We next consider the known limitations of the retrieval approach, focusing on the availability of suitable model spectra for stellar magnetic active regions. In reaching our finding, we considered the disagreement among current model stellar spectra and the related impact of employing different stellar spectra on retrieved planetary properties as well as recent advances in modelling spectra of stellar magnetic active regions.

5.3.1 Disagreement among model stellar spectra and its impact on retrievals

A primary limitation of retrieval approaches for handling stellar contamination is their reliance on stellar models, which vary substantially in their predictions of the spectra of cool stars. Substantial variations in spectral shape among widely used stellar models (Fig. 24, left-hand panel) owe to a variety of factors, including the choice of opacity data included and spectral line list completeness; treatment of line-broadening effects; and physical assumptions, such as plane-parallel versus spherical geometry and local thermodynamic equilibrium (LTE) versus non-LTE chemistry conditions. The variation is more pronounced for mid-to-late M stars ($T_{\rm eff}$ < 3500 K) than for FGK stars due to molecular opacities dominating such atmospheres and photospheric surface heterogeneities that are common in active cool stars (Hawley & Pettersen 1991; Hawley et al. 2014; Schmidt et al. 2014). As a result, the choice of stellar models used while correcting for TLSE signals can impact planetary properties retrieved from transmission spectra.

This impact has been explored quantitatively in a recent study by Iyer & Line (2020, Fig. 25). These authors used the PHOENIX-ACES model grid (Husser et al. 2013) to mimic a 'true' disc-integrated stellar spectrum of an M dwarf ($T_{\rm phot}$ = 3300 K) contaminated by unocculted spots ($T_{\rm s}$ = 2838 K) covering a fractional area $f_{\rm s}$ of 12 per cent. They performed a retrieval on a simulated transmission spectrum with this contamination, using the PHOENIX model grid (Allard et al. 2003) to calculate the TLSE contribution to the transmission spectrum. They find the fit reasonably explains the shape of the transmission spectrum. However, the induced variations in the best-fitting spectrum are probably due to false opacity signatures or incorrect estimates of the thermal profile – evident in the form of bias in the posterior probability distributions of the planetary

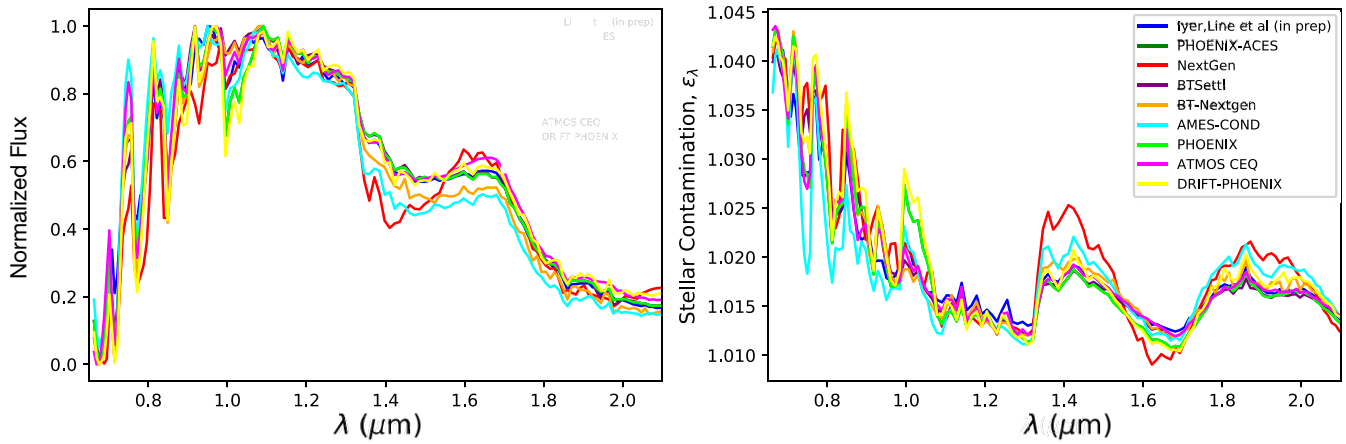

Figure 24 Disagreements among model stellar spectra and their resulting contamination factors. Left-hand panel: Spectra from popular stellar model grids of an M dwarf with $T_{\rm eff} = 3000$ K, $\log g = 5.0$, and [Fe/H] $= 0.0$. Right-hand panel: The stellar contamination factor that influences planetary spectra via the TLSE (equation 4) constructed from these stellar models, assuming a fractional coverage of unocculted spots on the photosphere of $f_{\rm s} = 5$ per cent and a spot temperature of $T_{\rm s} = 2700$ K. Adapted from Iyer et al. (2023).

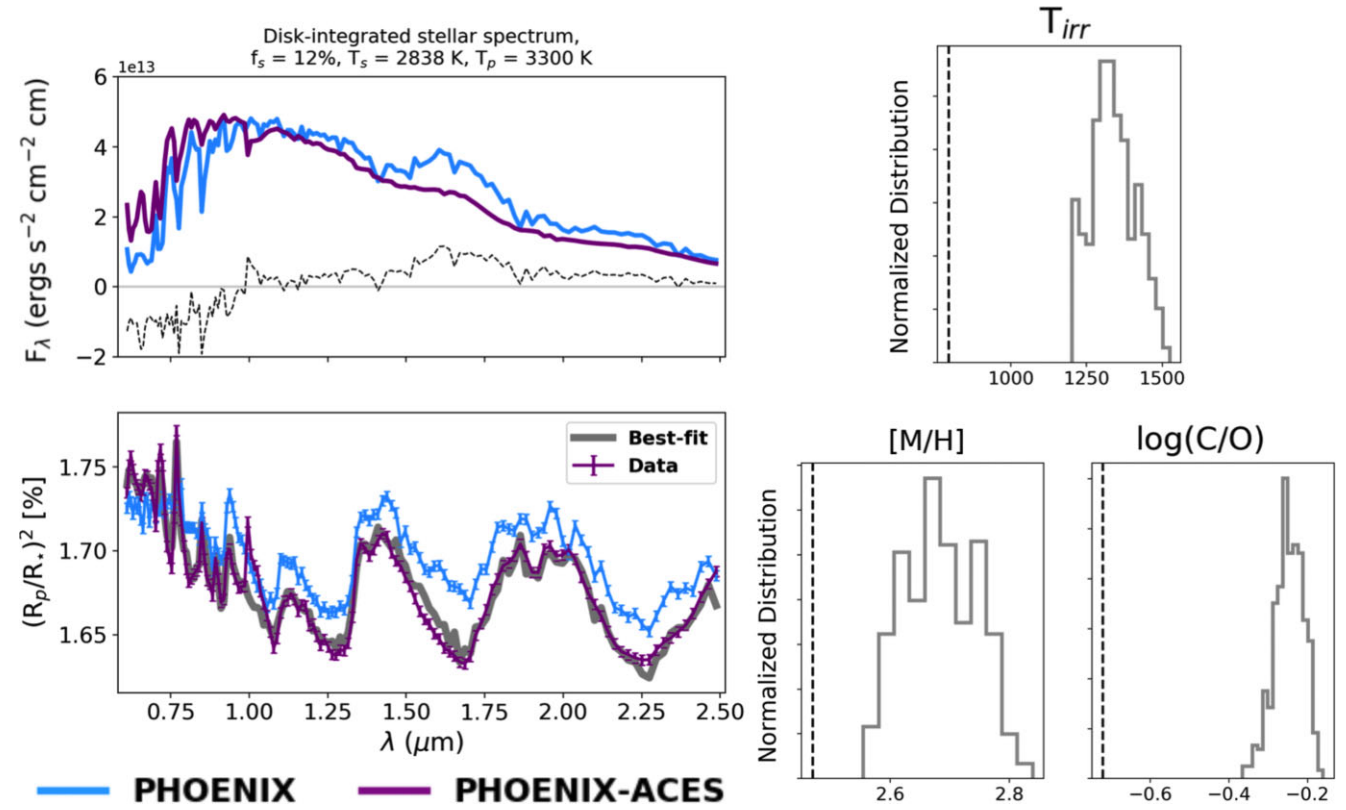

Figure 25 The impact of disagreements between stellar models on retrievals. Here, Iyer & Line (2020) simulated a data set contaminated by unocculted spots using the PHOENIX-ACES model grid (Husser et al. 2013) but retrieved it using the PHOENIX model grid (Allard et al. 2003). They find significant biases in the retrieved values of the atmospheric irradiation temperature $T_{\rm irr}$, metallicity [M/H], and carbon-to-oxygen ratio log (C/O). Top-left panel: Disc-integrated stellar spectra from both model grids and their residuals. Bottom-left panel: contaminated transmission spectra in both cases and the retrieved spectrum. Right-hand panel: Posterior distributions of the atmospheric parameters compared with the true model inputs (dashed lines). From Iyer & Line (2020).

irradiation temperature $T_{\rm irr}$, metallicity [M/H], and carbon-to-oxygen ratio log (C/O) (Fig. 25, right-hand panel). This exercise highlights that, despite an appropriate implementation of the TLSE, our ability to correct for the contribution of stellar contamination heavily depends on the accuracy of the stellar models used to represent the contaminated stellar photosphere – particularly for cooler host stars (K- and M-type) – thereby emphasizing the need for improved stellar atmosphere models.

5.3.2 Advances in modelling spectra of active regions

Facular and sunspot contrasts employed by retrieval models are typically derived from 1D, plane-parallel, semi-empirical model atmospheres (e.g. Vernazza, Avrett & Loeser 1981; Kurucz 1992a, b, c; Fontenla et al. 1993, 1999, 2006; Fontenla, Avrett & Loeser 2002). For faculae in particular, such models are adjusted to agree with solar observations (Vernazza et al. 1981). However, for stars other than the Sun, such observations are not available, and thus adjustment of the models is not possible. Furthermore, while such semi-empirical models capture the overall disc-integrated properties of faculae reasonably well, they do not recover the observed CLV of the facular contrast (e.g. Yeo et al. 2013).

More realistic CLV of facular contrasts is provided by 3D MHD simulations, as discussed in Section 2. The first 3D radiative HD simulations for stars were reported by Nordlund & Dravins (1990). The magnetic field was introduced in such simulations more recently, and by now a series of models for stars of spectral types F to M with different mean vertical magnetic fields is available (Beeck et al. 2011, 2015a; Beeck 2014; Wedemeyer et al. 2013; Steiner et al. 2014; Salhab et al. 2018). Norris et al. (2017) and Johnson et al. (2021) used the 3D MURaM atmospheres from Beeck et al. (2015a) to calculate the CLV of the facular contrast for G2 (see Fig. 26), K0, M0, and M2 stars with the mean vertical magnetic field ranging between 100 and 500 G. Norris et al. (2017) found the computed CLV profiles of a G2 star to be in good agreement with solar observations (Neckel & Labs 1994). More recently, simulations by Johnson et al. (2021) have clearly demonstrated a strong effect of faculae on the mean brightness and shape of stellar light curves, pointing to the need for more accurate facular models. Using a self-consistent approach and 1D model atmospheres, Witzke et al. (2018) have additionally shown that facular contrast increases with stellar metallicity, underscoring the importance of accurate fundamental stellar parameters when modelling stellar magnetic activity.

In the case of spots, 3D MHD simulations using the MURaM code have been largely successful in reproducing the fundamental observed features of spots, both on the Sun and other stars. Rempel et al. (2009a, b) have produced MURaM simulations of sunspots and found good agreement with observations. Recently, Panja et al. (2020) have used the MURaM code to perform the first ab initio simulations of spots on cool main-sequence stars other than the Sun. Their simulations for G2V, K0V, and M0V stars provide umbral and penumbral effective temperatures for these stars, along with other fundamental parameters of starspots, such as the brightness relative to the stellar surface and magnetic field strength. They conclude that the trend of increasing temperature difference with photospheric temperature that they observe is consistent with observations of starspots.

Taken together, these studies highlight recent advances in modelling spectra of magnetic active regions and underscore the existing limitations. While 1D models, such as those used to derive template spectra for state-of-the-art retrievals of transmission spectra, generally reproduce well the observed features of spots, they fail to capture aspects of facular contrasts that can impact transit observations. In particular, the CLV of the facular contrast and the dependence of facular contrast on stellar metallicity are important in this context but not addressed in modern retrievals. Recent work with 3D MHD simulations can be leveraged to improve template spectra for spots and faculae, though the output of these realistic stellar models has yet to be incorporated into exoplanetary retrieval analyses.

5.3.3 Our finding: Finding 4.2

From this analysis, we draw the following findings:

Summary

Retrieval approaches rely on stellar models, and thus their accuracy is limited by model fidelity and, depending on the approach, the prior information on stellar parameters used in the retrieval. Further efforts to develop model spectra for spots and faculae and incorporate them into exoplanetary atmospheric retrievals are needed.

Capability needed

More work is needed to (i) further test and develop models for cool stars, (ii) assess the impact of using stellar spectra to approximate active regions, and (iii) develop model spectra for active regions, particularly faculae, for different spectral types. Studies should also investigate the impact of simple parametrizations that neglect the viewing-angle dependence of spot and facula spectra.

Capability today

Retrieval analyses today rely on stellar spectra derived from 1D models (e.g. Husser et al. 2013) as templates for spot and facula spectra. Recent retrieval frameworks incorporate the option using multiple stellar model grids for generating component spectra (e.g. quiescent photosphere, spots, and faculae; MacDonald 2023). Simple parametrizations of signals introduced by unocculted heterogeneities do not incorporate any viewing-angle dependence of spot and facula spectra (e.g. Rackham et al. 2017).

Mitigation in progress

Recent studies have produced ab initio spot and facula spectra from 3D MHD models for a few FGKM spectral types (Norris et al. 2017; Panja et al. 2020). These studies reveal spectral differences with respect to spectra from 1D stellar spectral models that underscore the limitation of this approach, particularly for faculae (Witzke et al. 2022).

5.4 The complementarity of short-wavelength observations

The third and final general aspect we considered is the complementarity of short-wavelength observations to *HST* and *JWST* NIR observations for inferring stellar photospheric properties. In reaching our finding, we considered forward-modelling efforts that suggest the impacts of heterogeneous stellar photospheres are largest at UV and blue-optical wavelengths and recent studies that either point to stellar contamination in short-wavelength transit data or increase the model preference for a heterogeneous stellar photosphere by including optical data.

5.4.1 Projected impacts are strongest at short wavelengths

Many studies in the past decade have considered the impact of unocculted active regions on transit observations. Usually, these studies focus on interpretations of transmission spectra from individual systems with active host stars, such as HD 189733 (Pont et al. 2008, 2013; Sing et al. 2009, 2011; McCullough et al. 2014; Oshagh et al. 2014), WASP-6 (Jordán et al. 2013; Nikolov et al. 2015), and GJ 1214 (Berta et al. 2011, 2012; Rackham et al. 2017). Despite the different spectral types and activity levels of these host stars, studies of individual targets like these consistently find that the projected impacts of unocculted active regions are most evident at blue-optical and shorter wavelengths, where the contrasts between active regions (whether spots or faculae) and the quiescent photosphere are greatest.

This finding is borne out as well by studies of unocculted active regions for less-active stars, like the Sun. Llama & Shkolnik (2015) studied the impact of solar-like photospheric heterogeneity on transits

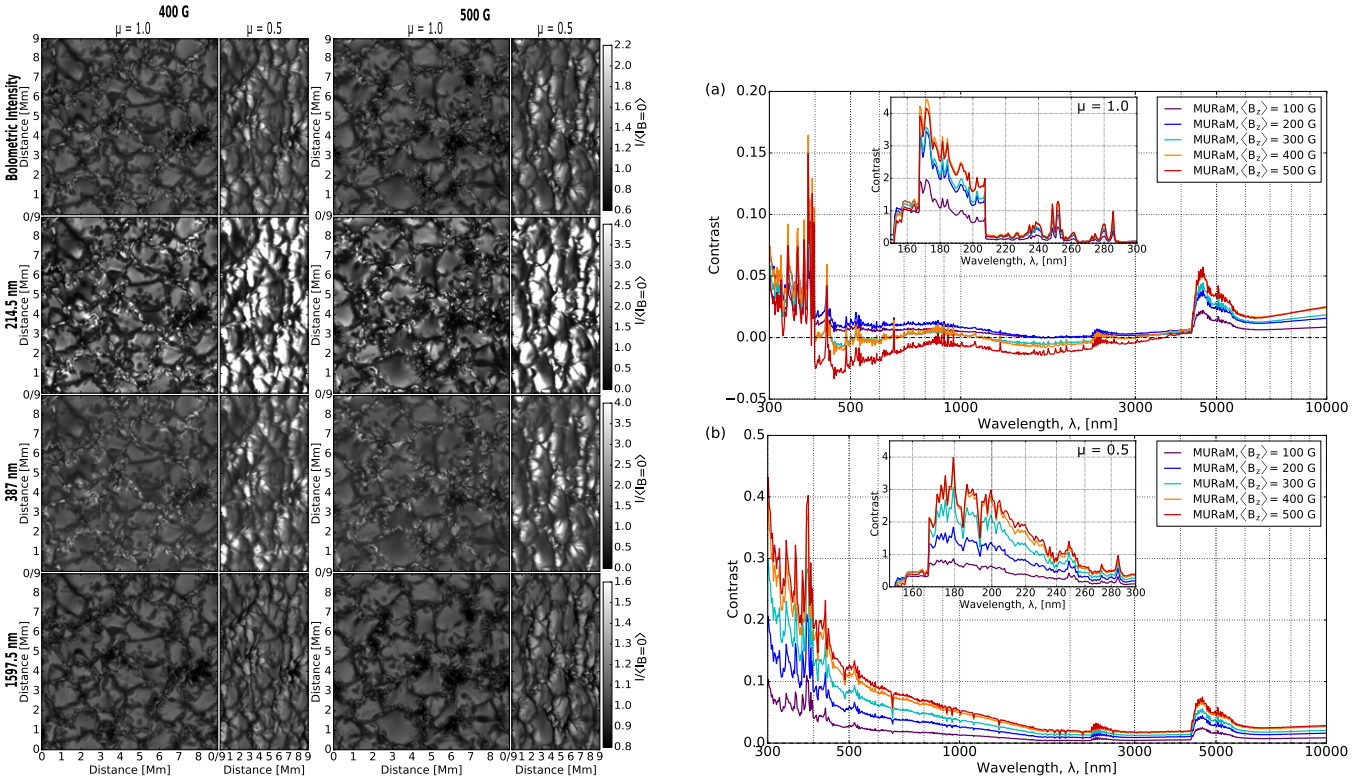

Figure 26 Simulations of faculae with the 3D radiation-MHD code MURaM (Vögler et al. 2005) and their derived contrast spectra. Left-hand panel: Normalized emergent intensities from a simulated G2 atmosphere at different viewing angles, wavelengths, and for two average magnetic field strengths (400 and 500 G). Faculae have markedly higher contrasts near the limb and at shorter wavelengths. Right-hand panel: Average facular contrast spectra for G2 simulated atmospheres with differing field strengths, both at disc centre (top right) and nearer to the limb (bottom right). The spectra show different structures than what are currently captured by approximations of facular spectra with disc-integrated stellar spectra. The CLVs shown here are also not captured by current approximations of faculae in retrievals. From Norris et al. (2017).

by injecting a hot Jupiter transit into resolved observations of Solar Cycle 24 from NASA's SDO. While they recovered accurate planetary radii in the optical (4500 Å), they found that solar-like unocculted active regions biased their recovered R_p/R_s values in ∼20 per cent of their simulated soft X-ray (94 Å) and UV (131–1700 Å) light curves. At these wavelengths, unocculted active regions generally led to a mean underestimate of 10 per cent of the planetary radius, with up to 25 per cent underestimates occurring during high-activity periods In the FUV (1600 and 1700 Å) simulations, the mean recovered value of R_p/R_s was overestimated by ∼20 per cent. Similarly, in simulated Ly α transits (Llama & Shkolnik 2016), recovered values of R_p/R_s are biased by up to 50 per cent in 25 per cent of the simulated light curves.

Turning to stars other than the Sun, Rackham et al. (2018, 2019) estimated the impact of unocculted active regions for FGKM stars with typical activity levels. Using a suite of Monte Carlo simulations, they estimated the spot and facula covering fractions that correspond to the observed variabilities of FGKM dwarfs by spectral type. They found that spot covering fractions, in particular, increase from ∼0.1 per cent for F dwarfs to 2–4 per cent for late-K dwarfs to ∼10 per cent for M dwarfs. If present on the unocculted stellar disc, spots and faculae alter transit depths in the 0.3- to 5.5-μm wavelength range by a few to tens of per cent, depending on assumptions about spot size and spot-to-facula areal ratio (Fig. 27). Along with the other studies summarized here, these studies of exoplanet host stars with typical activity levels agree that impacts should be most evident at blue-optical and UV wavelengths.

For this reason, the need to observe at short wavelengths is a key motivating factor in the design of upcoming transit-focused space missions. The Ariel Space Mission, a medium-class ESA mission planned for launch in 2029, will survey a diverse sample of roughly 1 000 exoplanets during its 4-yr mission. Its design includes a 1-m-class elliptical (1.1 × 0.7 m) primary mirror and enables simultaneous visible and NIR observations spanning 0.5–7.8 μm. The choice of the short wavelength limit of the Ariel bandpass was driven precisely by the need to correct for stellar activity (Tinetti et al. 2021). Likewise, Pandora is a NASA Pioneers Mission, planned for launch in the mid-2020s, with the goal of disentangling stellar and planetary signals in transmission spectra and reliably determining the compositions of exoplanet atmospheres. Pandora will study transits of at least 20 planets hosted by K and M dwarfs during its 1-yr primary mission. Its design includes a 0.45-m primary mirror and, like Ariel, it will also observe simultaneously in the visible and NIR (∼0.4–1.6 μm) with a visible photometric channel and a low-resolution ($R \geq$ 30) NIR (1.0–1.6 μm) spectroscopic channel (Quintana et al. 2021).

5.4.2 *Short-wavelength observations reveal stellar contamination*

Many existing exoplanet transmission spectra are assembled piecewise via observations with various instruments covering different wavelength ranges (e.g. *HST*/STIS, *HST*/WFC3, and *Spitzer*/IRAC; Sing et al. 2016). Consequently, the atmospheric interpretations inferred from a given planet's spectrum can change over time as the spectral wavelength range becomes more complete. Given that

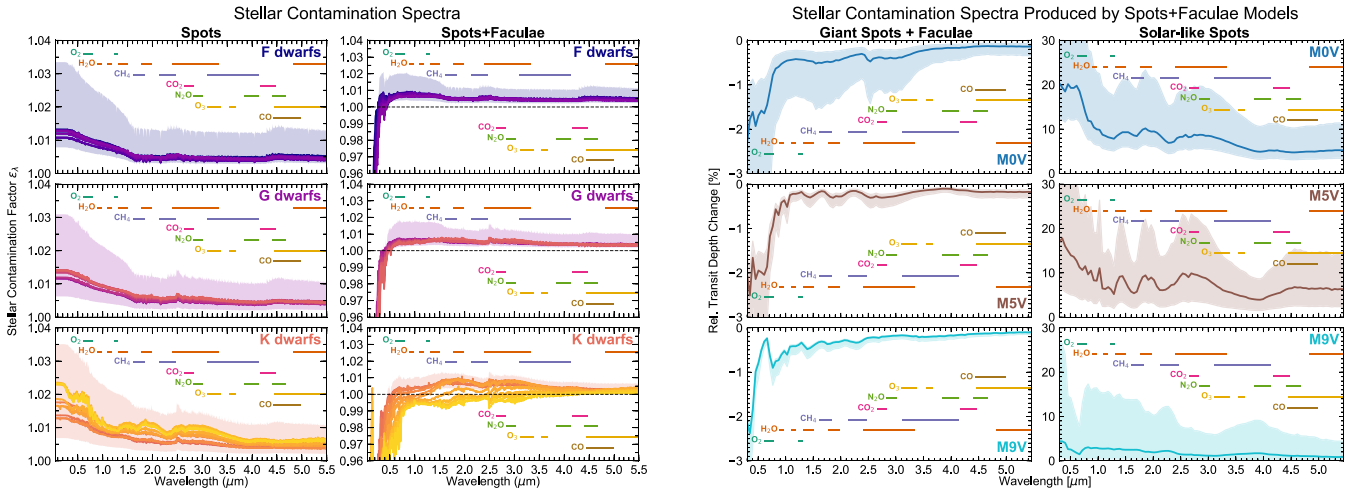

Figure 27 Estimated contamination spectra due to spots and faculae on FGKM dwarfs. Using spot and facula covering fractions inferred from rotational variabilities, forward modelling suggests that typical impacts of stellar contamination will be larger for cooler stars, though considerable uncertainty exists as to the relative impacts of spots and faculae. In any case, spectral contamination due to stellar photospheric heterogeneity is predicted to be largest at short wavelengths (<0.6 μm). From left to right, the columns show the spectral contamination from unocculted spots on FGK dwarfs, spots and faculae on FGK dwarfs, spots and faculae on M dwarfs, and spots on M dwarfs. From Rackham et al. (2018, 2019).

the impact of unocculted stellar heterogeneities is most pronounced at short wavelengths, one may anticipate that initial atmospheric reconnaissance using only IR observations can miss signatures of stellar contamination. Here, we focus on one recent case study demonstrating the utility of short-wavelength transmission spectra to reveal unocculted stellar heterogeneities.

The hot Jupiter WASP-79b (Smalley et al. 2012) has been considered a strong candidate for the *JWST* Early Release Science program (Bean et al. 2018). Sotzen et al. (2020) presented initial observations of WASP-79b obtained with *HST*/WFC3, *Spitzer*/IRAC, *TESS*, and *Magellan*/LDSS3. They inferred the presence of H_2O absorption from the IR observations and attributed a blue downward slope from the ground-based LDSS3 data to FeH. An independent analysis by Skaf et al. (2020), using only *HST*/WFC3 data, reached similar conclusions. However, neither of these studies considered unocculted stellar heterogeneities in their retrievals. Recently, Rathcke et al. (2021) presented additional *HST*/STIS observations of WASP-79b, which extended the transmission spectrum down to 0.3 μm and confirmed the lower transit depths at short wavelengths suggested by LDSS3 (see Fig. 28). Their retrieval analysis identified a strong preference for unocculted faculae (4.7σ), covering ∼15 per cent of the stellar disc with a temperature contrast of ∼500 K, but without the need for FeH. This provides another demonstration that, in the presence of informative data, atmospheric interpretations can be biased if stellar contamination is not considered (see Section 5.2.3).

Since *JWST* observations will be confined to wavelengths longer than 0.6 μm, we assessed the information content provided by optical transmission spectra in the context of WASP-79b. Fig. 28 shows how the inferred stellar properties alter when only the IR (> 1.0 μm) observations are considered. We see that the retrieval does not identify unocculted faculae when the optical data is omitted ($T_{*,\,\mathrm{het}}$ is consistent with $T_{*,\,\mathrm{phot}}$ and f_{het} is consistent with 0). This suggests that complementary blue-UV observations, at shorter wavelengths than *JWST* can observe, may aid the identification of unocculted stellar heterogeneities. However, additional work would be beneficial to explore whether the conclusions from this case study apply more broadly.

5.4.3 Combining visible and NIR spectra improves physical inferences

The inclusion of visible wavelength observations provides an additional quantitative benefit: better inferences for both the planetary atmospheric properties and any unocculted stellar heterogeneities. Kirk et al. (2021) recently demonstrated this with a retrieval analysis of the ultrahot Jupiter WASP-103b. Similar to the case of WASP-79b, they found the transit depth of WASP-103b to decrease towards blue wavelengths (Fig. 29). They showed that retrievals including only IR *HST* and *Spitzer* observations can infer unocculted faculae (2.4σ) from a slope in the WFC3 observations, but the addition of precise ground-based observations helps confirm this inference (4.3σ). At the same time, the detection significance of the planetary atmosphere increased marginally from 1.9σ to 2.8σ. This provides a quantitative example of how short-wavelength observations can increase our confidence in a given interpretation of an exoplanet's transmission spectrum.

5.4.4 Our finding: Finding 4.3

From this analysis, we draw the following findings:

Summary

For low-resolution transmission spectra, the impact of unocculted active regions is larger at shorter wavelengths. More work is needed to quantify the complementary nature of such spectra for *JWST* observations.

Capability needed

A detailed understanding is needed of when short-wavelength data are necessary to complement NIR transmission spectra from *HST* and *JWST*. Studies should address the impact of short-wavelength data on retrievals as a function of the stellar spectral type and activity level and the scale of planetary atmospheric features. Similarly, an understanding is needed of what biases may be introduced by studying NIR spectra alone – even in the context of joint stellar and planetary retrievals.

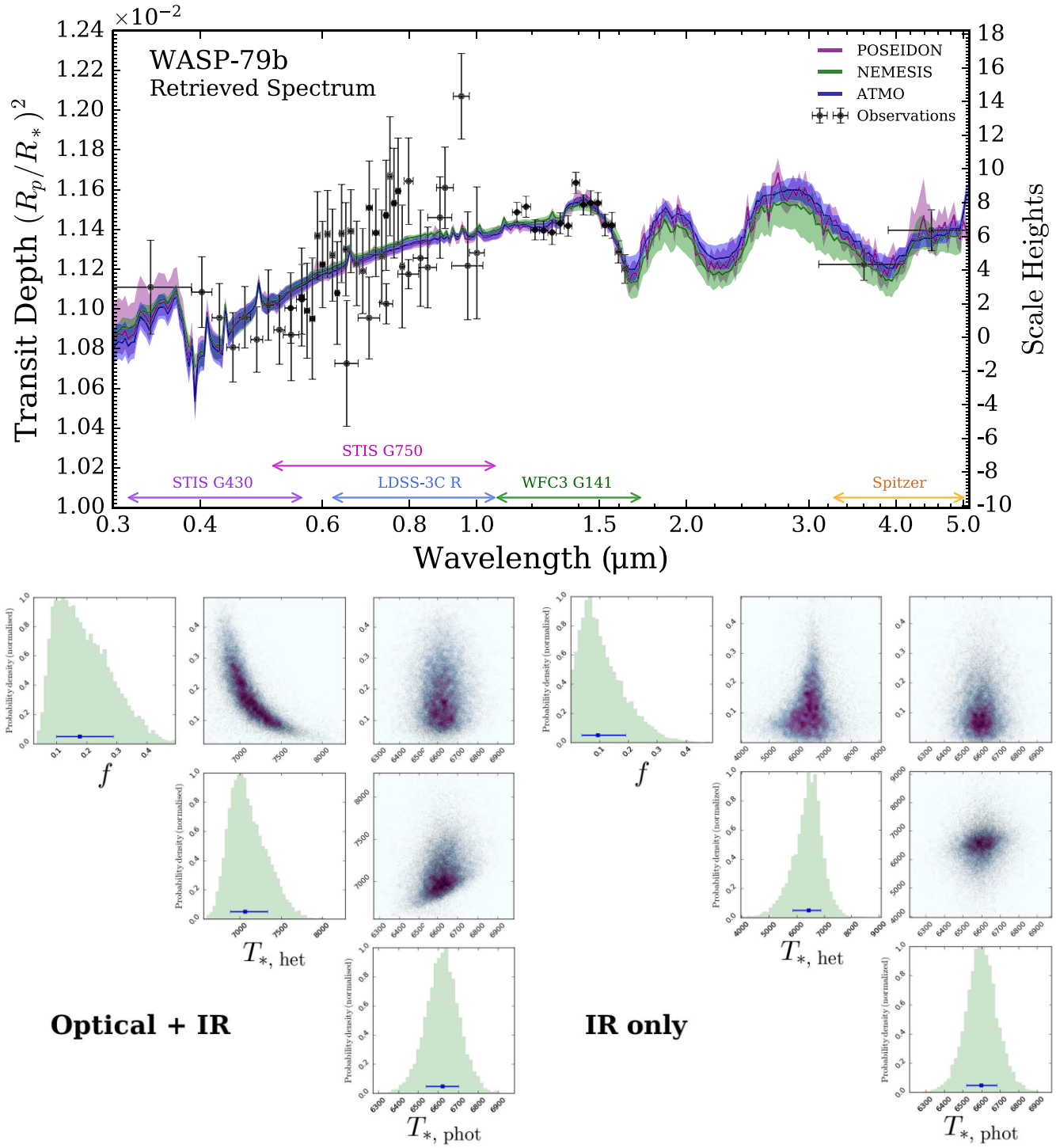

Figure 28 Top panel: The optical and NIR transmission spectrum of the hot Jupiter WASP-79b. The decreasing transit depth towards blue wavelengths is a characteristic signature of unocculted faculae (detected at 4.7σ). Three distinct retrieval codes independently inferred the necessity of faculae to explain WASP-79b's transmission spectrum, demonstrating the robustness of this interpretation. Bottom panel: Retrieved stellar heterogeneity parameters from the full optical + NIR data set (left-hand panel) and from the NIR data alone (right-hand panel). The identification of faculae for WASP-79b crucially hinges on data at wavelengths < 1.0 μm. From Rathcke et al. (2021).

Capability today

Simulated observations of a hot Jupiter transiting the Sun show that Sun-like activity can bias R_p/R_s measurements by ∼20 per cent in soft X-ray, extreme ultraviolet (EUV), and far ultraviolet (FUV) observations (Llama & Shkolnik 2015). Other simulations show that typical coverages of spots and faculae on K and M dwarfs can bias R_p/R_s measurements by tens of per cent in the 0.3- to 5.5-μm range (Rackham et al. 2018, 2019). Such effects are evident in some precise visible transmission spectra, both from space (McCullough et al. 2014) and the ground (Rackham et al. 2017). Recent studies have

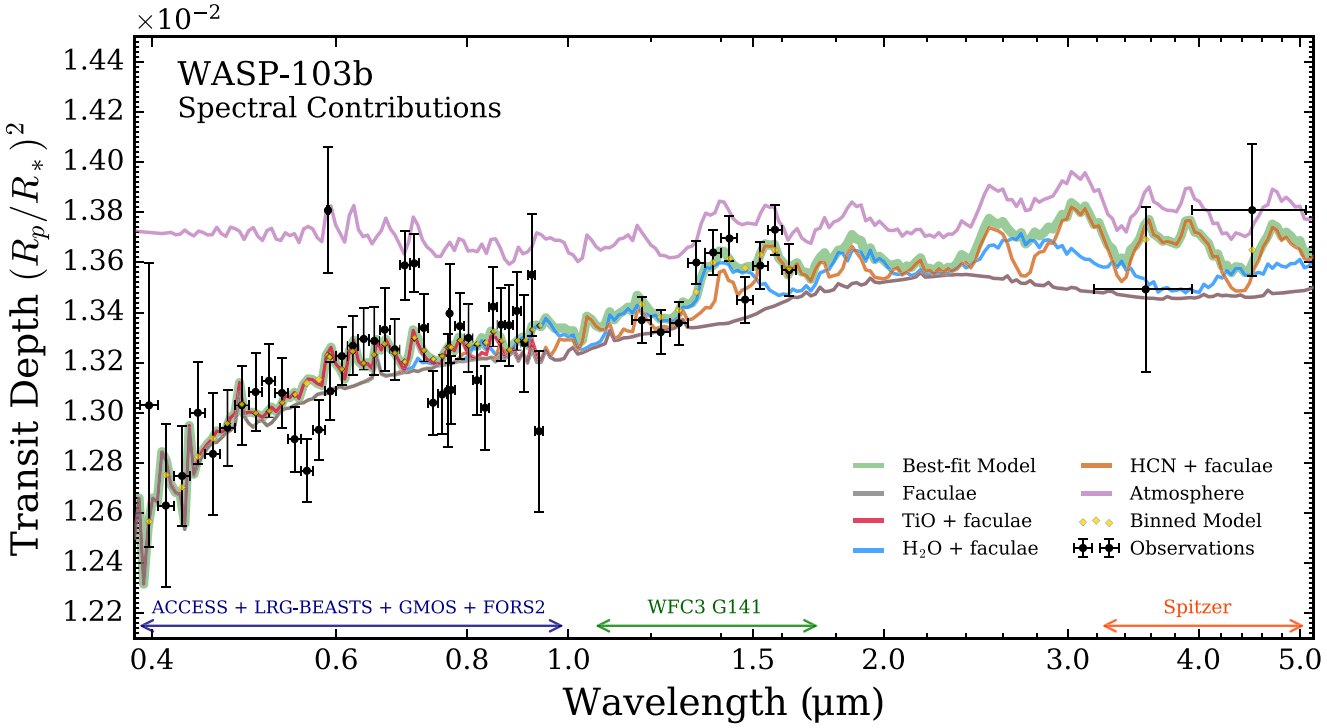

Figure 29 The panchromatic transmission spectrum of ultrahot Jupiter WASP-103b. The spectral impact of unocculted faculae is more pronounced at shorter wavelengths. Retrievals on the NIR *HST* and *Spitzer* data favour the inclusion of faculae at 2.4σ. Including the optical data, combined from 11 ground-based transits with four different facilities, boosts the detection significance of unocculted faculae to 4.3σ. The optical data also boost the detection significance for a planetary atmosphere, inferred by suggestions of TiO, H_2O, and HCN, to 2.8σ from 1.9σ with the NIR data alone. From Kirk et al. (2021).

shown that supplementing space-based NIR observations with optical observations (either ground- or space-based) boosts the detection significance of stellar contamination in transmission spectra and alters interpretations of planetary atmospheric properties (Kirk et al. 2021; Rathcke et al. 2021).

Mitigation in progress

The upcoming NASA Pandora Mission and Ariel Space Mission will collect simultaneous visible and NIR transmission spectra explicitly to account for stellar activity. Pandora, a 0.45-m space telescope planned for launch in the mid-2020s, will observe simultaneously across (∼0.4–1.6 μm) with a photometric channel and a low-resolution ($R \geq 30$) NIR (1.0–1.6 μm) spectroscopic channel (Quintana et al. 2021). Ariel, a 1-m-class space telescope planned for launch in 2029, will similarly observe simultaneously across 0.5–7.8 μm with a combination of short-wavelength photometric and long-wavelength spectroscopic channels (Tinetti et al. 2021).

6 FUTURE COMPLEMENTARY OBSERVATIONS

Essential questions include the following:

(i) What data sets and/or techniques can help to unveil stellar photospheres?

(ii) What strategies would optimize transit spectroscopy given the findings of the SAG?

6.1 Introduction

Exoplanet transmission spectroscopy is a key science case for *JWST* (e.g. Barstow & Irwin 2016; Greene et al. 2016; Morley et al. 2017) and the focus for the upcoming Ariel Space Mission (e.g. Tinetti et al. 2018) and its related NASA Contribution to Ariel Spectroscopy of Exoplanets (CASE) Mission of Opportunity (e.g. Zellem et al. 2019). Both *JWST* and Ariel/CASE will have unprecedented precision to probe exoplanet atmospheres, the former at wavelengths of 0.6–14 μm and the latter at 0.5–7.8 μm. Guided by the findings from Section 2 through Section 5, the goal of this section is to identify current capabilities and future complementary observations that could provide data sets and techniques to constrain stellar heterogeneities in aid of exoplanet transmission spectroscopy studies. Here, we describe the current landscape for ground- and space-based facilities, and identify gaps in observations and capabilities that are needed to mitigate or correct for stellar contamination. We focus first on observations of the Sun and second on observations of exoplanetary host stars.

6.2 Observations of the Sun

Observations of our nearest star provide the best opportunity to resolve and characterize stellar active regions over time. Here, we describe two lines of research that leverage solar observations to inform our understanding of exoplanetary transits: studying the Sun as a resolved star, and studying the Sun as a resolved planetary host. In each context, we discuss the parameters of useful observations and current or future facilities for gathering these data.

6.2.1 Studying the Sun as a resolved star

As described in Section 2, the brightness of the Sun (total and over selected spectral ranges) has been monitored from space since 1978. The Sun's brightness varies on all time-scales accessible to

observations, from minutes to decades (e.g. Kopp 2016). Despite the wealth of solar observations collected to date, resolved observations of the Sun in the visible and IR are still needed to study spectral variations of active regions on minute-to-year time-scales, as noted in Finding 1.1. These are the relevant time-scales spanning single-transit observations and observational campaigns that stack 10 or more transits to build up the necessary signal-to-noise ratio to probe atmospheric features for smaller, cooler exoplanets (e.g. Kreidberg et al. 2014; Benneke et al. 2019a, b).

To understand and model the effect of stellar active regions on these time-scales, it is important to combine information obtained from both long-term, full-disc (i.e. disc-integrated) observations and high-spatial-resolution (sub-arcsec) observations. The former allows an estimate of the temporal evolution of the areal coverage by the different features and an analysis of their properties (both individual and statistical), such as typical sizes, magnetic field, and photometric contrast in specific spectral bands. These quantities are fundamental ingredients of irradiance models and are the main observables for the validation of global dynamo models.

Full-disc observations

A number of existing facilities provide systematic full-disc observations of the Sun. Ground-based facilities targeted to investigate solar variability are typically furnished with broad-band Ca II K filters (see Petrie et al. 2021 for a recent review on Ca II K solar observations), and other broad-band photospheric filters and/or H-alpha filters. Examples of current facilities include the *PSPTs* in Rome (Ermolli et al. 1998) and Hawaii (Rast et al. 1999), and the Solar Observatories of Kanzelhöhe, Tenerife, San Fernando, Kodaikanal, and Mitaka. Furthermore, multiple historical Ca II K archives have been compiled, together providing more than a century of solar full-disc observations (Chatzistergos et al. 2019a, 2020b). Full-disc observations in the UV and EUV, fundamental to understanding and modelling the variability at the shortest wavelengths, are currently provided by AIA onboard SDO and the Solar Ultraviolet Imager (SUVI) onboard the Geostationary Operational Environmental Satellites (GOES) 16 and 17. These will be complemented in the near future with observations acquired in the UV by the *SUIT* instrument on the Indian Aditya-L1 mission (Ghosh et al. 2016). Full-disc continuum images, such as those provided SOHO/MDI or SDO/HMI, have been used to study brightness and other properties of sunspots and their changes over the solar cycle (e.g. Mathew et al. 2007; Kiess, Rezaei & Schmidt 2014; Watson, Penn & Livingston 2014). Full-disc magnetograms acquired in both the photosphere [e.g. SOHO/MDI, SDO/HMI, and International Space Station (ISS)] and chromosphere (e.g. Global Oscillations Network Group, ISS) allow studies of the evolution of the magnetic field over the activity cycle. A combination of full-disc magnetograms and broad-band imagery allows understanding of the relation between the magnetic field and the radiative properties of different features (e.g. Yeo et al. 2013; Criscuoli et al. 2017), and are assimilated in some irradiance reconstruction models (e.g. Krivova et al. 2003).

High-spatial-resolution observations

High-spatial-resolution observations are fundamental to understanding the physical processes that generate, sustain, and dissipate magnetic structures, and that determine their radiative properties. These, in turn, are fundamental for the development and validation of models. Current ground-based facilities, including the *Dunn Solar Telescope*,[15] *SST* (Scharmer et al. 2003), *Goode Solar Telescope* (Goode et al. 2010), and *GREGOR Solar Telescope* (Schmidt et al. 2012), and space-based facilities, including Hinode (Shimizu 2009) and IRIS (De Pontieu et al. 2014), allow the Sun to be observed at sub-arcsec spatial resolution (corresponding to a few hundred kilometres on the Solar surface), at high temporal cadence, and at moderate-to-high spectral resolution. These facilities also typically support spectropolarimetric observations to infer properties of the magnetic fields. The five first-light instruments of *DKIST* (Rimmele et al. 2020) provide solar observations at unprecedented spatial and temporal resolution, at high spectropolarimetric sensitivity, and in a wide spectral range (380–5000 nm) that allows observations of the Sun from the base of the photosphere to the corona. Synergistic observations in the millimetre spectral range with ALMA (Wootten & Thompson 2009) and in the UV with *IRIS* will provide essential information to validate and improve modelling, especially of the chromosphere and corona. Finally, the recently launched Solar Orbiter (Müller et al. 2020) will observe for the first time polar magnetic fields at sub-arcsec spatial resolution, thus providing essential information to improve our understanding of the global dynamo and of the radiative emission of faculae at high latitude.

Although breakthrough discoveries are expected in the understanding of the multiscale, dynamical processes occurring in the solar atmosphere, it should be noted that, because detailed information about physical and magnetic properties of plasma are derived from the analysis of spectral and spectropolarimetric observations, current and future solar facilities typically acquire data at high spectral resolution in relatively narrow spectral ranges (usually not more than ∼1 nm). For the purposes of studying the impact of stellar variability on both planetary atmospheres themselves and our observations of them, however, we are often interested in variability over wider – and sometimes poorly studied – spectral ranges (e.g. Ermolli et al. 2013; Matthes et al. 2017). UV variability, in particular, is known to affect planetary atmospheres and their habitability (Linsky 2017), but unfortunately, this is also the region in which models present the largest discrepancies. Additionally, with the exception of *IRIS*, which has been providing solar spectra in three UV regions since 2012, spatially and spectrally resolved observations in the UV and shorter wavelength ranges, necessary to validate and improve models are scarce (Criscuoli 2019). Most of spatially and spectrally resolved observations in the UV/EUV ranges have been so far rocket- or balloon-born, such as the recently launched (2015) Chromospheric Lyman-Alpha Spectro-Polarimeter (CLASP) or the 2019 Chromospheric Layer Spectropolarimeter (CLASP2), which have collected spectropolarimetric data in the Mg II h & k range (Narukage et al. 2016). The Sunrise UV Spectropolarimeter and Imager (Feller et al. 2020) onboard the SUNRISE III balloon, planned for launch in 2023, will provide for the first time sub-arcsec, spectropolarimetric observations of the Sun in the near-UV (300–400 nm) at a spectral resolution of ∼2 nm. The SUIT instrument on the Indian Aditya-L1 space mission, also planned for launch in 2023, will image the Sun for the first time in both broad and narrow spectral bands in the UV range from 200 to 400 nm (Ghosh et al. 2016).

6.2.2 Studying the Sun as a resolved planetary host

In addition to using the Sun to learn about other stars, the planets in our Solar system provide opportunities to learn about exoplanets. Several 'Earth as an exoplanet' studies have discussed the potential of using observations of the Earth from past planetary science missions (fly-bys) or current Earth science missions (e.g. EPOXI/DISCOVR) to identify key features that are observable for exoplanets (e.g. Cowan et al. 2009; Llama & Shkolnik 2015, 2016; Berdyugina &

[15] https://nso.edu/telescopes/dunn-solar-telescope/dunn/

Kuhn 2019). Recently, Mayorga et al. (2021) proposed that a small spacecraft at Earth–Sun L2 could potentially observe transits of the Earth and Moon across the Sun during periods of high activity. These observations would provide several means towards understanding the biases imparted on transmission spectra from active regions. For example, knowing a priori that a planet transits a star with numerous active regions and has a flat transmission spectrum (because the planet has no atmosphere, a high mean-molecular-weight atmosphere, or high gravity) would provide a testing ground for understanding the effects of occulted and unocculted active regions on the planet's measured transmission spectrum. Such an experiment would benefit from our knowledge of the properties of active regions from ground-based solar telescopes, thus providing quantitative points of comparison with the ground truth for active regions of various temperatures and sizes.

6.2.3 Our finding: Finding 5.1

From this analysis, we draw the following findings:

Summary

Our understanding of stellar photospheric heterogeneity and its impact on observations of transiting exoplanets is informed greatly by studies of the Sun. While many suitable facilities exist to study the Sun as a star, the field would benefit from additional capabilities to study planetary transits of the Sun.

Capability needed

Resolved observations of the Sun in the visible and IR are needed to study spectral variations of active regions on minute-to-year timescales. Observations of planetary bodies transiting the Sun, either resolved or unresolved, are needed to provide the ground-truth for exoplanetary transits.

Capability today

Many ground- and space-based facilities exist to study the Sun as a resolved star. Full-disc Ca II K observations of the Sun are available spanning more than the last century (Chatzistergos et al. 2019b, 2020b). Full-disc observations in the UV and EUV are provided by SDO/AIA and GOES/SUVI. Ground-based facilities, such as the *Dunn Solar Telescope*, *Swedish Solar Telescope* (Scharmer et al. 2003), *Goode Solar Telescope* (Goode et al. 2010), and *GREGOR Solar Telescope* (Schmidt et al. 2012), as well as space-based facilities, including Hinode (Shimizu 2009) and *IRIS* (De Pontieu et al. 2014), provide high-cadence observations of the Sun at sub-arcsec spatial resolution and moderate-to-high spectral resolution. No dedicated facilities exist to study planetary transits of the Sun.

Mitigation in progress

When fully operational, *DKIST* (Rimmele et al. 2020) will provide sensitive solar observations with unprecedented spatial and temporal resolution and across a wide spectral range of interest to exoplanetary transit observations (380–5000 nm). The Sunrise UV Spectropolarimeter and Imager (Feller et al. 2020), planned for launch in 2023 onboard the SUNRISE III balloon, will provide sub-arcsec, spectropolarimetric observations of the Sun in the near ultraviolet (NUV) (300–400 nm) at a spectral resolution of ∼2 nm. Also planned for launch in 2023, the SUIT instrument (Ghosh et al. 2016) on the Indian Aditya-L1 space mission will image the Sun in broad and narrow spectral bands in the UV (200–400 nm).

6.3 Observations of exoplanetary host stars

Understanding stellar activity, both the observations and the theory behind what physical processes drive the observations, requires a multiwavelength, multifacility approach. Here, we describe useful avenues to better constrain exoplanet host stars in upcoming years in the context of photometry, UV observations, and advances in interferometry.

6.3.1 Photometric approaches to constrain active-region parameters

Long-baseline photometry

Precise, time-domain photometric surveys (e.g. *CoRoT*, *Kepler*, *K2*, and *TESS*) have revolutionized our understanding of stellar activity by enabling the measurements of stellar flares and stellar rotation for a wide range of spectral types. As discussed in Section 4.3.2, long-baseline photometry of exoplanet host stars can be used effectively to monitor for epoch-to-epoch stellar variability (e.g. Knutson et al. 2012; Sing et al. 2015; Mallonn & Strassmeier 2016; Zellem et al. 2017; Mallonn et al. 2018; Mansfield et al. 2018; Kilpatrick et al. 2020; Rosich et al. 2020). Complementary observations from the ground allow us to place comparatively temporally limited observations with space-based observatories into a larger baseline to explore whether any observed variations can be attributed to the variability of the host star. These observations can be conducted on a variety of platforms, from automatic robotic telescopes (e.g. Dukes 1992) to even 15-cm-class telescopes, which have the potential to observe even a relatively dim 11.3 V-mag host star with a per-minute precision of 0.67 per cent (Zellem et al. 2020). From space, the recently selected Pandora SmallSat Mission (Quintana et al. 2021) will explore the potential of small telescopes (0.45 m) to reliably constrain stellar photospheres and exoplanetary atmospheres by collecting multi-epoch, long-baseline transit observations of active K- and M-type exoplanet hosts with simultaneous visible photometry and NIR spectroscopy. Likewise, the Ariel Space Mission (Tinetti et al. 2021) will study planetary transits across 0.5–7.8 μm with a combination of short-wavelength photometric channels (0.5–0.60, 0.6–0.80, and 0.80–1.10 μm) and long-wavelength spectroscopic channels (1.10–1.95 μm at $R \geq 15$ and 1.95–7.8 μm at R ∼30–100).

Multiband photometry

While photometric monitoring of exoplanet host stars can give insights into their epoch-to-epoch variability, detailed modelling of the stellar activity is generally limited by degeneracies between the spot temperature and spot size. For instance, a small, cool spot can produce the same amount of flux to first order as a large, comparatively warm/bright spot. As discussed in Section 4.3.1, however, multiband photometry can provide the necessary constraints to resolve this degeneracy and better understand the impact of active regions on stellar spectral contamination in exoplanetary transmission spectra. For example, TiO forms in cooler spots but dissociates at hotter temperatures (Berdyugina, Solanki & Frutiger 2003; Mirtorabi, Wasatonic & Guinan 2003). Therefore, one can perform simultaneous observations of the host star both inside the TiO band and just outside to provide measurements of the starspot temperature and, thus, its size (e.g. Zellem et al. 2010). Such a study was done of the chromospherically active star IM Peg using the relatively small 0.75-m *Four College Consortium Telescope* (Dukes 1992) as well as spectroscopy with the 2.5-m *Nordic Optical Telescope* (Berdyugina et al. 1999). This study and others like it show that, while these observations can be time-consuming, they potentially could be shifted to smaller telescopes, alleviating the need for larger telescopes (Zellem et al. 2020). Here too the Pandora SmallSat Mission (Quintana et al. 2021) will provide a relevant

space-based counterpart with its simultaneous visible photometry and NIR spectroscopy designed to uniquely identify the properties of heterogeneous photospheres with absolutely calibrated, multi-epoch observations.

Existing data sets and underutilized avenues for photometry

Existing single- or multiband photometry may be available for a given exoplanet host, given the abundance of existing time-domain photometric surveys, including those searching for transiting exoplanets, such as *Kepler* (Borucki et al. 2010), *TESS* (Ricker et al. 2014), HAT-P (Bakos et al. 2004), WASP (Pollacco et al. 2006), HATS (Bakos et al. 2013), MEarth (Nutzman & Charbonneau 2008), NGTS (Wheatley et al. 2018), SPECULOOS (Delrez et al. 2018), EDEN (Gibbs et al. 2020), and more. If data are not already available from a targeted or wide-field survey, monitoring the star over multiple rotation periods could be time-consuming. Spun-down M dwarfs, e.g. can have periods as long as 140 d (Newton et al. 2018). However, while monitoring exoplanet host stars over multiple rotation periods is challenging due to the oversubscription of professional observatories, there is the opportunity for amateur astronomers to contribute. For example, the American Association of Variable Star Observers has been observing variable stars for ∼100 yr and has over 2 million stars in its Variable Star Index (Watson, Henden & Price 2006).

High-cadence photometry

Finally, obtaining high-cadence photometry will help in a number of areas. Searches for flares with high-cadence photometry has a surprisingly long history, including detections of flares with sub-second time resolution in the 1980s (Beskin et al. 1988). *TESS* has opened the latest frontier in this research area with its recently introduced 20-s cadence mode, which can be used to resolved short-duration activity such as flares, but the number of stars observed at short cadence is typically limited. CHEOPS can also collect photometry at a sub-minute cadence (Benz et al. 2021), and PLATO will include 32 cameras with a 25-s readout cadence and two with a 2.5-s cadence (Rauer et al. 2014). High-cadence observations which fully resolve the ingress and egress of the transit can independently constrain the planetary radius even when the transit is contaminated by significant spot occultation events (Morris et al. 2018b).

6.3.2 UV observations to inform models of host-star atmospheres

With the wealth and quality of existing solar observations, highly sophisticated semi-empirical models of the Sun have been developed, including complex models of spots, flares, and other magnetic phenomena (See Section 2). Extensive modelling efforts have furthered our understanding of the solar interior (e.g. Vinyoles et al. 2017), the detailed structure in the upper atmosphere (Fontenla et al. 2006), and the solar activity cycle and associated energetic events (e.g. Yeo et al. 2014b; Hathaway 2015; Desai & Giacalone 2016). The current state-of-the-art for stellar atmosphere models of lower-mass, planet-hosting stars, including K and M dwarfs, is not at the same level as solar models, due in part to the additional complexity involved in modelling these objects (e.g. Iyer et al. 2023) and in part to the disparity in the quality and quantity of X-ray–NUV spectra available (e.g. France et al. 2016). In the context of exoplanet transmission spectroscopy, an accurate understanding of the high-energy radiation of host stars is crucially important, as it drives HD escape of planetary atmospheres (e.g. Lammer et al. 2003; Murray-Clay, Chiang & Murray 2009), leading to observations of comet-like evaporation tails (e.g. Vidal-Madjar et al. 2004; Kulow et al. 2014; Spake et al. 2018) and perhaps shaping the mass–radius distribution of close-in exoplanets (e.g. Owen & Jackson 2012; Owen & Wu 2013, 2017). Stellar modelling efforts would greatly benefit from a future EUV/FUV/NUV dedicated mission with time-dependent measurements to improve our understanding of active-region coverage and temperature, and flare frequency, size, and colour on these low-mass, planet-hosting stars. With this knowledge, composite semi-empirical models of stellar atmospheres could be developed, complete with accurate and precise modelling of PCHs that would, amongst other things, advance the general understanding of stellar atmospheres and improve our ability to disentangle the stellar and planetary contributions from UV transit spectra.

6.3.3 Constraining host-star surface inhomogeneities through interferometric imaging

Global surface temperature maps

Stellar surfaces have been indirectly imaged for decades using DI (e.g. Berdyugina 2005; Strassmeier 2009; Korhonen et al. 2021) and light-curve imaging (e.g. Lanza et al. 1998; Berdyugina et al. 2002; Roettenbacher et al. 2013) in order to detect surface inhomogeneities, such as starspots and faculae (see also Section 2). In these methods, either high-resolution spectra or photometric observations are used to obtain maps of the stellar surface with inversion methods. Light-curve inversion imaging reconstructs the stellar surface based upon the observed brightness fluctuations. DI utilizes the evolution of distortions of absorption lines caused by surface features rotating in and out of view to reconstruct the features of the stellar surface. Both methods suffer from degeneracies, especially for the latitudinal information of the spots. The determination of starspot latitudes is constrained in light-curve inversion with limb-darkening laws and estimated coefficients, while in DI with the location of the spot feature within absorption line profiles and the speed at which it crosses the profile as the star rotates. While the light-curve method cannot provide starspot latitudes, the DI can locate spot latitudes and longitudes within the stellar hemisphere that is best visible to the observer with respect to the equator, as was demonstrated by modelling various spots (e.g. Vogt & Penrod 1983; Piskunov et al. 1990; Berdyugina 1998).

In recent years, advances in long-baseline optical/NIR interferometry have enabled the direct-imaging of starspots on stellar surfaces (Roettenbacher et al. 2016, 2017; Martinez et al. 2021; Parks et al. 2021). This is the only method that can obtain reliable, unambiguous information of the spot locations in latitude and longitude within both stellar hemispheres relative to the equator. However, the targets currently accessible with present interferometric resources are limited, as this technique requires very bright targets with spots that appear large enough on the sky. Additionally, obtaining a complete image of the stellar surface requires repeated observations with phase coverage across a rotation. This can require large amounts of dedicated observing time. The relative rate of evolution of the surface structure compared with the stellar rotation must also be considered.

Currently, the highest spatial resolution can be reached by MIRC-X instrument (Anugu et al. 2020) at the CHARA Array (ten Brummelaar et al. 2005), which can provide an angular resolution of about 0.4 mas. MIRC-X is also the only instrument that can combine light from all the six 1-m telescopes of the CHARA Array, making it the instrument that is best suited for interferometric imaging of stellar surfaces. Another facility that can be used for interferometric imaging is ESO's Very Large Telescope Interferometer (VLTI). The best angular resolution of the VLTI can be reached using the Precision

Integrated Optics Near Infrared ExpeRiment instrument (Le Bouquin et al. 2011) that gives angular resolution of about 1.3 mas. VLTI can combine four telescopes simultaneously and has changeable array configurations with the 1.8-m auxiliary telescopes. VLTI can also combine the light from the four 8.2-m *Unit Telescopes*, which gives the current faintest limiting magnitudes for infra-red interferometry (GRAVITY instrument: $K = 10.5$ for on-axis observations and $K = 17$ when using a close-by bright fringe tracker star; Gravity Collaboration et al. 2017).

The number of targets that can be accurately mapped using interferometric imaging is still limited to a handful of bright, nearby stars that have angular diameters of about 2.0 mas or larger. The technique, however, importantly opens a new parameter space that is not accessible using DI or light-curve inversion imaging: cool, aged, main-sequence stars. Due to their slow rotation, DI cannot be used to image these stars. Cool, nearby, main-sequence stars include some exoplanet hosts, like ϵ Eridani.

New exciting discoveries are made with each new image obtained of stellar surfaces. Future advances in interferometric imaging can be made by: increasing the number of telescope that are combined to improve the image fidelity, moving towards shorter wavelengths to obtain higher angular resolution, and increasing the length of the longest baselines to obtain higher angular resolution. Many of these aspects will be addressed, e.g. by the Visible Imaging System for Interferometric Observations (VISION; Garcia et al. 2016) instrument at the upgraded Navy Precision Optical Interferometer (NPOI; van Belle et al. 2020a) and the Stellar Parameters and Images with a Cophased Array (SPICA; Pannetier et al. 2020) at the CHARA Array (ten Brummelaar et al. 2005).

Because the light detected with long-baseline optical interferometers must be combined at the telescopes, there are physical limitations to the size of ground-based interferometers. While efforts are being made to investigate kilometre baselines (e.g. Monnier et al. 2018), space-based interferometers (e.g. Monnier et al. 2018; van Belle et al. 2020b) could alleviate some of the constraints on ground-based optical interferometers, allowing for increased resolution and increased targets.

Empirical determination of fundamental stellar parameters

Precise stellar parameters, including stellar radius, surface temperature, and limb darkening, are crucial for correctly interpreting exoplanet observations. High-resolution spectroscopy from the ground provides the main avenue for determining stellar parameters of exoplanet hosts, including large efforts focused on FGK stars by the SWEET-Cat (Santos et al. 2013; Sousa et al. 2021), Ariel (Danielski et al. 2022; Magrini et al. 2022), and GAPS teams (e.g. Biazzo et al. 2022) and on M dwarfs by the CARMENES team (e.g. Passegger et al. 2018; Marfil et al. 2021). As a complement to these efforts, interferometry offers a powerful, direct, empirical means to determine the fundamental physical properties of stars. While most stars cannot be resolved with current single-dish, ground- and space-based telescopes, long-baseline optical and NIR interferometers consisting of individual telescopes connected as an array can provide accurate information on these parameters. When resolved stars are observed with interferometry the measured squared visibility changes with the baseline (distance between two telescopes) and wavelength. When limb-darkened disc models are fit to the observed squared visibilities, the apparent stellar diameter and limb-darkening profile can be determined. Additionally, the effective temperature can be measured when the stellar diameter is combined with observations of the bolometric flux.

Stellar diameters and limb-darkening laws have been determined interferometrically for many stars, both F to M subgiants and giants and A to M nearby main-sequence stars (e.g. Nordgren et al. 1999; Di Folco et al. 2004; Boyajian et al. 2012a, b, 2013; Mann et al. 2015). Interferometric measurements of stellar diameters have enabled the calibration of surface–brightness relations of dwarfs, subgiants, giants, and more (Kervella et al. 2004a, b; Kervella & Fouqué 2008). Diameter measurements have also been carried out for exoplanet host stars (see e.g. Baines et al. 2008, 2009; Bazot et al. 2011; Crida et al. 2018; White et al. 2018). These observations have shown the necessity of having sufficiently long baselines for accurately resolving targets with small angular diameters. Additionally, one has to take great care when selecting the calibration stars. Calibration stars are ideally nearby on the sky, of similar spectral type, single, and unresolved by the interferometer. Instrumentation developments that are ideally suited for studying smaller exoplanet host stars include VISION at NPOI (Garcia et al. 2016; van Belle et al. 2020a) and SPICA at the CHARA Array (ten Brummelaar et al. 2005; Pannetier et al. 2020). With instruments working in the visible wavelength range and with the long baselines of 432 and 330 m, respectively, NPOI and the CHARA Array are ideal facilities for studying fundamental stellar parameters of the exoplanet host stars in the future.

Complementing these capabilities is the method of 'pseudo-interferometry' (Stassun et al. 2017, 2018), in which the stellar angular radius is determined through an inversion of the Stefan-Boltzmann relation, $\Theta = \left(F_{\rm bol}/\sigma_{\rm SB}T_{\rm eff}^4\right)^{1/2}$, in which $F_{\rm bol}$ is the bolometric flux, $\sigma_{\rm SB}$ is the Stefan–Boltzmann constant, and $T_{\rm eff}$ is the effective temperature. The physical radius then follows directly via the distance as determined, e.g. with a precise Gaia parallax. This approach does require an independent determination of $T_{\rm eff}$, preferably via a high-quality spectroscopic analysis. As demonstrated by Stassun et al. (2017), the availability of broad-band apparent magnitudes spanning from the UV to the mid-IR allows $F_{\rm bol}$ to be determined with a typical precision of a few per cent, and in the best cases $T_{\rm eff}$ determined to a precision of 1–2 per cent, such that angular radii for typical planet-host stars can be measured to 2–3 μm, rivaling that of interferometric imaging for the brightest stars (though without the benefit of resolving surface inhomogeneities, of course). Moreover, as ultraprecise parallaxes are now routinely available with *Gaia*, physical radii for typical stars via pseudo-interferometry can be determined to better than a few per cent (Stassun et al. 2017). Finally, such pseudo-interferometric stellar radii can be further leveraged to measure the masses of single stars empirically as well, if a precise surface gravity is available such as through the technique of granulation 'flicker' from a light curve (Bastien et al. 2013, 2016). Masses of individual FGK dwarf, subgiant, and giant stars can be determined via this pseudo-interferometric + flicker gravity method to better than 10 per cent in many cases and as good as a few per cent in the best cases (Stassun et al. 2018).

6.3.4 *Our finding:* ***Finding 5.2***

From this analysis, we draw the following findings:

Summary

Many existing facilities can be leveraged to study exoplanet host stars photometrically, though there is a need to scale observations to study a large number of exoplanet host stars with long-term, multiband photometry. UV observations are also essential to inform models of host-star atmospheres, and time-dependent measurements provide valuable information on active-region coverage and temperature as well as flare frequency and magnitude. At the same time, advances in interferometric technique enable constraints on

photospheric properties of nearby dwarfs, including some exoplanet hosts; of specific interest is the direct mapping of temperature inhomogeneities on stellar surfaces.

Capability needed

Long-baseline, multiband photometry of active exoplanet host stars is needed to uniquely constrain active-region temperatures and sizes. Stellar modelling efforts would greatly benefit from a future EUV/FUV/NUV dedicated mission with time-dependent measurements to improve our understanding of active-region coverage and temperature, and flare frequency, size, and colour on these low-mass, planet-host stars. Much longer baseline interferometric imaging capabilities on the ground and/or in space would allow mapping of stellar surface inhomogeneities for a much larger sample of stars; currently this can only be done for a handful of bright, nearby stars with angular diameters larger than ∼2 mas.

Capability today

Photometric studies of exoplanet host stars benefit from many capable facilities, including dedicated transit-search networks and longstanding contributions from amateur astronomers (e.g. Zellem et al. 2020). Space-based platforms are being used to build panchromatic (X-ray–mid-IR) SEDs of nearby planet-hosting stars (France et al. 2016), providing inputs to models of stellar atmospheres and chemical evolution of associated planetary atmospheres. High-resolution stellar spectroscopy from the ground provides a strong avenue for characterizing the fundamental properties of exoplanet host stars, and large community efforts have pushed this work forward (e.g. Nordlund 1982; Santos et al. 2013; Passegger et al. 2018; Marfil et al. 2021; Sousa et al. 2021; Biazzo et al. 2022; Danielski et al. 2022). Long-baseline optical/NIR interferometry provides diameter measurements of exoplanet host stars (e.g. Baines et al. 2008, 2009; Bazot et al. 2011; Crida et al. 2018; White et al. 2018). In tandem with photometric and RV measurements, interferometry also provides an opportunity to directly image starspots of nearby, main-sequence exoplanet hosts (Roettenbacher et al. 2022).

Mitigation in progress

The extended *TESS* mission (Ricker et al. 2015) continues to provide long-baseline photometry in a broad red-optical bandpass for targets over nearly the whole sky. The recently selected Pandora SmallSat Mission (Quintana et al. 2021) will provide both long-baseline monitoring and transit observations simultaneously in a visible photometric bandpass and a NIR spectroscopic channel for at least 20 planets transiting K and M dwarfs over a 1-yr mission. Similarly, the Ariel Space Mission (Tinetti et al. 2021) will provide simultaneous visible photometry and NIR spectroscopy of roughly 1000 exoplanets over a 4-yr mission.

7 CONCLUSIONS

We have presented the analysis and findings of SAG21, an interdisciplinary group of more than 100 scientists that examined the impact of stellar contamination on space-based transmission spectra of exoplanets. The analysis was expansive, with subgroups of SAG21 focused on stellar photospheric and chromospheric heterogeneity, unocculted active regions, occulted active regions, stellar and planetary retrievals, and future complementary observations. In total, the analysis produced 14 findings, contextualized statements of what we understand to be the current research needs that can be addressed to further our understanding of stellar photospheres and make the best use of precise space-based transmission spectra of exoplanets.

To summarize these findings further, Fig. 30 presents a set of summary science questions and needs that are common to several findings at a time. These fall into three science themes encompassing (i) how the Sun is used as our best laboratory to calibrate our understanding of stellar heterogeneities (‘The Sun as the Stellar Benchmark’), (ii) how stars other than the Sun extend our knowledge of heterogeneities (‘Surface Heterogeneities of Other Stars’), and (iii) how to incorporate information gathered for the Sun and other stars into transit studies (‘Mapping Stellar Knowledge to Transit Studies’).

The following subsections summarize in turn the scope of the five subgroups and their findings. For brevity, only the summary statement of each finding is reproduced here. The full findings in the format of NASA’s Exoplanet Exploration Program Science Gap List, including descriptions of the capability needed, capability today, and mitigation in progress, are available in their respective sections of this review.

7.1 Stellar photospheric and chromospheric heterogeneity

The stellar photospheric and chromospheric heterogeneity subgroup was tasked with summarizing our knowledge of the heterogeneity of stellar photospheres and chromospheres and ongoing work to understand relevant properties for the purpose of transmission spectroscopy. The members considered observational and modelling efforts to understand the heterogeneity of the Sun at wavelengths relevant to transit studies and comparable efforts for other stars, including exoplanet hosts. Their analysis produced three findings.

7.1.1 Finding 1.1

The Sun provides the benchmark for stellar studies. Studying the spatial, spectral, and temporal variations of stellar surface structures is necessary for understanding the impact of analogous structures on transmission spectroscopy of exoplanets.

7.1.2 Finding 1.2

More modelling work is needed to understand how the fundamental parameters of stars other than the Sun govern their magnetic fields and the associated properties of their surface inhomogeneities. In accordance with observations, simulations show that many lower-activity stars, such as exoplanet hosts that might be deemed as ‘low risk’ for transmission spectroscopy in terms of stellar activity, are facula-dominated (Shapiro et al. 2014; Nèmec et al. 2022). However, little is known on how facular contrasts and coverages depend on stellar activity levels and fundamental parameters, such as metallicity and surface gravity. Both observing and modelling the fine structure of spots on stellar surfaces remain a challenge.

7.1.3 Finding 1.3

Simultaneous multiwavelength (multi-instrument) stellar observations are needed to provide feedback to modelling efforts and improve our understanding of the photospheres and chromospheres of other stars, including high-priority exoplanet host stars. This is particularly critical for K, M, and L dwarfs, for which models are relatively poorly constrained.

7.2 Occulted active regions

The occulted active regions subgroup was tasked with evaluating what we can learn from planetary occultations of stellar active regions during transits. The members considered the state of the art for observations and models of active-region occultations, outstanding

SAG21 Summary Questions & Needs

The Sun as the Stellar Benchmark

Science questions	Needs	Relevant findings
What are the **spectral properties of solar photospheric and chromospheric heterogeneities** as a function of time and location?	- Theoretical understanding of spot sizes, locations, lifetimes, and contrasts in the 0.3-5.0 μm range. - Resolved observations of the Sun, including spots and faculae, over 0.3-5.0 μm at resolutions relevant to space-based transit observations.	1.1, 3.2, 5.1
What are the **spectral properties of solar granules**?	- Validate 3D simulations of solar granulation against optical and NIR observations.	1.1, 3.3

Image credit: Andrew McCarthy

Surface Heterogeneities of Other Stars

Science questions	Needs	Relevant findings
How are the **spectral properties of spots and faculae** governed by the **fundamental parameters of stars**?	- 3D MHD simulations of magnetic features that provide priors on facular and spot spectra and coverages for different spectral types.	1.2, 4.3
What are the **spectral properties of spots and faculae** on high-priority **exoplanet host stars**?	- Observational constraints of exoplanet hosts, including photometry, spectroscopy, and spectropolarimetry, to use as feedback for stellar models	1.3, 3.2
What is the **impact of granulation** on precise transit studies?	- Validate 3D granulation simulations against optical and NIR light curves for a range of spectral types.	3.3

Image credit: Greg Hogan

Mapping Stellar Knowledge to Transit Studies

Science questions	Needs	Relevant findings
How do we **translate knowledge** of stellar heterogeneities in other stars **to transit observations**?	- Establish best practices for incorporating stellar heterogeneity in transit studies and atmospheric retrievals, including priors from stellar models of spots and faculae. - Study planetary transits of the Sun with existing and future datasets as ground truth for exoplanetary transits. - Collect panchromatic stellar observations, including UV-to-IR spectra and long baseline photometry. - Use interferometric observations to establish ground truth for photometric variations.	2.1, 2.2, 4.1, 4.2, 5.1, 5.2
What **unique constraints** on stellar heterogeneity are **enabled by transit observations**?	- Maintain publicly accessible and up-to-date tools for modeling active-region occultations. - Further pursue theoretical work connecting observational signatures in light curves to stellar physical parameters.	2.2, 2.3, 3.1

Image credit: ESA/ATG medialab

Figure 30 A summary of SAG21 in terms of its science questions, needs identified, and relevant findings.

theoretical challenges for these studies, and the availability of well-maintained tools for conducting these analyses. Their analysis produced three findings.

7.2.1 Finding 2.1

Precise transit observations increasingly reveal occultations of stellar active regions. Rather than flagging and removing active-region occultations, which results in decreased observing efficiency and possibly biased transit depth measurements, future observations should move towards joint inference of the active-region and planetary properties.

7.2.2 Finding 2.2

Theoretical advances are needed to understand the limits of what we can infer about active-region properties from transit light curves and how best to incorporate prior knowledge from MHD models into transit studies.

7.2.3 Finding 2.3

Several publicly available tools have been developed for forward-modelling active-region occultations. Their maintenance and further development is necessary to ensure their utility for analyses of precise transit observations.

7.3 Unocculted active regions

The unocculted active regions subgroup was tasked with examining our knowledge of host-star active regions that are not occulted by transiting exoplanets. The members considered what information can be obtained about unocculted active regions from high-cadence transit photometry, the utility of other data sets – current or planned – for inferring the presence of active regions and their properties, and the effects of stellar granulation on transmission spectra. Their analysis produced three findings.

7.3.1 Finding 3.1

High-cadence light curves provide the potential to understand unocculted active regions, but the information is not comprehensive enough to make unambiguous measurements at present. Theoretical advances are needed to make full use of these light curves.

7.3.2 Finding 3.2

Simultaneous multiband photometry and contemporaneous spectroscopy provide critical information towards understanding the potential effects of active regions on transmission spectroscopy observations. While other data sets can provide information on filling factors, theoretical work is needed to maximize the utility of these data for transmission spectroscopy.

7.3.3 Finding 3.3

Stellar 'granulation flicker' constitutes a fundamental 'noise floor' on stellar light curves that increases with decreasing stellar surface gravity and at shorter wavelengths. The impact of this stellar granulation can enter as a source of noise and/or contamination for transmission spectroscopy in two ways. The first is through extra light curve scatter, the impact of which is minimal in most cases (at most $\sim$0.05-per cent error on the transit depth in the visible and even less at longer wavelengths). The second is through a contamination source similar to that of spots and faculae, albeit at a much lower amplitude ($\sim$ 1 per cent of the transit depth at about 0.7 μm). This second source is significant at short wavelengths for smaller exoplanets around Sun-like stars, but decreases strongly as a function of wavelength.

7.4 Stellar and planetary retrievals

The stellar and planetary retrievals subgroup was tasked with studying how we can best use inference frameworks to constrain the properties of stellar photospheres and exoplanetary atmospheres jointly from transmission spectra and other relevant inputs. The members considered the utility of joint stellar and planetary retrievals generally, the known limitations of the approach, and the complementarity of short-wavelength observations to *HST* and *JWST* NIR observations for inferring stellar photospheric properties. Their analysis produced three findings.

7.4.1 Finding 4.1

Retrievals of transmission spectra that include the effects of unocculted active regions can guard against biases. More work is needed to understand when these retrievals are necessary and what are the limitations and best practices of this approach.

7.4.2 Finding 4.2

Retrieval approaches rely on stellar models, and thus their accuracy is limited by model fidelity and, depending on the approach, the prior information on stellar parameters used in the retrieval. Further efforts to develop model spectra for spots and faculae and incorporate them into exoplanetary atmospheric retrievals are needed.

7.4.3 Finding 4.3

For low-resolution transmission spectra, the impact of unocculted active regions is larger at shorter wavelengths. More work is needed to quantify the complementary nature of such spectra for *JWST* observations.

7.5 Future complementary observations

The future complementary observations subgroup was tasked with assessing the current landscape for ground- and space-based facilities that can provide useful complements for *HST* and *JWST* studies of transiting exoplanets. The subgroup was also tasked with identifying gaps in capabilities that are needed to mitigate or correct for stellar contamination. The members considered observations of the Sun that are informative in this context as well as observations of exoplanetary host stars themselves. Their analysis produced two findings.

7.5.1 Finding 5.1

Our understanding of stellar photospheric heterogeneity and its impact on observations of transiting exoplanets is informed greatly by studies of the Sun. While many suitable facilities exist to study the Sun as a star, the field would benefit from additional capabilities to study planetary transits of the Sun.

7.5.2 *Finding 5.2*

Many existing facilities can be leveraged to study exoplanet host stars photometrically, though there is a need to scale observations to study a large number of exoplanet host stars with long-term, multiband photometry. UV observations are also essential to inform models of host-star atmospheres, and time-dependent measurements provide valuable information on active-region coverage and temperature as well as flare frequency and magnitude. At the same time, advances in interferometric technique enable constraints on photospheric properties of nearby dwarfs, including some exoplanet hosts; of specific interest is the direct mapping of temperature inhomogeneities on stellar surfaces.

ACKNOWLEDGEMENTS

J.K.B. acknowledges support from an STFC Ernest Rutherford Fellowship. S.V.B. was supported by the European Research Council Advanced Grant HotMol ERC-2011-AdG291659. G.B. acknowledges support from CHEOPS ASI-INAF agreement n. 2019-29-HH.0. H.M.C. acknowledges support from a UKRI Future Leaders Fellowship MR/S035214/1. C.D. acknowledges the support from NASA XRP grant 80NSSC21K0608. E.D. acknowledges the Paris Region fellowship programme which is supported by the Ile-de-France Region and has received funding under the Horizon 2020 innovation framework programme and the Marie Sklodowska-Curie Actions grant agreement no. 945298. A.I. and M.L. acknowledge support from NSF Award Number: 2009592. G.K. was supported by NASA's TSIS program under contract NNG09HP02C. B.V.R. and R.M.R. thank the Heising-Simons Foundation for support. A.I.S. is supported by the by the European Research Council (ERC) under the European Union's Horizon 2020 research and innovation programme (grant agreement No. 715947). K.G.S. acknowledges generous support from NASA XRP grant 80NSSC18K0445. Y.C.U. acknowledges support from STFC through grant ST/S000372/1. S.W. is supported by the European Research Council (ERC) under the European Union's Horizon 2020 research and innovation programme (grant agreement No. 682462), and by the Research Council of Norway through its Centres of Excellence scheme (project number 262622) and FRIPRO scheme (project number 286853). We thank the three anonymous reviewers for their careful reading of the manuscript and their helpful comments. Part of the research was carried out at the Jet Propulsion Laboratory, California Institute of Technology, under a contract with the National Aeronautics and Space Administration (80NM0018D0004). This material is based upon work supported by the National Aeronautics and Space Administration under Agreement No. 80NSSC21K0593 for the program 'Alien Earths'. The results reported herein benefited from collaborations and/or information exchange within NASA's Nexus for Exoplanet System Science (NExSS) research coordination network sponsored by NASA's Science Mission Directorate. This research was supported by the Excellence Cluster ORIGINS which is funded by the Deutsche Forschungsgemeinschaft (DFG, German Research Foundation) under Germany's Excellence Strategy - EXC-2094 - 390783311. The National Solar Observatory is operated by the Association of Universities for Research in Astronomy, Inc. (AURA), under cooperative agreement with the National Science Foundation. This research has made use of the NASA Exoplanet Archive, which is operated by the California Institute of Technology, under contract with the National Aeronautics and Space Administration under the Exoplanet Exploration Program. This research has made use of NASA's Astrophysics Data System.

DATA AVAILABILITY

Most data sets presented in this report have been summarized from the scientific literature and can be found at the cited references. Data relating to any new analyses presented here are available upon reasonable request.

REFERENCES

Adjabshirzadeh A., Koutchmy S., 1983, A&A, 122, 1
Aerts C., 2021, Rev. Mod. Phys., 93, 015001
Afram N., Berdyugina S. V., 2015, A&A, 576, A34
Afram N., Berdyugina S. V., 2019, A&A, 629, A83
Agol E., Steffen J., Sari R., Clarkson W., 2005, MNRAS, 359, 567
Agol E., Cowan N. B., Knutson H. A., Deming D., Steffen J. H., Henry G. W., Charbonneau D., 2010, ApJ, 721, 1861
Ahern S., Chapman G. A., 2000, Sol. Phys., 191, 71
Aigrain S., Pont F., Zucker S., 2012, MNRAS, 419, 3147
Alexoudi X., Mallonn M., Keles E., Poppenhäger K., von Essen C., Strassmeier K. G., 2020, A&A, 640, A134
Allard F., Guillot T., Ludwig H.-G., Hauschildt P. H., Schweitzer A., Alexander D. R., Ferguson J. W., 2003, Proc. IAU Symp. 211, Brown Dwarfs. Astron. Soc. Pac., San Francisco, p. 325
Andersen J. M., Korhonen H., 2015, MNRAS, 448, 3053
Andretta V., Giampapa M. S., Covino E., Reiners A., Beeck B., 2017, ApJ, 839, 97
Anugu N. et al., 2021, in Tuthill P. G., Mérand A., Sallum S., eds, Proc. SPIE Conf. Ser. Vol. 11446, Optical and Infrared Interferometry and Imaging VII. SPIE, Bellingham, p. 114460N
Apai D., Radigan J., Buenzli E., Burrows A., Reid I. N., Jayawardhana R., 2013, ApJ, 768, 121
Apai D. et al., 2017, Science, 357, 683
Apai D. et al., 2018, preprint (arXiv:1803.08708)
Apai D., Nardiello D., Bedin L. R., 2021, ApJ, 906, 64
Araújo A., Valio A., 2021, ApJ, 907, L5
Artigau É., Bouchard S., Doyon R., Lafrenière D., 2009, ApJ, 701, 1534
Aschwanden M. J., Freeland S. L., 2012, ApJ, 754, 112
Asplund M., Grevesse N., Sauval A. J., 2005, ASP Conf. Ser. Vol. 336, Cosmic Abundances as Records of Stellar Evolution and Nucleosynthesis. Astron. Soc. Pac., San Francisco, p. 25
Asplund M., Grevesse N., Sauval A. J., Scott P., 2009, ARA&A, 47, 481
Atroshchenko I. N., Gadun A. S., Kostyk R. I., 1989a, Afz, 31, 281
Atroshchenko I. N., Gadun A. S., Kostyk R. I., 1989b, Solar and Stellar Granulation, NATO Advanced Science Institutes (ASI) Series C, Vol. 263. Kluwer, Dordrecht, p. 521
Aulanier G., Démoulin P., Schrijver C. J., Janvier M., Pariat E., Schmieder B., 2013, A&A, 549, A66
Auvergne M. et al., 2009, A&A, 506, 411
Ayres T. R., 2021, ApJ, 908, 205
Babcock H. W., Babcock H. D., 1955, ApJ, 121, 349
Baines E. K., McAlister H. A., ten Brummelaar T. A., Turner N. H., Sturmann J., Sturmann L., Goldfinger P. J., Ridgway S. T., 2008, ApJ, 680, 728
Baines E. K., McAlister H. A., ten Brummelaar T. A., Sturmann J., Sturmann L., Turner N. H., Ridgway S. T., 2009, ApJ, 701, 154
Bakos G., Noyes R. W., Kovács G., Stanek K. Z., Sasselov D. D., Domsa I., 2004, PASP, 116, 266
Bakos G. Á. et al., 2013, PASP, 125, 154
Baliunas S. L. et al., 1995, ApJ, 438, 269
Ballerini P., Micela G., Lanza A. F., Pagano I., 2012, A&A, 539, A140
Baranec C., Ziegler C., Law N. M., Morton T., Riddle R., Atkinson D., Schonhut J., Crepp J., 2016, AJ, 152, 18
Barragán O. et al., 2019, MNRAS, 490, 698
Barros S. C. C., Boué G., Gibson N. P., Pollacco D. L., Santerne A., Keenan F. P., Skillen I., Street R. A., 2013, MNRAS, 430, 3032
Barstow J. K., Irwin P. G. J., 2016, MNRAS, 461, L92
Basri G., 2021, An Introduction to Stellar Magnetic Activity. IoP Publishing, Bristol

Basri G., Shah R., 2020, ApJ, 901, 14
Bastien F. A., Stassun K. G., Basri G., Pepper J., 2013, Nature, 500, 427
Bastien F. A., Stassun K. G., Basri G., Pepper J., 2016, ApJ, 818, 43
Bazilevskaya G. A., Cliver E. W., Kovaltsov G. A., Ling A. G., Shea M. A., Smart D. F., Usoskin I. G., 2014, Space Sci. Rev., 186, 409
Bazot M. et al., 2011, A&A, 526, L4
Bean J. L., Miller-Ricci Kempton E., Homeier D., 2010, Nature, 468, 669
Bean J. L. et al., 2018, PASP, 130, 114402
Beckers J. M., Schröter E. H., 1968, Sol. Phys., 4, 303
Beeck B., 2014, PhD thesis, Georg-August-Universität Göttingen
Beeck B., Schüssler M., Reiners A., 2011, ASP Conf. Ser. Vol. 448, 16th Cambridge Workshop on Cool Stars, Stellar Systems, and the Sun. Astron. Soc. Pac., San Francisco, p. 1071
Beeck B. et al., 2012, A&A, 539, A121
Beeck B., Cameron R. H., Reiners A., Schüssler M., 2013a, A&A, 558, A48
Beeck B., Cameron R. H., Reiners A., Schüssler M., 2013b, A&A, 558, A49
Beeck B., Schüssler M., Cameron R. H., Reiners A., 2015a, A&A, 581, A42
Beeck B., Schüssler M., Cameron R. H., Reiners A., 2015b, A&A, 581, A43
Béky B., Kipping D. M., Holman M. J., 2014, MNRAS, 442, 3686
Bellot Rubio L., Orozco Suárez D., 2019, Living Rev. Sol. Phys., 16, 1
Benneke B. et al., 2019a, Nature Astron., 3, 813
Benneke B. et al., 2019b, ApJ, 887, L14
Benz W. et al., 2021, Exp. Astron., 51, 109
Berdyugina S. V., 1998, A&A, 338, 97
Berdyugina S. V., 2002, Astron. Nachr., 323, 192
Berdyugina S. V., 2005, Living Rev. Sol. Phys., 2, 8
Berdyugina S. V., 2009, Proc. IAU Symp. 259, Cosmic Magnetic Fields: From Planets, to Stars and Galaxies. Cambridge Univ. Press, Cambridge, p. 323
Berdyugina S. V., 2011, ASP Conf. Ser. Vol. 437, Solar Polarization 6. Astron. Soc. Pac., San Francisco, p. 219
Berdyugina S. V., Fluri D. M., 2004, A&A, 417, 775
Berdyugina S. V., Henry G. W., 2007, ApJ, 659, L157
Berdyugina S. V., Kuhn J. R., 2019, AJ, 158, 246
Berdyugina S. V., Solanki S. K., 2002, A&A, 385, 701
Berdyugina S. V., Tuominen I., 1998, A&A, 336, L25
Berdyugina S. V., Jankov S., Ilyin I., Tuominen I., Fekel F. C., 1998, A&A, 334, 863
Berdyugina S. V., Ilyin I., Tuominen I., 1999, A&A, 347, 932
Berdyugina S. V., Frutiger C., Solanki S. K., Livingstone W., 2000, A&A, 364, L101
Berdyugina S. V., Pelt J., Tuominen I., 2002, A&A, 394, 505
Berdyugina S. V., Solanki S. K., Frutiger C., 2003, A&A, 412, 513
Berdyugina S. V., Braun P. A., Fluri D. M., Solanki S. K., 2005, A&A, 444, 947
Berdyugina S. V., Petit P., Fluri D. M., Afram N., Arnaud J., 2006, ASP Conf. Ser. Vol. 358, Solar Polarization 4. Astron. Soc. Pac., San Francisco, p. 381
Berdyugina S. V., Harrington D. M., Kuzmychov O., Kuhn J. R., Hallinan G., Kowalski A. F., Hawley S. L., 2017, ApJ, 847, 61
Berger T. E., Berdyugina S. V., 2003, ApJ, 589, L117
Berger T. E., Title A. M., 2001, ApJ, 553, 449
Berger T. E., Rouppe van der Voort L., Löfdahl M., 2007, ApJ, 661, 1272
Berta Z. K., Charbonneau D., Bean J., Irwin J., Burke C. J., Désert J.-M., Nutzman P., Falco E. E., 2011, ApJ, 736, 12
Berta Z. K. et al., 2012, ApJ, 747, 35
Beskin G. M. et al., 1988, Sov. Astron. Lett., 14, 65
Bétrémieux Y., Kaltenegger L., 2013, ApJ, 772, L31
Bhatia T., Cameron R., Solanki S., Peter H., Przybylski D., Witzke V., Shapiro A., 2021, American Astronomical Society Meeting Abstracts, 53, 304.04
Bhatia T. S., Cameron R. H., Solanki S. K., Peter H., Przybylski D., Witzke V., Shapiro A., 2022, A&A, 663, A166
Biazzo K. et al., 2022, A&A, 664, A161
Biller B. A. et al., 2013, ApJ, 778, L10
Blanco Rodríguez J., Kneer F., 2010, A&A, 509, A92
Bogdan T. J., Gilman P. A., Lerche I., Howard R., 1988, ApJ, 327, 451
Boisse I., Bonfils X., Santos N. C., 2012, A&A, 545, A109
Boldt S., Oshagh M., Dreizler S., Mallonn M., Santos N. C., Claret A., Reiners A., Sedaghati E., 2020, A&A, 635, A123
Boley A. C., Van Laerhoven C., Granados Contreras A. P., 2020, AJ, 159, 207
Bonifacio P. et al., 2018, A&A, 611, A68
Bopp B. W., Evans D. S., 1973, MNRAS, 164, 343
Borrero J. M., Ichimoto K., 2011, Living Rev. Sol. Phys., 8, 4
Borucki W. J. et al., 2010, Science, 327, 977
Boyajian T. S. et al., 2012a, ApJ, 746, 101
Boyajian T. S. et al., 2012b, ApJ, 757, 112
Boyajian T. S. et al., 2013, ApJ, 771, 40
Bradshaw S. J., Hartigan P., 2014, ApJ, 795, 79
Brehm N. et al., 2021, Nature Geosci., 14, 10
Brown D. J. A., 2014, MNRAS, 442, 1844
Brown T. M., Charbonneau D., Gilliland R. L., Noyes R. W., Burrows A., 2001, ApJ, 552, 699
Bruno G., Deleuil M., 2021, preprint (arXiv:2104.06173)
Bruno G. et al., 2016, A&A, 595, A89
Bruno G. et al., 2022, MNRAS, 509, 5030
Budding E., 1977, Ap&SS, 48, 207
Buehler D., Lagg A., van Noort M., Solanki S. K., 2019, A&A, 630, A86
Buenzli E., Apai D., Radigan J., Reid I. N., Flateau D., 2014, ApJ, 782, 77
Burdanov A. Y. et al., 2019, MNRAS, 487, 1634
Cabrera J. et al., 2010, A&A, 522, A110
Campante T. L. et al., 2016, ApJ, 830, 138
Carlsson M., Stein R. F., 2002, ApJ, 572, 626
Carlsson M., Hansteen V. H., Gudiksen B. V., Leenaarts J., De Pontieu B., 2016, A&A, 585, A4
Carter J. A., Winn J. N., 2010, ApJ, 716, 850
Casanovas J., 1997, ASP Conf. Ser. Vol. 118, 1st Advances in Solar Physics Euroconference. Advances in Physics of Sunspots. Astron. Soc. Pac., San Francisco, p. 3
Castelli F., Kurucz R. L., 2003, Proc. IAU Symp. 210, Modelling of Stellar Atmospheres. Astron. Soc. Pac., San Francisco, p. A20
Catalano S., Biazzo K., Frasca A., Marilli E., 2002, A&A, 394, 1009
Cauley P. W., Kuckein C., Redfield S., Shkolnik E. L., Denker C., Llama J., Verma M., 2018, AJ, 156, 189
Chachan Y. et al., 2019, AJ, 158, 244
Chaplin W. J. et al., 2011a, ApJ, 732, 54
Chaplin W. J. et al., 2011b, Science, 332, 213
Chaplin W. J. et al., 2015, PASP, 127, 1038
Chapman G. A., 1970, Sol. Phys., 13, 78
Chapman G. A., Cookson A. M., Preminger D. G., 2013, Sol. Phys., 283, 295
Charbonneau D., Brown T. M., Latham D. W., Mayor M., 2000, ApJ, 529, L45
Charbonneau D., Brown T. M., Noyes R. W., Gilliland R. L., 2002, ApJ, 568, 377
Chatzistergos T., Ermolli I., Krivova N. A., Solanki S. K., 2019a, A&A, 625, A69
Chatzistergos T., Ermolli I., Solanki S. K., Krivova N. A., Giorgi F., Yeo K. L., 2019b, A&A, 626, A114
Chatzistergos T., Ermolli I., Giorgi F., Krivova N. A., Puiu C. C., 2020a, J. Space Weather Space Clim., 10, 45
Chatzistergos T. et al., 2020b, A&A, 639, A88
Chen G., Guenther E. W., Pallé E., Nortmann L., Nowak G., Kunz S., Parviainen H., Murgas F., 2017, A&A, 600, A138
Chiavassa A., Plez B., Josselin E., Freytag B., 2009, A&A, 506, 1351
Chiavassa A. et al., 2017, A&A, 597, A94
Choudhary D. P., Cadavid A. C., Cookson A., Chapman G. A., 2020, Sol. Phys., 295, 15
Ciceri S. et al., 2013, A&A, 557, A30
Claret A., 2009, A&A, 506, 1335
Clette F., 2021, J. Space Weather Space Clim., 11, 2
Corsaro E., Fröhlich H. E., Bonanno A., Huber D., Bedding T. R., Benomar O., De Ridder J., Stello D., 2013, MNRAS, 430, 2313
Cowan N. B. et al., 2009, ApJ, 700, 915
Cowan N. B., Fuentes P. A., Haggard H. M., 2013, MNRAS, 434, 2465
Cracchiolo G., Micela G., Peres G., 2021, MNRAS, 501, 1733

Cranmer S. R., Bastien F. A., Stassun K. G., Saar S. H., 2014, ApJ, 781, 124
Crida A., Ligi R., Dorn C., Lebreton Y., 2018, ApJ, 860, 122
Criscuoli S., 2019, ApJ, 872, 52
Criscuoli S., Ermolli I., 2008, A&A, 484, 591
Criscuoli S., Norton A., Whitney T., 2017, ApJ, 847, 93
Csizmadia S., Pasternacki T., Dreyer C., Cabrera J., Erikson A., Rauer H., 2013, A&A, 549, A9
Czesla S., Huber K. F., Wolter U., Schröter S., Schmitt J. H. M. M., 2009, A&A, 505, 1277
Dai F., Winn J. N., 2017, AJ, 153, 205
Danielski C., Deroo P., Waldmann I. P., Hollis M. D. J., Tinetti G., Swain M. R., 2014, ApJ, 785, 35
Danielski C. et al., 2022, Exp. Astron., 53, 473
Danilovic S., Gandorfer A., Lagg A., Schüssler M., Solanki S. K., Vögler A., Katsukawa Y., Tsuneta S., 2008, A&A, 484, L17
Davenport J., 2015, PhD thesis, Univ. Washington
Davenport J. R. A., 2016, ApJ, 829, 23
de la Cruz Rodríguez J., Rouppe van der Voort L., Socas-Navarro H., van Noort M., 2013, A&A, 556, A115
De Pontieu B. et al., 2006, ApJ, 646, 1405
De Pontieu B. et al., 2014, Sol. Phys., 289, 2733
de Wijn A. G., Stenflo J. O., Solanki S. K., Tsuneta S., 2009, Space Sci. Rev., 144, 275
Deeg H. J., Garrido R., Claret A., 2001, New Astron., 6, 51
Delrez L. et al., 2018, Proc. SPIE Conf. Ser. Vol. 10700, Ground-based and Airborne Telescopes VII. SPIE, Bellingham, p. 107001I
Delrez L. et al., 2022, A&A, 667, A59
Deming D. et al., 2013, ApJ, 774, 95
Desai M., Giacalone J., 2016, Living Rev. Sol. Phys., 13, 3
Désert J. M. et al., 2011b, A&A, 526, A12
Désert J.-M. et al., 2011a, ApJS, 197, 14
Deutsch A. J., 1958, Proc. IAU Symp. 6, Electromagnetic Phenomena in Cosmical Physics. Cambridge Univ. Press, Cambridge, p. 209
Di Folco E., Thévenin F., Kervella P., Domiciano de Souza A., Coudé du Foresto V., Ségransan D., Morel P., 2004, A&A, 426, 601
Donati J. F., 1999, MNRAS, 302, 457
Donati J. F., Collier Cameron A., 1997, MNRAS, 291, 1
Donati J. F., Landstreet J. D., 2009, ARA&A, 47, 333
Donati J.-F., Semel M., Carter B. D., Rees D. E., Collier Cameron A., 1997, MNRAS, 291, 658
Dorren J. D., 1987, ApJ, 320, 756
Doyle L., Ramsay G., Doyle J. G., Wu K., Scullion E., 2018, MNRAS, 480, 2153
Dravins D., Nordlund Å., 1990a, A&A, 228, 184
Dravins D., Nordlund Å., 1990b, A&A, 228, 203
Ducrot E. et al., 2020, A&A, 640, A112
Dukes R. J., Jr, 1992, ASP Conf. Ser. Vol. 103, Robotic Telescopes in the 1990s. Astron. Soc. Pac., San Francisco, p. 9
Dunn R. B., Zirker J. B., 1973, Sol. Phys., 33, 281
Engvold O., Vial J.-C., Skumanich A., 2019, The Sun as a Guide to Stellar Physics. Elsevier, The Netherlands
Ermolli I., Fofi M., Bernacchia C., Berrilli F., Caccin B., Egidi A., Florio A., 1998, Sol. Phys., 177, 1
Ermolli I., Criscuoli S., Centrone M., Giorgi F., Penza V., 2007, A&A, 465, 305
Ermolli I., Criscuoli S., Uitenbroek H., Giorgi F., Rast M. P., Solanki S. K., 2010, A&A, 523, A55
Ermolli I. et al., 2013, Atmos. Chem. Phys., 13, 3945
Espinoza N., Jordán A., 2015, MNRAS, 450, 1879
Espinoza N. et al., 2019, MNRAS, 482, 2065
Faria J. P., Haywood R. D., Brewer B. J., Figueira P., Oshagh M., Santerne A., Santos N. C., 2016, A&A, 588, A31
Faurobert M., Criscuoli S., Carbillet M., Contursi G., 2020, A&A, 642, A186
Faurobert-Scholl M., 1993, A&A, 268, 765
Feinstein A. D. et al., 2019, PASP, 131, 094502
Feinstein A. D., Montet B. T., Ansdell M., Nord B., Bean J. L., Günther M. N., Gully-Santiago M. A., Schlieder J. E., 2020, AJ, 160, 219
Feller A., Gandorfer A., Iglesias F. A., Lagg A., Riethmüller T. L., Solanki S. K., Katsukawa Y., Kubo M., 2020, in Evans C. J., Bryant J. J., Motohara K., eds, Proc. SPIE Conf. Ser. Vol. 11447, Ground-based and Airborne Instrumentation for Astronomy VIII. SPIE, Bellingham, p. 11447AK
Findeisen K., Hillenbrand L., Soderblom D., 2011, AJ, 142, 23
Fligge M., Solanki S. K., Unruh Y. C., 2000, A&A, 353, 380
Fontenla J. M., Avrett E. H., Loeser R., 1993, ApJ, 406, 319
Fontenla J., White O. R., Fox P. A., Avrett E. H., Kurucz R. L., 1999, ApJ, 518, 480
Fontenla J. M., Avrett E. H., Loeser R., 2002, ApJ, 572, 636
Fontenla J. M., Avrett E., Thuillier G., Harder J., 2006, ApJ, 639, 441
Fontenla J. M., Curdt W., Haberreiter M., Harder J., Tian H., 2009, ApJ, 707, 482
Fossati L., Ingrassia S., Lanza A. F., 2015, ApJ, 812, L35
Fraine J. et al., 2014, Nature, 513, 526
France K. et al., 2016, ApJ, 820, 89
Freytag B., Steffen M., Dorch B., 2002, Astron. Nachr., 323, 213
Freytag B., Steffen M., Ludwig H. G., Wedemeyer-Böhm S., Schaffenberger W., Steiner O., 2012, J. Comput. Phys., 231, 919
Frohlich C. et al., 1997, Sol. Phys., 170, 1
Fuhrmeister B. et al., 2022, A&A, 657, A125
Gaidos E., Claytor Z., Dungee R., Ali A., Feiden G. A., 2023, MNRAS, 520, 5283
Gan T. et al., 2022a, MNRAS, 511, 83
Gan T. et al., 2022b, MNRAS, 514, 4120
Garcia E. V. et al., 2016, PASP, 128, 055004
Gaudi B. S. et al., 2020, preprint (arXiv:2001.06683)
Gaulme P. et al., 2016, ApJ, 833, L13
Ghosh A. et al., 2016, Proc. SPIE Conf. Ser. Vol. 9905, Space Telescopes and Instrumentation 2016: Ultraviolet to Gamma Ray. SPIE, Bellingham, p. 990503
Gibbs A. et al., 2020, AJ, 159, 169
Giles H. A. C., Collier Cameron A., Haywood R. D., 2017, MNRAS, 472, 1618
Gizis J. E. et al., 2015, ApJ, 813, 104
Gnevyshev M. N., 1938, Izv. Gl. Astron. Obs. Pulkove, 16, 36
Goode P. R., Coulter R., Gorceix N., Yurchyshyn V., Cao W., 2010, Astron. Nachr., 331, 620
Gravity Collaboration, 2017, A&A, 602, A94
Gray D. F., 2005, The Observation and Analysis of Stellar Photospheres. Cambridge Univ. Press, Cambridge
Gray D. F., Johanson H. L., 1991, PASP, 103, 439
Greene T. P., Line M. R., Montero C., Fortney J. J., Lustig-Yaeger J., Luther K., 2016, ApJ, 817, 17
Grindlay J., Tang S., Simcoe R., Laycock S., Los E., Mink D., Doane A., Champine G., 2009, ASP Conf. Ser. Vol. 410, Preserving Astronomy's Photographic Legacy: Current State and the Future of North American Astronomical Plates. Astron. Soc. Pac., San Francisco, p. 101
Grindlay J., Tang S., Los E., Servillat M., 2012, Proc. IAU Symp. 285, New Horizons in Time Domain Astronomy. Cambridge Univ. Press, Cambridge, p. 29
Gudiksen B. V., Carlsson M., Hansteen V. H., Hayek W., Leenaarts J., Martínez-Sykora J., 2011, A&A, 531, A154
Gully-Santiago M. A. et al., 2017, ApJ, 836, 200
Günther M. N. et al., 2020, AJ, 159, 60
Hale G. E., 1908, ApJ, 28, 315
Hall D. S., Henry G. W., 1994, Int. Amat.-Prof. Photoelectr. Photometry Commun., 55, 51
Hall O. J. et al., 2021, Nature Astron., 5, 707
Hamann A., Montet B. T., Fabrycky D. C., Agol E., Kruse E., 2019, AJ, 158, 133
Harvey J., Livingston W., 1969, Sol. Phys., 10, 283
Hathaway D. H., 2015, Living Rev. Sol. Phys., 12, 4
Hawley S. L., Pettersen B. R., 1991, ApJ, 378, 725
Hawley S. L., Davenport J. R. A., Kowalski A. F., Wisniewski J. P., Hebb L., Deitrick R., Hilton E. J., 2014, ApJ, 797, 121
Haywood R. D. et al., 2014, MNRAS, 443, 2517

Hedges C., Luger R., Dotson J., Foreman-Mackey D., Barentsen G., 2021, AJ, 161, 95
Hellier C. et al., 2015, AJ, 150, 18
Henriques V. M. J., Nelson C. J., Rouppe van der Voort L. H. M., Mathioudakis M., 2020, A&A, 642, A215
Henry T. J., Soderblom D. R., Donahue R. A., Baliunas S. L., 1996, AJ, 111, 439
Henry G. W., Marcy G. W., Butler R. P., Vogt S. S., 2000, ApJ, 529, L41
Herbst K., Papaioannou A., Airapetian V. S., Atri D., 2021, ApJ, 907, 89
Herrero E., Ribas I., Jordi C., Morales J. C., Perger M., Rosich A., 2016, A&A, 586, A131
Hirzberger J., Wiehr E., 2005, A&A, 438, 1059
Hirzberger J. et al., 2010, ApJ, 723, L154
Holczer T. et al., 2016, ApJS, 225, 9
Houdek G., Balmforth N. J., Christensen-Dalsgaard J., Gough D. O., 1999, A&A, 351, 582
Howard W. S. et al., 2020, ApJ, 902, 115
Huber D. et al., 2011, ApJ, 743, 143
Huenemoerder D. P., Ramsey L. W., Buzasi D. L., 1989, AJ, 98, 2264
Hussain G. A. J., 2002, Astron. Nachr., 323, 349
Husser T. O., Wende-von Berg S., Dreizler S., Homeier D., Reiners A., Barman T., Hauschildt P. H., 2013, A&A, 553, A6
Iyer A. R., Line M. R., 2020, ApJ, 889, 78
Iyer A. R., Line M. R., Muirhead P. S., Fortney J. J., Gharib-Nezhad E., 2023, ApJ, 944, 41
Järvinen S. P., Berdyugina S. V., Strassmeier K. G., 2005a, A&A, 440, 735
Järvinen S. P., Berdyugina S. V., Tuominen I., Cutispoto G., Bos M., 2005b, A&A, 432, 657
Järvinen S. P., Korhonen H., Berdyugina S. V., Ilyin I., Strassmeier K. G., Weber M., Savanov I., Tuominen I., 2008, A&A, 488, 1047
Järvinen S. P., Strassmeier K. G., Carroll T. A., Ilyin I., Weber M., 2018, A&A, 620, A162
Jeffers S. V., Donati J. F., Collier Cameron A., 2007, MNRAS, 375, 567
Johnson L. J., Norris C. M., Unruh Y. C., Solanki S. K., Krivova N., Witzke V., Shapiro A. I., 2021, MNRAS, 504, 4751
Jordán A. et al., 2013, ApJ, 778, 184
Juvan I. G., Lendl M., Cubillos P. E., Fossati L., Tregloan-Reed J., Lammer H., Guenther E. W., Hanslmeier A., 2018, A&A, 610, A15
Kahil F., Riethmüller T. L., Solanki S. K., 2017, ApJS, 229, 12
Kallinger T. et al., 2014, A&A, 570, A41
Karoff C. et al., 2018, ApJ, 852, 46
Katsukawa Y. et al., 2007, Science, 318, 1594
Keller C. U., Harvey J. W., Giampapa M. S., 2003, Proc. SPIE Conf. Ser. Vol. 4853, Innovative Telescopes and Instrumentation for Solar Astrophysics. SPIE, Bellingham, p. 194
Keller C. U., Schüssler M., Vögler A., Zakharov V., 2004, ApJ, 607, L59
Kervella P., Fouqué P., 2008, A&A, 491, 855
Kervella P., Bersier D., Mourard D., Nardetto N., Fouqué P., Coudé du Foresto V., 2004a, A&A, 428, 587
Kervella P., Thévenin F., Di Folco E., Ségransan D., 2004b, A&A, 426, 297
Keys P. H. et al., 2019, MNRAS, 488, L53
Kiepenheuer K. O., 1953, ApJ, 117, 447
Kiess C., Rezaei R., Schmidt W., 2014, A&A, 565, A52
Kilcik A., Sarp V., Yurchyshyn V., Rozelot J.-P., Ozguc A., 2020, Sol. Phys., 295, 58
Kilpatrick B. M. et al., 2020, AJ, 159, 51
Kiraga M., Stepien K., 2007, Acta Astron., 57, 149
Kirk J., Wheatley P. J., Louden T., Littlefair S. P., Copperwheat C. M., Armstrong D. J., Marsh T. R., Dhillon V. S., 2016, MNRAS, 463, 2922
Kirk J. et al., 2021, AJ, 162, 34
Kitai R., 1986, Sol. Phys., 104, 287
Kitai R., Muller R., 1984, Sol. Phys., 90, 303
Kjeldsen H., Bedding T. R., 2011, A&A, 529, L8
Kleint L., Berdyugina S. V., Shapiro A. I., Bianda M., 2010, A&A, 524, A37
Kleint L., Shapiro A. I., Berdyugina S. V., Bianda M., 2011, A&A, 536, A47
Knutson H. A. et al., 2011, ApJ, 735, 27
Knutson H. A. et al., 2012, ApJ, 754, 22
Kobel P., Solanki S. K., Borrero J. M., 2011, A&A, 531, A112
Kochanek C. S. et al., 2017, PASP, 129, 104502
Kopp G., 2016, J. Space Weather Space Clim., 6, A30
Kopp G., 2021, Sol. Phys., 296, 133
Korhonen H. et al., 2021, A&A, 646, A6
Kostogryz N. M., Berdyugina S. V., 2015, A&A, 575, A89
Kostogryz N. M., Milic I., Berdyugina S. V., Hauschildt P. H., 2016, A&A, 586, A87
Kostogryz N. M., Yakobchuk T. M., Berdyugina S. V., Milic I., 2017, A&A, 601, A6
Kovári Z., Bartus J., Strassmeier K. G., Vida K., Švanda M., Oláh K., 2007, A&A, 474, 165
Kowalski A. F., Hawley S. L., Wisniewski J. P., Osten R. A., Hilton E. J., Holtzman J. A., Schmidt S. J., Davenport J. R. A., 2013, ApJS, 207, 15
Kreidberg L. et al., 2014, Nature, 505, 69
Krivova N. A., Solanki S. K., Fligge M., Unruh Y. C., 2003, A&A, 399, L1
Kron G. E., 1947, PASP, 59, 261
Kulow J. R., France K., Linsky J., Loyd R. O. P., 2014, ApJ, 786, 132
Kurucz R. L., 1992a, Rev. Mex. Astron. Astrofis., 23, 45
Kurucz R. L., 1992b, Rev. Mex. Astron. Astrofis., 23, 181
Kurucz R. L., 1992c, Rev. Mex. Astron. Astrofis., 23, 187
Kuzmychov O., Berdyugina S. V., Harrington D. M., 2017, ApJ, 847, 60
Lam K. W. F. et al., 2020, AJ, 159, 120
Lammer H., Selsis F., Ribas I., Guinan E. F., Bauer S. J., Weiss W. W., 2003, ApJ, 598, L121
Langhans K., Schmidt W., Rimmele T., 2004, A&A, 423, 1147
Lanza A. F., Catalano S., Cutispoto G., Pagano I., Rodono M., 1998, A&A, 332, 541
Law N. M. et al., 2014, ApJ, 791, 35
Le Bouquin J. B. et al., 2011, A&A, 535, A67
Leenaarts J., Wedemeyer-Böhm S., 2006, A&A, 460, 301
Leenaarts J., Carlsson M., Hansteen V., Rutten R. J., 2007, A&A, 473, 625
Leenaarts J., Carlsson M., Rouppe van der Voort L., 2012, ApJ, 749, 136
Lightkurve Collaboration, 2018, Astrophysics Source Code Library, record ascl:1812.013
Linsky J. L., 2017, ARA&A, 55, 159
Lites B. W. et al., 2008, ApJ, 672, 1237
Livingston W., Harvey J., 1971, Proc. IAU Symp. 43, Solar Magnetic Fields. D. Reidel Publishing Company, Dordrecht, p. 51
Livingston W., Harvey J. W., Malanushenko O. V., Webster L., 2006, Sol. Phys., 239, 41
Llama J., Shkolnik E. L., 2015, ApJ, 802, 41
Llama J., Shkolnik E. L., 2016, ApJ, 817, 81
Ludwig H. G., Caffau E., Steffen M., Freytag B., Bonifacio P., Kučinskas A., 2009, Mem. Soc. Astron. Ital., 80, 711
Luger R. et al., 2017, Nature Astron., 1, 0129
Luger R., Foreman-Mackey D., Hedges C., 2021a, AJ, 162, 124
Luger R., Foreman-Mackey D., Hedges C., Hogg D. W., 2021b, AJ, 162, 123
Lupu R. E. et al., 2014, ApJ, 784, 27
McCullough P. R., Crouzet N., Deming D., Madhusudhan N., 2014, ApJ, 791, 55
MacDonald R. J., 2023, J. Open Source Softw., 8, 4873
MacDonald R. J., Madhusudhan N., 2017, MNRAS, 469, 1979
Maciejewski G. et al., 2016, A&A, 588, L6
Maehara H., Shibayama T., Notsu Y., Notsu S., Honda S., Nogami D., Shibata K., 2015, Earth Planets Space, 67, 59
Magic Z. et al., 2013, A&A, 557, A26
Magrini L. et al., 2022, A&A, 663, A161
Mallonn M., Strassmeier K. G., 2016, A&A, 590, A100
Mallonn M. et al., 2018, A&A, 614, A35
Mancini L. et al., 2013, MNRAS, 436, 2
Mancini L. et al., 2014a, A&A, 568, A127
Mancini L. et al., 2014b, MNRAS, 443, 2391
Mancini L. et al., 2015, A&A, 579, A136
Mancini L. et al., 2016, A&A, 590, A112
Mancini L. et al., 2017, MNRAS, 465, 843
Mandal S., Krivova N. A., Cameron R., Solanki S. K., 2021, A&A, 652, A9
Mann A. W., Feiden G. A., Gaidos E., Boyajian T., von Braun K., 2015, ApJ, 804, 64

Mansfield M. et al., 2018, ApJ, 868, L34
Marchenko S. V., Woods T. N., DeLand M. T., Mauceri S., Pilewskie P., Haberreiter M., 2019, Earth Space Sci., 6, 2379
Marfil E. et al., 2021, A&A, 656, A162
Martinez A. O., Baron F. R., Monnier J. D., Roettenbacher R. M., Parks J. R., 2021, ApJ, 916, 60
Mathew S. K., Martínez Pillet V., Solanki S. K., Krivova N. A., 2007, A&A, 465, 291
Mathur S. et al., 2011, ApJ, 741, 119
Matthes K. et al., 2017, Geoscientific Model Dev., 10, 2247
Maxted P. F. L., 2016, A&A, 591, A111
Maxted P. F. L., 2018, A&A, 616, A39
Maxted P. F. L., Serenelli A. M., Southworth J., 2015, A&A, 577, A90
Mayfield E. B., Lawrence J. K., 1985, Sol. Phys., 96, 293
Mayorga L. C. et al., 2021, Planet. Sci. J., 2, 140
Mehltretter J. P., 1974, Sol. Phys., 38, 43
Metchev S. A. et al., 2015, ApJ, 799, 154
Michel E. et al., 2008, Science, 322, 558
Milbourne T. W. et al., 2021, ApJ, 920, 21
Miles-Páez P. A., Metchev S. A., Heinze A., Apai D., 2017, ApJ, 840, 83
Millar-Blanchaer M. A. et al., 2020, ApJ, 894, 42
Mirtorabi M. T., Wasatonic R., Guinan E. F., 2003, AJ, 125, 3265
Miyakawa K., Hirano T., Fukui A., Mann A. W., Gaidos E., Sato B., 2021, AJ, 162, 104
Močnik T., Clark B. J. M., Anderson D. R., Hellier C., Brown D. J. A., 2016, AJ, 151, 150
Močnik T., Hellier C., Anderson D. R., Clark B. J. M., Southworth J., 2017a, MNRAS, 469, 1622
Močnik T., Southworth J., Hellier C., 2017b, MNRAS, 471, 394
Mohler-Fischer M. et al., 2013, A&A, 558, A55
Monnier J. D. et al., 2018, Proc. SPIE Conf. Ser. Vol. 10701, Optical and Infrared Interferometry and Imaging VI. SPIE, Bellingham, p. 1070118
Montalto M., Boué G., Oshagh M., Boisse I., Bruno G., Santos N. C., 2014, MNRAS, 444, 1721
Montet B. T., Tovar G., Foreman-Mackey D., 2017, ApJ, 851, 116
Morin J. et al., 2008, MNRAS, 384, 77
Morley C. V., Kreidberg L., Rustamkulov Z., Robinson T., Fortney J. J., 2017, ApJ, 850, 121
Morris B. M., Hebb L., Davenport J. R. A., Rohn G., Hawley S. L., 2017, ApJ, 846, 99
Morris B. M., Agol E., Davenport J. R. A., Hawley S. L., 2018a, ApJ, 857, 39
Morris B. M., Agol E., Hebb L., Hawley S. L., 2018b, AJ, 156, 91
Morris B. M. et al., 2018c, ApJ, 863, L32
Morris B. M., Curtis J. L., Douglas S. T., Hawley S. L., Agüeros M. A., Bobra M. G., Agol E., 2018d, AJ, 156, 203
Morris B. M., Hawley S. L., Hebb L., 2018e, Res. Notes Am. Astron. Soc., 2, 26
Morris B. M., Bobra M. G., Agol E., Lee Y. J., Hawley S. L., 2020, MNRAS, 493, 5489
Mosser B. et al., 2012, A&A, 537, A30
Müller D. et al., 2020, A&A, 642, A1
Murgas F., Chen G., Pallé E., Nortmann L., Nowak G., 2019, A&A, 622, A172
Murray-Clay R. A., Chiang E. I., Murray N., 2009, ApJ, 693, 23
Namekata K. et al., 2019, ApJ, 871, 187
Namekata K. et al., 2020, ApJ, 891, 103
Narukage N. et al., 2016, Proc. SPIE Conf. Ser. Vol. 9905, Space Telescopes and Instrumentation 2016: Ultraviolet to Gamma Ray. SPIE, Bellingham, p. 990508
Nascimbeni V. et al., 2015, A&A, 579, A113
Neckel H., Labs D., 1994, Sol. Phys., 153, 91
Neff J. E., O'Neal D., Saar S. H., 1995, ApJ, 452, 879
Nèmec N. E., Shapiro A. I., Işık E., Sowmya K., Solanki S. K., Krivova N. A., Cameron R. H., Gizon L., 2022, ApJ, 934, L23
Netto Y., Valio A., 2020, A&A, 635, A78
Neveu-VanMalle M. et al., 2016, A&A, 586, A93
Newman P. D. et al., 2023, AJ, 165, 151
Newton E. R., Irwin J., Charbonneau D., Berta-Thompson Z. K., Dittmann J. A., West A. A., 2016, ApJ, 821, 93
Newton E. R., Irwin J., Charbonneau D., Berlind P., Calkins M. L., Mink J., 2017, ApJ, 834, 85
Newton E. R., Mondrik N., Irwin J., Winters J. G., Charbonneau D., 2018, AJ, 156, 217
Nichols-Fleming F., Blackman E. G., 2020, MNRAS, 491, 2706
Nikolov N. et al., 2015, MNRAS, 447, 463
Nikolov N., Sing D. K., Gibson N. P., Fortney J. J., Evans T. M., Barstow J. K., Kataria T., Wilson P. A., 2016, ApJ, 832, 191
Nordgren T. E. et al., 1999, AJ, 118, 3032
Nordlund A., 1982, A&A, 107, 1
Nordlund A., 1984, Small-Scale Dynamical Processes in Quiet Stellar Atmospheres. National Solar Observatory, Sunspot, New Mexico, p. 181
Nordlund A., 1985, Sol. Phys., 100, 209
Nordlund A., Dravins D., 1990, A&A, 228, 155
Nordlund Å., Stein R. F., Asplund M., 2009, Living Rev. Sol. Phys., 6, 2
Norris C. M., 2018, PhD thesis, Imperial College London
Norris C. M., Beeck B., Unruh Y. C., Solanki S. K., Krivova N. A., Yeo K. L., 2017, A&A, 605, A45
Notsu Y. et al., 2013, ApJ, 771, 127
Notsu Y. et al., 2019, ApJ, 876, 58
Noyes R. W., Hartmann L. W., Baliunas S. L., Duncan D. K., Vaughan A. H., 1984, ApJ, 279, 763
Nutzman P., Charbonneau D., 2008, PASP, 120, 317
O'Neal D., Saar S. H., Neff J. E., 1998, ApJ, 501, L73
Okamoto T. J., Sakurai T., 2018, ApJ, 852, L16
Okamoto S., Notsu Y., Maehara H., Namekata K., Honda S., Ikuta K., Nogami D., Shibata K., 2021, ApJ, 906, 72
Oláh K. et al., 2009, A&A, 501, 703
Omodei N., Pesce-Rollins M., Longo F., Allafort A., Krucker S., 2018, ApJ, 865, L7
Ortiz A., Solanki S. K., Domingo V., Fligge M., Sanahuja B., 2002, A&A, 388, 1036
Osborn A., Bayliss D., 2020, MNRAS, 491, 4481
Oshagh M., Boisse I., Boué G., Montalto M., Santos N. C., Bonfils X., Haghighipour N., 2013a, A&A, 549, A35
Oshagh M., Santos N. C., Boisse I., Boué G., Montalto M., Dumusque X., Haghighipour N., 2013b, A&A, 556, A19
Oshagh M., Santos N. C., Ehrenreich D., Haghighipour N., Figueira P., Santerne A., Montalto M., 2014, A&A, 568, A99
Oshagh M., Santos N. C., Figueira P., Adibekyan V. Z., Santerne A., Barros S. C. C., Lima J. J. G., 2015, A&A, 583, L1
Oshagh M., Dreizler S., Santos N. C., Figueira P., Reiners A., 2016, A&A, 593, A25
Oshagh M. et al., 2017, A&A, 606, A107
Oshagh M. et al., 2018, A&A, 619, A150
Owen J. E., Jackson A. P., 2012, MNRAS, 425, 2931
Owen J. E., Wu Y., 2013, ApJ, 775, 105
Owen J. E., Wu Y., 2017, ApJ, 847, 29
Pallavicini R., Golub L., Rosner R., Vaiana G. S., Ayres T., Linsky J. L., 1981, ApJ, 248, 279
Panja M., Cameron R., Solanki S. K., 2020, ApJ, 893, 113
Pannetier C. et al., 2020, Proc. SPIE Conf. Ser. Vol. 11446, Space Telescopes and Instrumentation 2020: Optical, Infrared, and Millimeter Wave. SPIE, Bellingham, p. 114460T
Parker E. N., 1955, ApJ, 122, 293
Parks J. R. et al., 2021, ApJ, 913, 54
Passegger V. M. et al., 2018, A&A, 615, A6
Patra K. C. et al., 2020, AJ, 159, 150
Peck C. L., Rast M. P., 2015, ApJ, 808, 192
Penza V., Caccin B., Del Moro D., 2004, A&A, 427, 345
Pepper J. et al., 2007, PASP, 119, 923
Petrie G., Criscuoli S., Bertello L., 2021, Space Physics and Aeronomy, Vol. 1, Solar Physics and Solar Wind. Geophysical Monograph Series, Vol. 258. Wiley, New York, p. 83
Petrovay K., van Driel-Gesztelyi L., 1997, Sol. Phys., 176, 249

Pinhas A., Rackham B. V., Madhusudhan N., Apai D., 2018, MNRAS, 480, 5314
Piskunov N. E., Tuominen I., Vilhu O., 1990, A&A, 230, 363
Pollacco D. L. et al., 2006, PASP, 118, 1407
Polyansky O. L., Zobov N. F., Viti S., Tennyson J., Bernath P. F., Wallace L., 1997, ApJ, 489, L205
Pont F., Knutson H., Gilliland R. L., Moutou C., Charbonneau D., 2008, MNRAS, 385, 109
Pont F., Aigrain S., Zucker S., 2011, MNRAS, 411, 1953
Pont F., Sing D. K., Gibson N. P., Aigrain S., Henry G., Husnoo N., 2013, MNRAS, 432, 2917
Prša A., Zwitter T., 2005, ApJ, 628, 426
Prša A. et al., 2016, ApJS, 227, 29
Quintana E. V. et al., 2021, preprint (arXiv:2108.06438)
Rackham B. V., de Wit J. 2023, preprint (arXiv:2303.15418)
Rackham B. et al., 2017, ApJ, 834, 151
Rackham B. V., Apai D., Giampapa M. S., 2018, ApJ, 853, 122
Rackham B. V., Apai D., Giampapa M. S., 2019, AJ, 157, 96
Rackham B. V. et al., 2022, preprint (arXiv:2201.09905)
Radick R. R., Lockwood G. W., Skiff B. A., Baliunas S. L., 1998, ApJS, 118, 239
Radigan J., Jayawardhana R., Lafrenière D., Artigau É., Marley M., Saumon D., 2012, ApJ, 750, 105
Radigan J., Lafrenière D., Jayawardhana R., Artigau E., 2014, ApJ, 793, 75
Ragozzine D., Wolf A. S., 2009, ApJ, 698, 1778
Rajpaul V., Aigrain S., Osborne M. A., Reece S., Roberts S., 2015, MNRAS, 452, 2269
Rast M. P., Fox P. A., Lin H., Lites B. W., Meisner R. W., White O. R., 1999, Nature, 401, 678
Rathcke A. D. et al., 2021, AJ, 162, 138
Rauer H. et al., 2014, Exp. Astron., 38, 249
Redfield S., Endl M., Cochran W. D., Koesterke L., 2008, ApJ, 673, L87
Reiners A., 2012, Living Rev. Sol. Phys., 9, 1
Reinhold T., Reiners A., Basri G., 2013, A&A, 560, A4
Reinhold T., Bell K. J., Kuszlewicz J., Hekker S., Shapiro A. I., 2019, A&A, 621, A21
Reinhold T., Shapiro A. I., Witzke V., Nèmec N.-E., Işık E., Solanki S. K., 2021, ApJ, 908, L21
Rempel M., 2012, ApJ, 750, 62
Rempel M., 2020, ApJ, 894, 140
Rempel M., Schüssler M., Cameron R. H., Knölker M., 2009a, Science, 325, 171
Rempel M., Schüssler M., Knölker M., 2009b, ApJ, 691, 640
Ribárik G., Oláh K., Strassmeier K. G., 2003, Astron. Nachr., 324, 202
Ricker G. R. et al., 2014, Proc. SPIE Conf. Ser. Vol. 9143, Space Telescopes and Instrumentation 2014: Optical, Infrared, and Millimeter Wave. SPIE, Bellingham, p. 914320
Ricker G. R. et al., 2015, J. Astron. Tel. Inst. Syst., 1, 014003
Riethmüller T. L., Solanki S. K., Zakharov V., Gandorfer A., 2008, A&A, 492, 233
Rimmele T. R. et al., 2020, Sol. Phys., 295, 172
Robertson P., Mahadevan S., Endl M., Roy A., 2014, Science, 345, 440
Robertson P., Roy A., Mahadevan S., 2015, ApJ, 805, L22
Robertson P. et al., 2020, ApJ, 897, 125
Roettenbacher R. M., Kane S. R., 2017, ApJ, 851, 77
Roettenbacher R. M., Vida K., 2018, ApJ, 868, 3
Roettenbacher R. M., Monnier J. D., Harmon R. O., Barclay T., Still M., 2013, ApJ, 767, 60
Roettenbacher R. M. et al., 2016, Nature, 533, 217
Roettenbacher R. M. et al., 2017, ApJ, 849, 120
Roettenbacher R. M. et al., 2022, AJ, 163, 19
Romano P., Berrilli F., Criscuoli S., Del Moro D., Ermolli I., Giorgi F., Viticchié B., Zuccarello F., 2012, Sol. Phys., 280, 407
Rosich A., Herrero E., Mallonn M., Ribas I., Morales J. C., Perger M., Anglada-Escudé G., Granzer T., 2020, A&A, 641, A82
Rutten R. J., 2007, ASP Conf. Ser. Vol. 368, The Physics of Chromospheric Plasmas. Astron. Soc. Pac., San Francisco, p. 27
Salhab R. G., Steiner O., Berdyugina S. V., Freytag B., Rajaguru S. P., Steffen M., 2018, A&A, 614, A78
Samadi R. et al., 2010a, A&A, 509, A16
Samadi R., Ludwig H. G., Belkacem K., Goupil M. J., Dupret M. A., 2010b, A&A, 509, A15
Samadi R., Belkacem K., Dupret M. A., Ludwig H. G., Baudin F., Caffau E., Goupil M. J., Barban C., 2012, A&A, 543, A120
Sánchez Cuberes M., Vázquez M., Bonet J. A., Sobotka M., 2002, ApJ, 570, 886
Sánchez Cuberes M., Vázquez M., Bonet J. A., Sobotka M., 2003, A&A, 397, 1075
Sanchis-Ojeda R., Winn J. N., 2011, ApJ, 743, 61
Sanchis-Ojeda R., Winn J. N., Holman M. J., Carter J. A., Osip D. J., Fuentes C. I., 2011, ApJ, 733, 127
Sanchis-Ojeda R. et al., 2012, Nature, 487, 449
Sanchis-Ojeda R. et al., 2013, ApJ, 775, 54
Santos N. C. et al., 2013, A&A, 556, A150
Sarkar S., Argyriou I., Vandenbussche B., Papageorgiou A., Pascale E., 2018, MNRAS, 481, 2871
Sayeed M., Huber D., Wheeler A., Ness M. K., 2021, American Astronomical Society Meeting Abstracts, 53, 339.17
Scandariato G., Nascimbeni V., Lanza A. F., Pagano I., Zanmar Sanchez R., Leto G., 2017, A&A, 606, A134
Schad T. A., 2014, Sol. Phys., 289, 1477
Schanche N. et al., 2022, A&A, 657, A45
Scharmer G. B., Bjelksjo K., Korhonen T. K., Lindberg B., Petterson B., 2003, Proc. SPIE Conf. Ser. Vol. 4853, Innovative Telescopes and Instrumentation for Solar Astrophysics. SPIE, Bellingham, p. 341
Schmidt W. et al., 2012, Astron. Nachr., 333, 796
Schmidt S. J. et al., 2014, ApJ, 781, L24
Schofield M. et al., 2019, ApJS, 241, 12
Schrijver C. J. et al., 2012, J. Geophys. Res. (Space Phys.), 117, A08103
Schüssler M., Shelyag S., Berdyugina S., Vögler A., Solanki S. K., 2003, ApJ, 597, L173
Schutte M. C. et al., 2022, AJ, 164, 14
Seager S., Sasselov D. D., 2000, ApJ, 537, 916
Sedaghati E., Boffin H. M. J., Csizmadia S., Gibson N., Kabath P., Mallonn M., Van den Ancker M. E., 2015, A&A, 576, L11
See V., Roquette J., Amard L., Matt S. P., 2021, ApJ, 912, 127
Semel M., 1989, A&A, 225, 456
Serrano L. M., Oshagh M., Cegla H. M., Barros S. C. C., Santos N. C., Faria J. P., Akinsanmi B., 2020, MNRAS, 493, 5928
Shapiro A. I., Fluri D. M., Berdyugina S. V., Bianda M., Ramelli R., 2011, A&A, 529, A139
Shapiro A. I., Solanki S. K., Krivova N. A., Schmutz W. K., Ball W. T., Knaack R., Rozanov E. V., Unruh Y. C., 2014, A&A, 569, A38
Shapiro A. I., Solanki S. K., Krivova N. A., Yeo K. L., Schmutz W. K., 2016, A&A, 589, A46
Shapiro A. I., Solanki S. K., Krivova N. A., Cameron R. H., Yeo K. L., Schmutz W. K., 2017, Nature Astron., 1, 612
Shapiro A., Amazo-Gómez E., Krivova N. A., Solanki S. K., 2020, A&A, 633, A32
Sheeley N. R. J., 1971, Sol. Phys., 20, 19
Shimizu T., 2009, Trans. Space Technol. Japan, 7, Tm_1
Shulyak D. et al., 2019, A&A, 626, A86
Silva A. V. R., 2003, ApJ, 585, L147
Silva-Valio A., Lanza A. F., Alonso R., Barge P., 2010, A&A, 510, A25
Sing D. K., 2010, A&A, 510, A21
Sing D. K., Désert J. M., Lecavelier Des Etangs A., Ballester G. E., Vidal-Madjar A., Parmentier V., Hebrard G., Henry G. W., 2009, A&A, 505, 891
Sing D. K. et al., 2011, MNRAS, 416, 1443
Sing D. K. et al., 2015, MNRAS, 446, 2428
Sing D. K. et al., 2016, Nature, 529, 59
Siu-Tapia A., Lagg A., Solanki S. K., van Noort M., Jurčák J., 2017, A&A, 607, A36
Siu-Tapia A., Lagg A., van Noort M., Rempel M., Solanki S. K., 2019, A&A, 631, A99

Skaf N. et al., 2020, AJ, 160, 109
Skumanich A., 1972, ApJ, 171, 565
Smalley B. et al., 2012, A&A, 547, A61
Snellen I. A. G., Albrecht S., de Mooij E. J. W., Le Poole R. S., 2008, A&A, 487, 357
Snellen I. A. G., de Kok R. J., de Mooij E. J. W., Albrecht S., 2010, Nature, 465, 1049
Sobotka M., Hanslmeier A., 2005, A&A, 442, 323
Sobotka M., Brandt P. N., Simon G. W., 1997a, A&A, 328, 682
Sobotka M., Brandt P. N., Simon G. W., 1997b, A&A, 328, 689
Solanki S. K., 1993, Space Sci. Rev., 63, 1
Solanki S. K., 2003, A&AR, 11, 153
Solanki S. K., Unruh Y. C., 2013, Astron. Nachr., 334, 145
Solanki S. K., Inhester B., Schüssler M., 2006, Rep. Prog. Phys., 69, 563
Sotzen K. S. et al., 2020, AJ, 159, 5
Sousa S. G. et al., 2021, A&A, 656, A53
Southworth J., 2011, MNRAS, 417, 2166
Southworth J. et al., 2009, MNRAS, 399, 287
Southworth J. et al., 2016, MNRAS, 457, 4205
Spake J. J. et al., 2018, Nature, 557, 68
Stassun K. G., Collins K. A., Gaudi B. S., 2017, AJ, 153, 136
Stassun K. G., Corsaro E., Pepper J. A., Gaudi B. S., 2018, AJ, 155, 22
Stefansson G. et al., 2018, Proc. SPIE Conf. Ser. Vol. 10702, Ground-based and Airborne Instrumentation for Astronomy VII. SPIE, Bellingham, p. 1070250
Steffen M., Holweger H., 2002, A&A, 387, 258
Stein R. F., 2012, Living Rev. Sol. Phys., 9, 4
Stein R. F., Nordlund Å., 1998, ApJ, 499, 914
Steiner O., 2005, A&A, 430, 691
Steiner O., Salhab R., Freytag B., Rajaguru P., Schaffenberger W., Steffen M., 2014, PASJ, 66, S5
Stello D. et al., 2011, ApJ, 737, L10
Stello D. et al., 2013, ApJ, 765, L41
Stenflo J. O., 1982, Sol. Phys., 80, 209
Stenflo J. O., Keller C. U., Gandorfer A., 1998, A&A, 329, 319
Stephenson F. R., 1990, Phil. Trans. Roy. Soc. Lond. Ser. A, Math. Phys. Sci., 330, 499
Strassmeier K. G., 2009, A&AR, 17, 251
Strassmeier K. G., Rice J. B., 1998, A&A, 330, 685
Suetterlin P., 1998, A&A, 333, 305
Sulis S., Lendl M., Hofmeister S., Veronig A., Fossati L., Cubillos P., Van Grootel V., 2020, A&A, 636, A70
Sun L. et al., 2017, AJ, 153, 28
Tan X., Showman A. P., 2021, MNRAS, 502, 678
Tang S., Sasselov D., Grindlay J., Los E., Servillat M., 2013, PASP, 125, 793
ten Brummelaar T. A. et al., 2005, ApJ, 628, 453
The LUVOIR Team, 2019, preprint (arXiv:1912.06219)
Tinetti G. et al., 2007, Nature, 448, 169
Tinetti G. et al., 2018, Exp. Astron., 46, 135
Tinetti G. et al., 2021, preprint(arXiv:2104.04824)
Toner C. G., Gray D. F., 1988, ApJ, 334, 1008
Toner C. G., Jefferies S. M., Duvall T. L., 1997, ApJ, 478, 817
Trampedach R., Asplund M., Collet R., Nordlund Å., Stein R. F., 2013, ApJ, 769, 18
Tregloan-Reed J., Unda-Sanzana E., 2019, A&A, 630, A114
Tregloan-Reed J., Unda-Sanzana E., 2021, A&A, 649, A130
Tregloan-Reed J., Southworth J., Tappert C., 2013, MNRAS, 428, 3671
Tregloan-Reed J. et al., 2015, MNRAS, 450, 1760
Tregloan-Reed J. et al., 2018, MNRAS, 474, 5485
Tremblay P.-E., Ludwig H.-G., Freytag B., Steffen M., Caffau E., 2013, A&A, 557, A7
Tremblin P., Phillips M. W., Emery A., Baraffe I., Lew B. W. P., Apai D., Biller B. A., Bonnefoy M., 2020, A&A, 643, A23
Trotta R., 2008, Contemp. Phys., 49, 71
Trujillo Bueno J., Shchukina N., Asensio Ramos A., 2004, Nature, 430, 326
Tsuneta S. et al., 2008, Sol. Phys., 249, 167
Turova I. P., 1984, Sol. Phys., 91, 51
Unruh Y. C., Solanki S. K., Fligge M., 1999, A&A, 345, 635
Usoskin I. G., Solanki S. K., Krivova N. A., Hofer B., Kovaltsov G. A., Wacker L., Brehm N., Kromer B., 2021, A&A, 649, A141
Valio A., Estrela R., Netto Y., Bravo J. P., de Medeiros J. R., 2017, ApJ, 835, 294
Valio A., Spagiari E., Marengoni M., Selhorst C. L., 2020, Sol. Phys., 295, 120
van Belle G. et al., 2020a, in Tuthill P. G., Mérand A., Sallum S., eds, Proc. SPIE Conf. Ser. Vol. 11446, Optical and Infrared Interferometry and Imaging VII. SPIE, Bellingham, p.1144608
van Belle G. T. et al., 2020b, in Tuthill P. G., Mérand A., Sallum S., eds, Proc. SPIE Conf. Ser. Vol. 11446, Optical and Infrared Interferometry and Imaging VII. SPIE, Bellingham, p. 114462K
van Noort M., Lagg A., Tiwari S. K., Solanki S. K., 2013, A&A, 557, A24
van Saders J. L., Ceillier T., Metcalfe T. S., Silva Aguirre V., Pinsonneault M. H., García R. A., Mathur S., Davies G. R., 2016, Nature, 529, 181
Vaughan A. H., Preston G. W., 1980, PASP, 92, 385
Vaughan A. H., Jr, Zirin H., 1968, ApJ, 152, 123
Vernazza J. E., Avrett E. H., Loeser R., 1981, ApJS, 45, 635
Vida K., Kovári Z., Švanda M., Oláh K., Strassmeier K. G., Bartus J., 2007, Astron. Nachr., 328, 1078
Vida K. et al., 2016, A&A, 590, A11
Vida K., Kővári Z., Pál A., Oláh K., Kriskovics L., 2017, ApJ, 841, 124
Vidal-Madjar A. et al., 2004, ApJ, 604, L69
Vinyoles N. et al., 2017, ApJ, 835, 202
Viticchié B., Del Moro D., Criscuoli S., Berrilli F., 2010, ApJ, 723, 787
Vögler A., Shelyag S., Schüssler M., Cattaneo F., Emonet T., Linde T., 2005, A&A, 429, 335
Vogt S. S., 1979, PASP, 91, 616
Vogt S. S., Penrod G. D., 1983, PASP, 95, 565
Vogt S. S., Penrod G. D., Hatzes A. P., 1987, ApJ, 321, 496
Vogt S. S., Hatzes A. P., Misch A. A., Kürster M., 1999, ApJS, 121, 547
Vrard M., Kallinger T., Mosser B., Barban C., Baudin F., Belkacem K., Cunha M. S., 2018, A&A, 616, A94
Wakeford H. R. et al., 2019, AJ, 157, 11
Waldmeier M., 1955, Ergebnisse und Probleme der Sonnenforschung. Geest & Portig, Leipzig, Germany
Walton S. R., Preminger D. G., Chapman G. A., 2003, Sol. Phys., 213, 301
Watanabe H., 2014, PASJ, 66, S1
Watson C. L., Henden A. A., Price A., 2006, Soc. Astron. Sci. Annu. Symp., 25, 47
Watson F. T., Penn M. J., Livingston W., 2014, ApJ, 787, 22
Wedemeyer S., Ludwig H. G., Steiner O., 2013, Astron. Nachr., 334, 137
Wedemeyer-Böhm S., Rouppe van der Voort L., 2009, A&A, 503, 225
Wells R. D. et al., 2021, A&A, 653, A97
Wende S., Reiners A., Ludwig H. G., 2009, A&A, 508, 1429
Wheatley P. J. et al., 2018, MNRAS, 475, 4476
White T. R. et al., 2018, MNRAS, 477, 4403
Wilson R. E., 1979, ApJ, 234, 1054
Wilson R. E., 1990, ApJ, 356, 613
Wilson R. E., 2012, AJ, 144, 73
Wilson R. E., Devinney E. J., 1971, ApJ, 166, 605
Winn J. N., Fabrycky D., Albrecht S., Johnson J. A., 2010, ApJ, 718, L145
Witzke V., Shapiro A. I., Solanki S. K., Krivova N. A., Schmutz W., 2018, A&A, 619, A146
Witzke V., Reinhold T., Shapiro A. I., Krivova N. A., Solanki S. K., 2020, A&A, 634, L9
Witzke V., Shapiro A. I., Kostogryz N. M., Cameron R., Rackham B. V., Seager S., Solanki S. K., Unruh Y. C., 2022, ApJ, 941, L35
Witzke V., Duehnen H. B., Shapiro A. I., Przybylski D., Bhatia T. S., Cameron R., Solanki S. K., 2023, A&A, 669, A157
Wöhl H., 1971, Sol. Phys., 16, 362
Wöhl H., Wittmann A., Schröter E. H., 1970, Sol. Phys., 13, 104
Wootten A., Thompson A. R., 2009, IEEE Proc., 97, 1463
Wright N. J., Newton E. R., Williams P. K. G., Drake J. J., Yadav R. K., 2018, MNRAS, 479, 2351
Yadav R., Mathew S. K., 2018, Sol. Phys., 293, 54
Yadav R. K., Christensen U. R., Morin J., Gastine T., Reiners A., Poppenhaeger K., Wolk S. J., 2015, ApJ, 813, L31

Yeo K. L., Solanki S. K., Krivova N. A., 2013, A&A, 550, A95
Yeo K. L., Feller A., Solanki S. K., Couvidat S., Danilovic S., Krivova N. A., 2014a, A&A, 561, A22
Yeo K. L., Krivova N. A., Solanki S. K., Glassmeier K. H., 2014b, A&A, 570, A85
Yeo K. L., Solanki S. K., Krivova N. A., Rempel M., Anusha L. S., Shapiro A. I., Tagirov R. V., Witzke V., 2020a, Geophys. Res. Lett., 47, e90243
Yeo K. L., Solanki S. K., Krivova N. A., 2020b, A&A, 639, A139
Yu J., Huber D., Bedding T. R., Stello D., Hon M., Murphy S. J., Khanna S., 2018, ApJS, 236, 42
Zakharov V., Gandorfer A., Solanki S. K., Löfdahl M., 2005, A&A, 437, L43
Zaleski S. M., Valio A., Marsden S. C., Carter B. D., 2019, MNRAS, 484, 618
Zaleski S. M., Valio A., Carter B. D., Marsden S. C., 2020, MNRAS, 492, 5141
Zellem R., Guinan E. F., Messina S., Lanza A. F., Wasatonic R., McCook G. P., 2010, PASP, 122, 670
Zellem R. T. et al., 2017, ApJ, 844, 27
Zellem R. T. et al., 2019, PASP, 131, 094401
Zellem R. T. et al., 2020, PASP, 132, 054401
Zhang X., Showman A. P., 2014, ApJ, 788, L6
Zhang Z., Zhou Y., Rackham B. V., Apai D., 2018, AJ, 156, 178
Zhang M., Chachan Y., Kempton E. M. R., Knutson H. A., 2019, PASP, 131, 034501
Ziegler C. et al., 2017, AJ, 153, 66
Ziegler C., Tokovinin A., Briceño C., Mang J., Law N., Mann A. W., 2020, AJ, 159, 19

APPENDIX A: ACRONYMS USED

For convenience, Table A1 lists the acronyms and abbreviations used in this review.

Table A1. Acronyms and abbreviations used in this review.

Acronym or Abbreviation	Definition
3D	Three-dimensional
ALMA	Atacama Large Millimeter/submillimeter Array
ASAS-SN	All Sky Automated Survey for SuperNovae
BFI	Broad-band Filter Imager
CASE	Contribution to Ariel Spectroscopy of Exoplanets
CHARA	Center for High Angular Resolution Astronomy
CLASP	Chromospheric Lyman-Alpha Spectro-Polarimeter
CO5BOLD	COnservative COde for the COmputation of COmpressible COnvection in a BOx of L Dimensions, L = 2,3
CoRoT	Convection, Rotation, and planetary Transits
CLV	Center-to-limb variation
DASCH	Digital Access to a Sky Century @ Harvard
DKIST	Daniel K. Inouye Solar Telescope
DI	Doppler imaging
EUV	Extreme ultraviolet
ExoFOP	Exoplanet Follow-up Observing Program
ExoPAG	Exoplanet Exploration Program Analysis Group
GOES	Geostationary Operational Environmental Satellites
HabEx	Habitable Exoplanet Observatory
HARPS-N	High Accuracy Radial velocity Planet Searcher for the Northern hemisphere
HD	Hydrodynamic
HST	Hubble Space Telescope
IRIS	Interface Region Imaging Spectrograph
ISS	International Space Station
JWST	James Webb Space Telescope
KELT	Kilodegree Extremely Little Telescope
Kepler	Kepler Space Telescope
LTE	Local thermodynamic equilibrium
LUVOIR	Large UV/Optical/IR Surveyor
MCMC	Markov chain Monte Carlo
MHD	Magnetohydrodynamic
MHS	Millionths of the hemisphere of the Sun
MIRC-X	Michigan InfraRed Combiner-eXeter
MURaM	Max-Planck-Institute for Aeronomy/University of Chicago Radiation Magneto-hydrodynamics code
NASA	National Aeronautics and Space Administration
NIR	Near-infrared
NPOI	Navy Precision Optical Interferometer
NSF	National Science Foundation
OMI	Ozone Monitoring Experiment
PCH	Photospheric and chromospheric heterogeneities
PIONIER	Precision Integrated Optics Near Infrared ExpeRiment
ppm	Parts-per-million
ppt	Parts-per-thousand
PLATO	PLAnetary Transit and Oscillations
PSPT	Precision Solar Photometric Telescope

Table A1 – *continued*

Acronym or Abbreviation	Definition
RMS	Root mean square
RV	Radial velocity
SAG21	Study Analysis Group 21
SATIRE	Spectral And Total Irradiance REconstruction
SDO	Solar Dynamics Observatory
SED	Spectral energy distribution
SOHO	Solar and Heliospheric Observatory
SOLIS	Synoptic Long-term Investigations of the Sun
SORCE	Solar Radiation and Climate Experiment
SOT	Solar Optical Telescope
SPICA	Stellar Parameters and Images with a Cophased Array
Spitzer	Spitzer Space Telescope
SST	Swedish Solar Tower
SUIT	Solar Ultraviolet Imaging Telescope
SUVI	Solar Ultraviolet Imager
TESS	Transiting Exoplanet Survey Satellite
TOI	TESS Object of Interest
TIM	Total irradiance monitor
TLSE	Transit light source effect
TSI	Total solar irradiance
UV	Ultraviolet
VIRGO	Variability of solar IRradiance and Gravity Oscillations
VISION	Visible Imaging System for Interferometric Observations
VLTI	Very Large Telescope Interferometer
WASP	Wide Angle Search for Planets
ZDI	Zeeman–Doppler imaging

[1]*Department of Earth, Atmospheric and Planetary Sciences, Massachusetts Institute of Technology, 77 Massachusetts Avenue, Cambridge, MA 02139, USA*
[2]*Kavli Institute for Astrophysics and Space Research, Massachusetts Institute of Technology, Cambridge, MA 02139, USA*
[3]*Space Telescope Science Institute, 3700 San Martin Drive, Baltimore, MD 21218, USA*
[4]*Leibniz-Institut für Sonnenphysik (KIS), Schöneckstrasse 6, D-79104 Freiburg, Germany*
[5]*Istituto Ricerche Solari Aldo e Cele Daccò (IRSOL), Faculty of Informatics, Università della Svizzera italiana, Locarno 6605, Switzerland*
[6]*European Southern Observatory (ESO), Alonso de Córdova 3107, Vitacura, Santiago, Chile*
[7]*Department of Astronomy, University of Michigan, 1085 South University Avenue, Ann Arbor, MI 48109, USA*
[8]*School of Physics, University of New South Wales, Sydney, NSW 2052, Australia*
[9]*Center for Space and Habitability, University of Bern, Gesellschaftsstrasse 6, CH-3012 Bern, Switzerland*
[10]*Instituto de Astrofísica de Canarias, E-38200 La Laguna, Tenerife, Spain*
[11]*Max-Planck-Institut für Sonnensystemforschung, Justus-von-Liebig-Weg 3, D-37077 Göttingen, Germany*
[12]*Department of Physics, Imperial College London, Prince Consort Road, London SW7 2AZ, UK*
[13]*NASA Goddard Space Flight Center, 8800 Greenbelt Road, Greenbelt, MD 20771, USA*
[14]*Jet Propulsion Laboratory, California Institute of Technology, 4800 Oak Grove Drive, Pasadena, CA 91109, USA*
[15]*Steward Observatory, The University of Arizona, 933 North Cherry Avenue, Tucson, AZ 85721, USA*
[16]*Lunar and Planetary Laboratory, The University of Arizona, 1629 E. University Blvd., Tucson, AZ 85721, USA*
[17]*University of Maryland, Baltimore County, 1000 Hilltop Circle, Baltimore, MD 21250, USA*
[18]*School of Physical Sciences, The Open University, Walton Hall, Milton Keynes MK7 6AA, UK*
[19]*INAF, Osservatorio Astrofisico di Catania, Via S. Sofia 78, I-95123 Catania, Italy*
[20]*Space Research Institute, Austrian Academy of Sciences, Schmiedlstrasse 6, A-8042 Graz, Austria*
[21]*School of Physics and Astronomy, University of Leicester, University Road, Leicester LE1 7RH, UK*
[22]*Department of Physics, University of Warwick, Coventry CV4 7AL, UK*
[23]*National Solar Observatory, 3665 Discovery Drive, Boulder, CO 80303, USA*
[24]*Observatoire de Genève, Université de Genève, Chemin des Maillettes 51, CH-1290 Versoix, Switzerland*
[25]*School of Earth and Space Exploration, Arizona State University, 525 E. University Dr., Tempe, AZ 85281, USA*
[26]*Laboratory for Atmospheric and Space Physics, University of Colorado Boulder, Boulder, CO 80303, USA*
[27]*Leibniz-Institut für Astrophysik Potsdam (AIP), An der Sternwarte 16, D-14482 Potsdam, Germany*
[28]*Center for Astrophysics | Harvard & Smithsonian, 60 Garden St, Cambridge, MA 02138, USA*
[29]*Universitäts-Sternwarte, Ludwig-Maximilians-Universität München, Scheinerstrasse 1, D-81679 München, Germany*
[30]*Exzellenzcluster Origins, Boltzmannstraße 2, D-85748 Garching, Germany*
[31]*Landessternwarte, Zentrum für Astronomie der Universität Heidelberg, Königstuhl 12, D-69117 Heidelberg, Germany*
[32]*Department of Physics and Astronomy, Dartmouth College, Hanover, NH 03755, USA*
[33]*National Solar Observatory, Boulder, CO 80303, USA*
[34]*Department of Astrophysics and Planetary Sciences, University of Colorado, Boulder, CO 80303, USA*
[35]*Yale Center for Astronomy and Astrophysics, Yale University, 46 Hillhouse Avenue, New Haven, CT 06511, USA*
[36]*Department of Astronomy, Yale University, 52 Hillhouse Avenue, New Haven, CT 06511, USA*
[37]*Department of Physics and Astronomy, Vanderbilt University, Nashville, TN 37235, USA*

[38]*Johns Hopkins University Applied Physics Laboratory, 11100 Johns Hopkins Road, Laurel, MD 20723, USA*
[39]*Instituto de Investigación en Astronomia y Ciencias Planetarias, Universidad de Atacama, Copiapó, Atacama 1531772, Chile*
[40]*Centro de Rádio Astronomia e Astrofisica Mackenzie, Mackenzie Presbyterian University, Rua da Consolacao, 896, Sao Paulo, Brazil*
[41]*Rosseland Centre for Solar Physics, University of Oslo, Postboks 1029 Blindern, 0315 Oslo, Norway*
[42]*Institute of Theoretical Astrophysics, University of Oslo, Postboks 1029 Blindern, 0315 Oslo, Norway*
[43]*Carnegie Earth & Planets Laboratory, 5241 Broad Branch Road NW, Washington, DC 20015, USA*
[44]*Astronomy Department, University of Washington, Box 951580, Seattle, WA 98195, USA*
[45]*Department of Astronomy, University of Maryland, College Park, MD 20742, USA*
[46]*Department of Astronomy, Boston University, Boston, MA 02215, USA*
[47]*Department of Astrophysical Sciences, Princeton University, Princeton, NJ 08544, USA*
[48]*Astrobiology Research Unit, Université de Liège, 19C Allée du 6 Aout, B-4000 Liège, Belgium*
[49]*Department of Astronomy and Astrophysics, University of Chicago, 5640 South Ellis Avenue, Chicago, IL 60637, USA*
[50]*SETI Institute, 189 Bernardo Avenue, Suite 200, Mountain View, CA 94043, USA*
[51]*Gemini Observatory/NSF's NOIRLab, 670 N. A'ohoku Place, Hilo, HI 96720, USA*
[52]*Institut de Ciències de l'Espai (ICE, CSIC), Campus UAB, C/Can Magrans s/n, E-08193 Bellaterra, Spain*
[53]*Institut d'Estudis Espacials de Catalunya (IEEC), E-08034 Barcelona, Spain*

This paper has been typeset from a TEX/LATEX file prepared by the author.